



UNICAMP

UNIVERSIDADE ESTADUAL DE CAMPINAS

INSTITUTO DE QUÍMICA

EDISON HUERTAS MONTOYA

**SYNTHESIS OF CORE-MULTISHELL GOLD
NANORODS@Gd₂O₃:Yb,Er@Gd₂O₃:Nd FOR BIOMEDICAL APPLICATIONS**

**SÍNTESE DE NANOPARTÍCULAS DO TIPO CAROÇO@CASCA BASEADAS EM
NANOBASTÕES DE OURO@Gd₂O₃:Yb,Er@Gd₂O₃:Nd PARA APLICAÇÕES
BIOMÉDICAS**

CAMPINAS

2020

EDISON HUERTAS MONTOYA

**SYNTHESIS OF CORE-MULTISHELL GOLD
NANORODS@Gd₂O₃:Yb,Er@Gd₂O₃:Nd FOR BIOMEDICAL APPLICATIONS**

**SÍNTESE DE NANOPARTÍCULAS DO TIPO CAROÇO@CASCA BASEADAS EM
NANOBASTÕES DE OURO@Gd₂O₃:Yb,Er@Gd₂O₃:Nd PARA APLICAÇÕES
BIOMÉDICAS**

Dissertação de Mestrado apresentada ao Instituto de Química da
Universidade Estadual de Campinas como parte dos requisitos
exigidos para a obtenção do título de Mestre(a) em Química na área de
Química Inorgânica

Master's dissertation presented to the Institute of Chemistry of the
University of Campinas as part of the requirements to obtain the title
Master's in Chemistry in the area of Inorganic Chemistry.

Dissertation Advisor: Prof. Italo Odone Mazali, PhD

O arquivo digital corresponde à versão final da Dissertação defendida pelo aluno Edison Huertas Montoya e orientada pelo Prof. Dr. Italo Odone Mazali.

**CAMPINAS
2020**

Ficha catalográfica
Universidade Estadual de Campinas
Biblioteca do Instituto de Química
Simone Luiz Alves - CRB 8/9094

M768s Montoya, Edison Huertas, 1991-
Synthesis of core-multishell gold nanorods@Gd₂O₃:Yb,Er@Gd₂O₃:Nd for biomedical applications / Edison Huertas Montoya. – Campinas, SP : [s.n.], 2020.

Orientador: Italo Odone Mazali.
Dissertação (mestrado) – Universidade Estadual de Campinas, Instituto de Química.

1. Nanopartículas caroço-casca. 2. Ressonância de plasmon de superfície. 3. Lantanídeos. 4. Luminescência. 5. Nanopartículas de ouro. I. Mazali, Italo Odone, 1972-. II. Universidade Estadual de Campinas. Instituto de Química. III. Título.

Informações para Biblioteca Digital

Título em outro idioma: Síntese de nanopartículas do tipo caroço@casca baseadas em nanobastões de ouro@Gd₂O₃:Yb,Er@Gd₂O₃:Nd para aplicações biomédicas

Palavras-chave em inglês:

Core-shell nanoparticles
Surface plasmon resonance
Lanthanides
Luminescence
Gold nanoparticles

Área de concentração: Química Inorgânica

Titulação: Mestre em Química na área de Química Inorgânica

Banca examinadora:

Italo Odone Mazali [Orientador]
Paulo Cesar de Sousa Filho
Elias de Barros Santos

Data de defesa: 16-09-2020

Programa de Pós-Graduação: Química

Identificação e informações acadêmicas do(a) aluno(a)
- ORCID do autor: <https://orcid.org/0000-0003-0878-9977>
- Currículo Lattes do autor: <http://lattes.cnpq.br/6419328046187087>

BANCA EXAMINADORA

Prof. Dr. Italo Odone Mazali (Orientador)

Prof. Dr. Paulo Cesar de Sousa Filho (IQ-UNICAMP)

Prof. Dr. Elias de Barros Santos (IQ-UNIFESP/São José dos Campos)

A Ata da defesa assinada pelos membros da Comissão Examinadora, consta no SIGA/Sistema de Fluxo de Dissertação/Tese e na Secretaria do Programa da Unidade.

Este exemplar corresponde à redação final da Dissertação de Mestrado defendida pelo aluno **EDISON HUERTAS MONTOYA**, aprovada pela Comissão Julgadora em 16 de Setembro de 2020.

DEDICATION

I dedicate this work to the engine of my life, my son Esteban, my family and all the people who helped me in the way to reach this goal.

ACKNOWLEDGMENTS

- To my mother Divanelly and my brother Sebastian who always encourage me to go ahead and pursue my dreams. Also special thanks to my family for the constant support and affection;
- To my advisor and friend Prof. Italo Mazali for the opportunity, for trusting in my work, for all the teachings and for the constant support in every moment. Also a special thanks to Prof. Fernando Sigoli for all the discussions and contributions to this work;
- To my Colombian friends Alejandro, Julie, Javier, Josaphat, Katherine, Monica and Paula for all the support and the great moments shared. Special thanks to my second brother Gonzalo for follow me in this new adventure;
- To all my dear friends from the LMF for the warm reception, the kindness and all the good moments shared: Anerise, Claudia, Déborah, Filipe, Geovana, Gesiane, Isabela, Isaías, Jaciara, Josi, Lanousse, Laura, Lohana, Raisa, Rafael, Raul, Rodrigo, Sergio, Tainá and William. A special thanks to Amanda and Naiara for all the support, the discussions and funny moments which make me feel one at home;
- To Flávia, the kindest person that I have ever met for the support and encouragement in every moment;
- To Douglas, Flávia, and Erico for the microscopy images.
- To all the teachers, technicians and collaborators of the Institute of Chemistry for the hard work and for contributing to our academic formation. A special thanks to Claudia, Milene, and Sônia for the training, patient and kindness every day;
- To the Coordenação de Aperfeiçoamento de Pessoal de Nível Superior (CAPES) for the scholarship granted;
- This study was financed in part by the Coordenação de Aperfeiçoamento de Pessoal de Nível Superior - Brasil (CAPES) - Finance Code 001.

“Nothing in life is to be feared, it is only to be understood. Now is the time to understand more, so that we may fear less.”

Marie Curie

RESUMO

Os nanobastões de ouro (AuNRs) são nanomateriais que apresentam atividade teranóstica eficiente devido à sua grande capacidade de conversão fototérmica, fácil funcionalização da superfície e modificação das propriedades de absorção por meio do deslocamento da banda de ressonância de plasmon de superfície localizada em função da razão de aspecto, por meio do controle das condições de síntese. Quando um fluoróforo está localizado próximo à superfície de uma nanopartícula metálica o campo eletromagnético intensificado gerado pela excitação do plasmon de superfície pode aumentar as taxas de excitação e emissão, e criar novas rotas de relaxação, o que pode levar a um aumento da intensidade da luminescência do fluoróforo. Portanto, o objetivo desta pesquisa foi realizar a síntese de nanoestruturas hierárquicas do tipo caroço-casca utilizando nanobastões de ouro, revestidos com $Gd_2O_3:Er(III), Yb(III)$ e $Gd_2O_3:Nd(III)$, a fim de aumentar a intensidade de emissão do sistema na região visível e do infravermelho próximo, modificando a razão de aspecto dos nanobastões para controlar localmente o aprimoramento dos processos de transferência de energia como *down shifting* e *up-conversion*. As nanopartículas do tipo caroço-casca foram sintetizadas por um processo solvotérmico seguido de um tratamento térmico a alta temperatura e caracterizadas por espectroscopia de infravermelho, ultravioleta-visível, difração de raios X e fluorescência; microscopia eletrônica de transmissão e análise termogravimétrica. As micrografias de transmissão eletrônica e o análise de difração de raios X confirmam a formação bem-sucedida da estrutura hierárquica AuNRs@ $Gd_2O_3:Yb,Er$ @ $Gd_2O_3:Nd$. Além disso, as medidas de espectroscopia de fluorescência mostram atividade na região do infravermelho próximo. Assim, o sistema proposto apresentar potenciais aplicação na terapia fototérmica devido ao fenômeno de hipertermia induzido pelos AuNRs e como sensor de temperatura mediante medidas de termometria ótica da luminescência associada aos íons lantanídeos.

ABSTRACT

Gold nanorods (AuNRs) are nanomaterials that show efficient theranostic activity due to their great photothermal conversion capacity, easy surface functionalization and easy modification of their absorption properties by shifting the localized surface plasmon resonance (LSPR) band as a function of the aspect ratio through the modification of the synthetic conditions. When a fluorophore is located close to the surface of a metallic nanoparticle, the intensified electromagnetic field generated by the excitation of the LSPR band may increase both the excitation and emission rates and create new relaxation pathways, which could lead to enhanced fluorescence intensity. Therefore, the purpose of this research is carry out the synthesis of core-multishell hierarchical nanostructures using AuNRs, coated with $Gd_2O_3:Er(III), Yb(III)$ and $Gd_2O_3:Nd(III)$. In order to improve the emission of the system in the visible and NIR region by modifying the aspect ratio of the AuNRs to locally control the enhancement of the up-conversion or down shifting transfer energy processes. The core-shell nanoparticles were synthesized by a solvothermal process followed by a thermal treatment at high temperature and characterized by infrared, ultraviolet-visible, X-ray diffraction (XRD) and fluorescence spectroscopy, transmission electron microscopy and thermogravimetric analysis. Transmission microscopy images and XRD analysis confirm the successful formation of the hierarchical structure $AuNRs@Gd_2O_3:YbEr@Gd_2O_3:Nd$. In addition, fluorescence spectroscopy measurements show the different emissions of the Er, Yb and Nd ions showing activity in the near-infrared region. Thus, the proposed system may have potential applications in photothermal therapy due to the hyperthermia phenomenon generated for the AuNRs providing improved photothermal capacity and acting as a thermal sensor through thermometry measures of the Lanthanoid ions luminescence.

RESUMEN

Los nanobastones de oro (AuNRs) son nanomateriales que presentan alta actividad teranóstica debido a su eficiente capacidad de conversión fototérmica, fácil funcionalización de la superficie y fácil modificación de sus propiedades de absorción variando las condiciones de síntesis, lo que permite la deslocalización de la banda plasmon de resonancia de superficie localizada en función de la relación de aspecto. Cuando un fluoróforo se encuentra posicionado cerca a la superficie de una nanopartícula metálica, el campo electromagnético intensificado generado por la excitación de la banda plasmon, puede llevar a un aumento de las velocidades de excitación y emisión del fluoróforo y la creación de nuevas rutas de relajación, lo que puede conducir a un aumento de la intensidad de emisión. Teniendo esto en cuenta, el propósito de esta investigación es llevar a cabo la síntesis nanoestructuras híbridas de tipo núcleo-multicoraza utilizando AuNRs recubiertos con $Gd_2O_3:Er(III), Yb(III)$ y $Gd_2O_3:Nd(III)$, con el fin de aumentar la intensidad de la luminiscencia en la región del visible y el infrarrojo cercano manipulando la relación de aspecto de los AuNRs para promover y mejorar localmente los diferentes procesos de transferencia de energía como el *up-conversion* y el *down shifting*. Las nanopartículas núcleo-coraza fueron sintetizadas mediante un proceso solvotermal seguido por un tratamiento térmico a alta temperatura y caracterizadas por espectroscopia de ultravioleta visible, fluorescencia e infrarroja, difracción de rayos X, microscopia de transmisión electrónica y análisis termogravimétrico. Las micrografías de transmisión electrónica y el análisis de difracción de rayos X confirman la formación exitosa de la estructura nucleo-multicoraza AuNRs@ $Gd_2O_3:YbEr@Gd_2O_3:Nd$. Además, las medidas de espectroscopia de fluorescencia muestran que el sistema es activo en la región del infrarrojo cercano. Por lo que, el sistema propuesto presenta potenciales aplicaciones en terapia fototérmica aprovechando el fenómeno de hipertermia inducido por los AuNRs, así como control de la temperatura mediante medidas de termometría óptica de la luminiscencia asociada a los iones lantánidos.

LIST OF FIGURES

Figure 1. a) Schematic illustration of LSPR excitation for gold nanospheres. Reproduced from ref. 9 copyrights <i>Annu. Rev. Phys. Chem.</i> 2007. b) Typical LSPR band of gold nanospheres. Reproduced from ref. 8. Copyrights <i>Sensors Actuators, B Chem</i> 2014.	21
Figure 2. Representative scheme of the most common gold nanoparticle assemblies and morphologies. Reproduced from ref. 7. Copyright 2018 <i>Journal of Nanomaterials</i>	22
Figure 3. a) Schematic illustration of longitudinal and transverse LSPR excitation for AuNRs. b) Longitudinal and transverse LSPR absorption bands of AuNRs reproduced from ref. 8 copyrights <i>sensors and actuators B</i> 2014 and c) Longitudinal LSPR band tuning and color change of the AuNRs as a function of the aspect ratio reproduced from ref. 20 copyrights <i>Talanta</i> 2018.	23
Figure 4. a) Wavelength effect in tissue penetration reproduced from ref. 62 copyrights <i>royal society</i> 2016 and b) biological spectral window reproduced from ref. 16 copyrights <i>Nanoscale Horizons</i> 2016.	24
Figure 5. Core-shell NPs applications reproduced from ref. 29 copyrights <i>Nanoscale Research Letters</i> 2019.	25
Figure 6. Energy scale of the electronic structure of lanthanoid ions. From left to right, electron-electron interaction, spin-orbit coupling, and ligand field effect. Adapted from ref. 39. Copyrights <i>American Chemical Society</i> 1995.	29
Figure 7. Up-Conversion main processes. a) Energy transfer UC (ETU), b) Excited State Absorption (ESA) and c) Photon avalanche (PA).	31
Figure 8. a) Representative scheme of the general steps involved in the UC emission process and b) Intrinsic material characteristics that affect the UC process: distance between optically active elements (left) local symmetry and phonon density of states (right). Adapted from ref.39. Copyright 2019 <i>Advance Materials</i>	32
Figure 9. Schematic illustration of down-shifting general process a) and b) single ion c) Non-radiative energy transfer from a Ln ion A to B. (the energy in excess is dissipated by phonons). Adapted from ref 56. Copyrights <i>ACS Nano</i> 2019.	33
Figure 10. a) Schematic illustration of the plasmon enhancement fluorescence on fluorophore. Adapted from ref. 50. <i>Rev. Phys.</i> 2019. b) Jablonski diagram showing the pathways through which energy is transferred between energy states when a fluorophore is in the absence or presence of a metallic NP. Adapted from ref. 62. Copyrights <i>Materials Today advances</i> 2020.	36
Figure 11. a) Transmission electron microscopy image of the AuNRs@SiO ₂ /NaYF ₄ :Tb(III),Yb(III)@NaYF ₄ core-shell NPS with a SiO ₂ thickness layer of 35 nm. b) Absorption spectra as a function of the SiO ₂ thickness 0-45 nm. c) UC emission spectra $\lambda_{exc} = 980$ nm (left), enhancement factor as a function of the SiO ₂ thickness and NP concentration (right). d) QC emission spectra $\lambda_{exc} = 372$ nm (left), enhancement factor as a	

<i>function of the SiO₂ thickness and NP concentration (right). Reproduced from ref. 68. Copyrights J. Lumin. 2019.</i>	39
Figure 12. <i>Luminescence decay curves of Er(III) ⁴I_{11/2} → ⁴I_{15/2} transition (λ_{exc} = 486 nm, λ_{em} = 977 nm) in β-NaYF₄:Er(III) NPs decorated x% Au NRs (x = 0, 0.075, 0.15, 0.225, 0.3, 0.375). Inset: Calculated lifetimes of Er(III) ⁴I_{11/2} excited state decorated with x% Au NRs (x = 0, 0.075, 0.15, 0.225, 0.3, 0.375). Reproduced from ref 60. Copyrights Opt. Commun 2019.</i>	40
Figure 13. <i>Schematic illustration of the synthesis procedure of AuNRs with H₂O₂ as the reducing agent under basic conditions.</i>	46
Figure 14. <i>Schematic illustration of the formation process of the AuNRs@Gd₂O₃:Er(III),Yb(III)@ Gd₂O₃:Nd(III) core-multishell nanoparticles.</i>	48
Figure 15. <i>a) AuNRs-790 UV-Vis spectra using 20 μL AgNO₃ and H₂O₂/Au (III) = 13.82. (----) Before centrifugation; (----) after centrifugation. b) UV-Vis spectra normalized at 400nm.</i>	54
Figure 16. <i>a) AuNRs-931 UV-Vis spectra using 60 μL AgNO₃ and H₂O₂/Au(III) = 28.14 (----) before centrifugation; (----) after centrifugation. b) UV-Vis spectra normalized at 400nm.</i>	54
Figure 17. <i>TEM images of the AuNRs-790 at different magnifications. 20 nm (top left), 100 nm (top right and bottom).</i>	56
Figure 18. <i>TEM images of the AuNRs-931 at different magnifications. 50 nm (top), 100 nm (bottom).</i>	57
Figure 19. <i>Size distribution and aspect ratio of. a) AuNRs-790 and b) AuNRs-931. Were counted 355 and 308 NPs respectively.</i>	58
Figure 20. <i>TEM images of the AuNRs@Gd(OH)₃/GdOHCO₃:Er(III),Yb(III)-H₂O at different magnifications with Au/Gd(NO₃)₃ ratio of a) 1:800 and b) 1:1.</i>	60
Figure 21. <i>TEM images of AuNRs@Gd(OH)₃/GdOHCO₃:Er(III),Yb(III)-H₂O precursor at different magnifications a) From this work b) Reproduced from ref 83. c) Reproduced from ref 81.</i>	61
Figure 22. <i>EELS mapping of the AuNRs@Gd(OH)₃/GdOHCO₃:Er(III),Yb(III)-H₂O core-shell NPs.</i>	62
Figure 23. <i>a) Transmission electron micrograph and b) EDS mapping of the core-multishell system.</i>	64
Figure 24. <i>TG and DTA curves of the AuNRs@Gd(OH)₃/GdOHCO₃:Er(III),Yb(III)@Gd(OH)₃/GdOHCO₃:Nd(III)-H₂O.</i>	66
Figure 25. <i>IR spectra of the samples: after thermal treatment under different conditions a) 800 °C 3h b) 600 °C 2h c) 600 °C 0.5h. And d) before thermal treatment.</i>	68
Figure 26. <i>IR spectra of a) hydroxycarbonate and b) gadolinium oxide. Reproduced from ref.9. Copyright 2010 University of Campinas.</i>	69
Figure 27. <i>a) TEM image and EDS mapping, b) single crystal HR-TEM image and c) SAED pattern of AuNRs@Gd₂O₃:Er(III),Yb(III)@Gd₂O₃:Nd(III) after thermal treatment at 800 °C for 3h.</i>	70

Figure 28. XRD patterns of a) AuNRs@Gd ₂ O ₃ :Er(III),Yb(III)@Gd ₂ O ₃ :Nd(III) after thermal treatment at 800 °C for 3h. b) AuNPs PDF: 4-784 and c) Gd ₂ O ₃ PDF: 862477.	71
Figure 29. Emission spectra of the AuNRs@Gd ₂ O ₃ :Er(III),Yb(III)@Gd ₂ O ₃ :Nd(III) under 808 nm laser irradiation.	72
Figure 30. Emission spectra of the AuNRs@Gd ₂ O ₃ :Er(III),Yb(III)@Gd ₂ O ₃ :Nd(III) under 980 nm laser irradiation.	73
Figure 31. Proposed energy mechanisms for the emission of AuNRs@Gd ₂ O ₃ :Er(III),Yb(III)@Gd ₂ O ₃ :Nd(III) a) $\lambda_{exc}=980$ nm b) $\lambda_{exc}=808$ nm.	73
Figure 32. Linear Intensity Ratio (LIR) as a function of temperature under 980 nm laser irradiation.	75
Figure 33. Stacked emission spectra of AuNRs@Gd ₂ O ₃ :Er(III),Yb(III)@Gd ₂ O ₃ :Nd(III) by varying the temperature from 30-51 °C under 980 nm laser irradiation.	76
Figure 34. UV-Vis spectra at each step along the core-multishell synthesis. (---) AuNRs-CTAB, (----) AuNRs-NaOL, (----) AuNRs@Gd(OH) ₃ /GdOHCO ₃ :Er(III),Yb(III) and (----) AuNRs@Gd(OH) ₃ /GdOHCO ₃ :Er(III),Yb(III)@Gd(OH) ₃ /GdOHCO ₃ :Nd(III).	78
Figure 35. a) TEM image and EDS mapping of the AuNRs@Gd ₂ O ₃ :Er(III),Yb(III)@Gd ₂ O ₃ :Nd(III) after thermal treatment at 800 °C for 3h. b) Schematic synthesis procedure and HR-TEM images presenting the growing process of the Yb(OH)CO ₃ onto AuNRs (left) and EDX mapping images, and absorption spectra presenting the distributions and the absorption properties of gold in the calcined samples (right). Reproduced from ref. 97 copyright J. Phys. Chem. C 2014.	79

LIST OF TABLES

Table 1. <i>Lanthanoid properties. Adapted from ref 37.</i>	27
Table 2. <i>Average sizes dimensions and aspect ratio of the synthesized AuNRs.</i>	58

LIST OF ABBREVIATIONS

AuNPs – Gold nanoparticles
AuNRS – Gold nanorods
CET – Cooperative energy transfer
CTAB – Cethyltrimethylammonium bromide
CR – Cross relaxation
DS – Down shifting
DTA – Differential thermal analysis
EDTA – Ethylenediaminetetracetic acid
EDS – Energy dispersive scanning
EELS Electron energy loss spectroscopy
ESA – Excited state absorption
ETU – Energy transfer up-conversion
HMPNPs – Hybridmagneto-plasmonic nanoparticles
HMT – Hexamethylene tetramine
HR – High resolution
IR – Infrared
IONNPs – Iron oxide nanoparticles
LIR – Luminescence intensity ratio
Ln – Lanthanoids
LSPR – Localized surface plasmon resonance
NaOL – Sodium Oleate
NPs – Nanoparticles
NIR – Near infrared
PA – Photon avalanche
PTT – Photothermal therapy
QC – Quantum Cutting
SAED – Selected area electron diffraction

SET – Serial energy transfer

TEM – Transmission electron microscopy

TGA – Thermogravimetric analysis

UC – Up-conversion

XRD – X-ray Diffraction

CONTENTS

Chapter 1	19
Introduction	19
1.1. Gold nanoparticles properties and medical applications	20
1.2. Core-shell plasmonic heterostructures	25
1.3. Lanthanoids properties	27
1.4. Lanthanoid core-shell nanoparticles	29
1.5. Plasmon enhanced Fluorescence	34
1.6. Recent background of gold core-shell heterostructures on photothermal therapy. ...	41
1.7. Objectives and Justification	42
Chapter 2	44
Experimental procedures	44
2.1. Gold nanorods synthesis	45
2.1.1. Seed preparation	45
2.1.2. Synthesis and growth of the AuNRs	46
2.2. Synthesis of AuNRs@Gd ₂ O ₃ :Er(III), Yb(III)@Gd ₂ O ₃ :Nd(III)	47
2.2.1. Surfactant exchange	47
2.2.2. Formation of the core-shell structure	47
2.2.3. Thermal treatment	48
2.3. Characterization	49
2.3.1. Ultraviolet-visible spectroscopy (UV-Vis)	49
2.3.2. Infrared spectroscopy	49
2.3.3. Transmission electron microscopy (TEM)	49
2.3.4. Fluorescence spectroscopy	50
2.3.5. Thermogravimetric and differential thermal analysis	50
2.3.6. X-Ray Diffraction analysis (XRD)	50
Chapter 3	51
Results and Discussion	51
3.1. Gold nanorods synthesis	52
3.2. Synthesis of the AuNRs@Gd(OH) ₃ /GdOHCO ₃ :Er(III), Yb(III) ·H ₂ O precursor	58
3.3. Growth of the second shell of Gd(OH) ₃ /GdOHCO ₃ :Nd(III)	63
3.4. Synthesis of AuNRs@Gd ₂ O ₃ :Er(III), Yb(III)@Gd ₂ O ₃ :Nd(III)	65

3.5. Fluorescence and optical thermometry.....	71
3.6. Plasmon effect on the emission intensity.....	77
Chapter 4	81
Conclusions and future perspectives	81
Chapter 5	84
References	84

Chapter 1

Introduction

1.1. Gold nanoparticles properties and medical applications

Nanotechnology is one of the most studied research topics in the last century since it has a direct impact on the comprehension and development of different fields like molecular biology, physics, organic and inorganic chemistry, medicine and materials science¹. The optical, mechanic and physicochemical properties of nanometric materials differs from their bulk counterparts, and can be modified depending on the size, shape, surface characteristics and internal structure², allowing the design and application of new materials in areas like renewable energies, textile, biomedicine, healthcare, electronic and industrial processes.³ For example, gold is a rather non-reactive metal, however when the size is reduced to the nanometer scale, there is a drastic change in their electronic behavior, completely modifying its properties. Then gold nanoparticles (AuNPs) have interesting properties like high conductivity and catalytic activity for a wide variety of reactions such as oxidations of olefins, alcohols and alkanes, hydrogenations and aminations^{4,5}. These properties can be tuned by varying size particle, surface functionality, and intraparticle separation, facilitating the construction of electrochemical and electrocatalytic sensors⁶. One of the main features associated with the optical properties of these metallic NPs is the localized surface plasmon resonance (LSPR), defined as the collective oscillations of electrons present in the surface of metallic materials when an electromagnetic field of a specific wavelength is applied. The electric field of light interacts with the free electrons in the NP, leading to a charge separation between the free electrons and the ionic metal core; in turn coulombic repulsions among the free electrons acts as a restoring force that pushes the free electrons to opposite directions (Figure 1a), which results in the excitation of the LSPR (collective oscillation of electrons) and a strong absorption of light⁷⁻⁹.

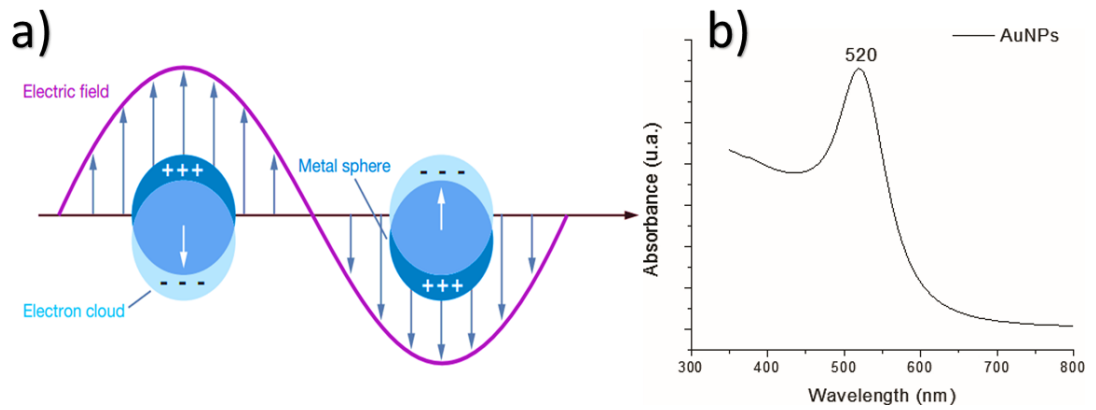


Figure 1. a) Schematic illustration of LSPR excitation for gold nanospheres. Reproduced from ref. 9 copyrights *Annu. Rev. Phys. Chem.* 2007. b) Typical LSPR band of gold nanospheres. Reproduced from ref. 8. Copyrights *Sensors Actuators, B Chem* 2014.

The plasmon frequency ω_p is given by:

$$\omega_p = \left(\frac{4\pi N e^2}{\epsilon_\alpha m^*} \right)^{1/2} \quad (1)$$

where N is the density of carriers (electrons or holes), m^* is the effective mass of carriers, e is the electron charge and ϵ_α is the medium permittivity. As can be noticed ω_p is proportional to the square root of N , for noble metal NPs, typical value of N is 10^{22} – 10^{23} cm^{-3} and the LSPR wavelength is in the visible region (Figure 1b). In addition, the plasmon frequency and strength depends on physical factors such as size, morphology, and geometrical arrangement; therefore, metal NPs of different sizes, shapes and materials show different absorption properties and thus may display different colors¹⁰. As is observed for AuNPs where by varying the synthetic conditions, it is possible to achieve different morphologies like nanospheres, nanorods, nanoshells, nanostars, and nanoprisms (Figure 2) with tunable LSPR bands in the visible or Near Infrared (NIR) region. Moreover, due to their low toxicity in biological systems and broad absorption spectral window (300-1000 nm), the optical and optoelectronic properties of AuNPs are widely applied in biomedicine in the detection of biomolecules such as proteins, pathogen agents, DNA and cancer cells¹¹.

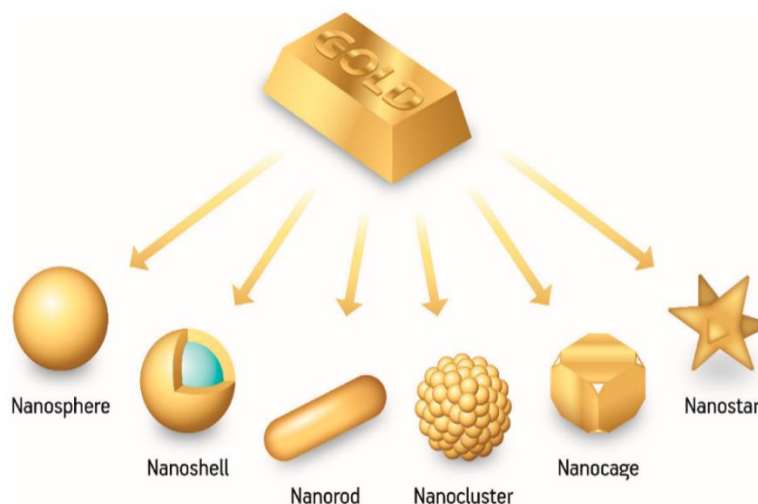


Figure 2. Representative scheme of the most common gold nanoparticle assemblies and morphologies. Reproduced from ref. 7. Copyright 2018 Journal of Nanomaterials.

From all these morphologies, the most studied are the nanospheres since their synthesis procedure is easy and well-established, and they show a strong LSPR band in the visible region between 500-530 nm depending on the NP diameter¹². Although in the last decades gold nanorods (AuNRs) have been the focus of a wide number of studies for biomedical applications^{13,14} since they show two LSPR bands, one located around 530 nm that corresponds to the excitation of the transverse mode of the rod, and a second one that corresponds to the longitudinal mode and can be redshifted towards higher wavelengths (usually centered between 600 and 1200 nm) as long as the aspect ratio of the AuNRs increases (Figure 3b-c). The energy difference between these two LSPR bands depends on the distribution of charge polarization, which is associated with the fact that in the longitudinal mode there is bigger charge separation in comparison to transverse mode (Figure 3a), thus the restoring force that determine the oscillation frequency decreases, reducing the energy of the longitudinal LSRP band; which in turn, is more intense due to the dipole strength¹⁵. Besides, AuNRs are highly sensitive to any change in the dielectric constant of the surrounding medium, which also leads to changes in the shape and position of the LSPR band^{13,16}. Therefore, one of the main advantages of use AuNRs instead of nanospheres or other morphologies for biomedical applications is the possibility of tuning the longitudinal LSPR band from the visible to the NIR region by increasing the aspect ratio in a controlled synthesis procedure, allowing deep tissue penetration of light. Since, as shown in Figure 4a there is a wavelength effect of light in the penetration of biological tissues where ultraviolet irradiation

(~100-380nm) would harm the cells during prolonged exposure times and cause photochemical reactions, and light in the visible region (~400-780 nm) can be readily absorbed by different pigments in the tissues hindering their penetration. Whereby, in order to achieve deeper tissue penetration according to the biological window (Figure 4b) and minimize photoinduced damage, the best option is the use of light in the NIR region as the irradiation source¹⁷⁻¹⁹.

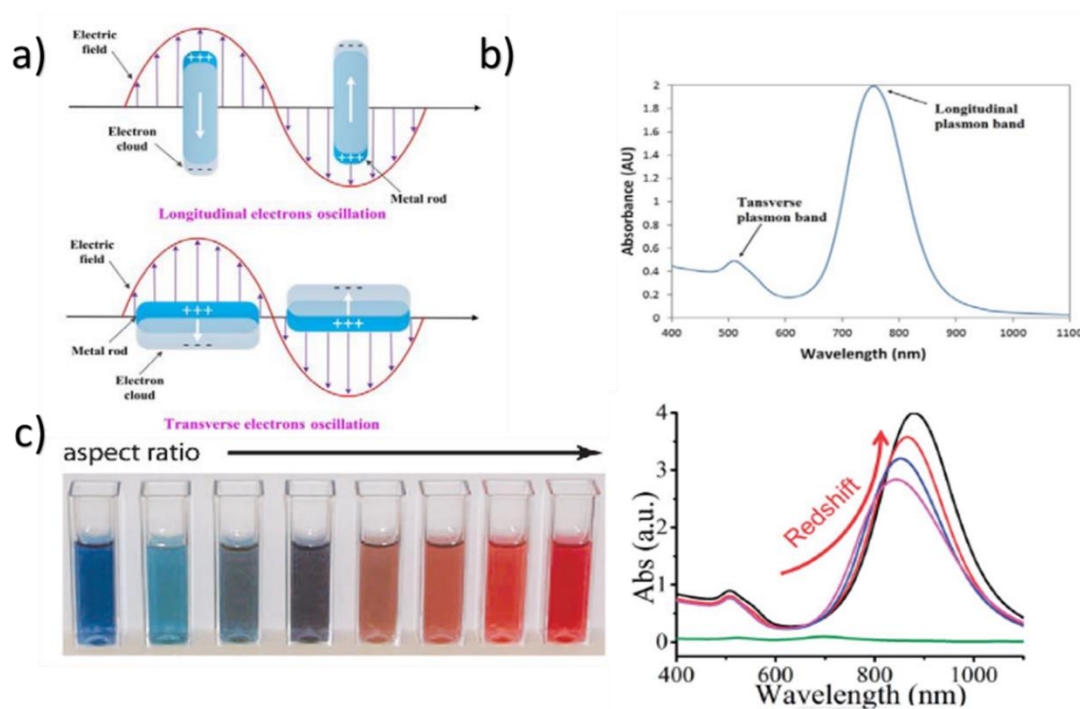


Figure 3. *a) Schematic illustration of longitudinal and transverse LSPR excitation for AuNRs. b) Longitudinal and transverse LSPR absorption bands of AuNRs reproduced from ref. 8 copyrights sensors and actuators B 2014 and c) Longitudinal LSPR band tuning and color change of the AuNRs as a function of the aspect ratio reproduced from ref. 20 copyrights Talanta 2018.*

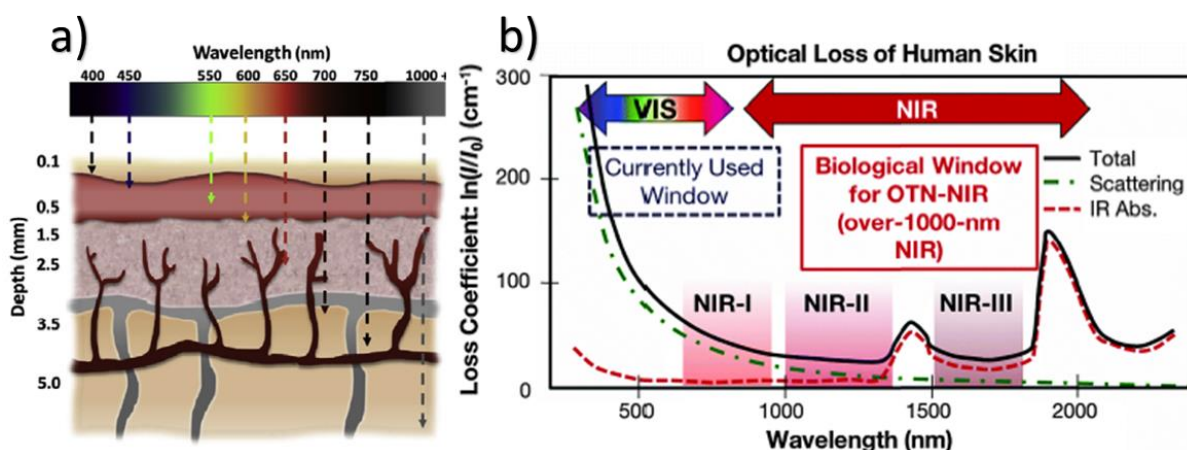


Figure 4. a) Wavelength effect in tissue penetration reproduced from ref. 62 copyrights royal society 2016 and b) biological spectral window reproduced from ref. 16 copyrights Nanoscale Horizons 2016.

In addition, due to their surface functionalization capacity, great biocompatibility and since do not generate light interferences or photoinduced damage^{20,21}, AuNRs are frequently used for *photothermal therapy* (PTT)^{14,22}, a process where a suspension of NPs is injected into a tumor tissue and then irradiated with a laser, exciting the LSPR band leading to a photothermal conversion of energy that induces the hyperthermia phenomenon. A treatment in which malignant cells are driven up to the cytotoxic level between 40 - 44 °C, which is the temperature range where tumor cells are more susceptible to heat than healthy tissue²³. In consequence, in this kind of treatments, it is necessary to adjust the irradiation conditions to achieve the desired range of temperatures that affect only the damaged cells. This range can be achieved by modifying the synthetic conditions to adjust the position of the LSPR band as a function of the aspect ratio as reported by Elahi et al²⁴. Then, AuNRs are an excellent choice for remote temperature readout, acting as nanoheaters and favoring imaging properties²⁵.

1.2. Core-shell plasmonic heterostructures

In order to design nanomaterials with improved optical properties and biological interactions for PTT and imaging applications, plasmonic metal heterostructures are emerging as potential theranostic platforms that improve the fluorescence imaging and phototherapeutic effect on cancer, based on their unconventional physical, chemical and electronic properties result of the sum of different components, as noble metals like Au, Ag, Pd, Pt and Cu; semiconductors based on oxides, fluorides or chalcogenides; quantum dots, lanthanoids, or organic polymers that improve the biological uptake^{26,27}.

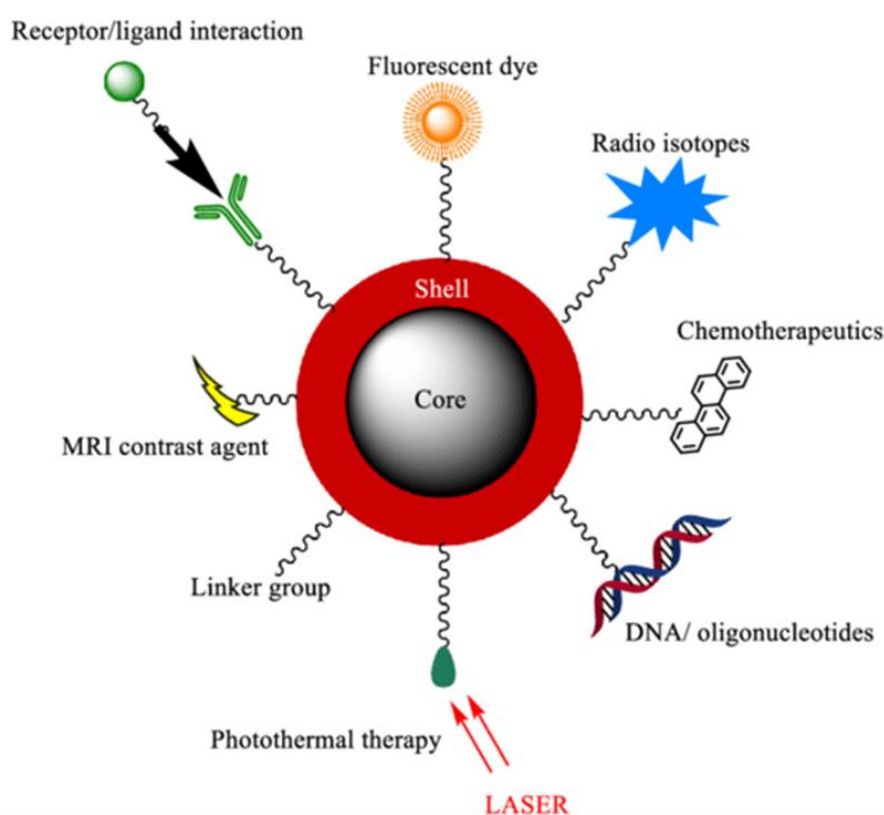


Figure 5. Core-shell NPs applications reproduced from ref. 29 copyrights Nanoscale Research Letters 2019.

Moreover, there is a wide variety of arrangements for plasmonic heterostructures, like multilayer photonic crystals; supported, decorated or doped materials, core-shell structures and so on²⁸. Among all of these, core-shell NPs are the most widely used in biological and PTT applications (Figure 5), since they could have major advantages over simple NPs and other heterostructures, like less cytotoxicity, improved dispersibility and biocompatibility,

increased thermal and chemical stability depending on the type of materials used as the core or the shell^{29,30}. For example, when the desired NPs are toxic, which is troublesome to the host tissues and organs, the coating with a benign material as an organic polymer on top of the core, makes the NPs much less toxic and biocompatible³¹. Sometimes, the shell layer may also improve the core material properties, as in the case of semiconductor core-shell NPs, where the shell could improve the photostability and optoelectronic properties³². Besides, when the core is susceptible to a thermal or chemical change when exposed to the surrounding environment, coating with an inert material could enhance the stability of the core particles³⁰.

As discussed in the last section, AuNRs are nanomaterials that show efficient theranostic activity due to their great photothermal conversion capacity, easy surface functionalization and the easy modification of their absorption properties by delocalizing the LSPR band as a function of the aspect ratio by controlling the synthetic conditions. Thus, taking advantage of these properties, many researchers have focused on the development of plasmonic core-shell heterostructures using AuNRs with different materials that improve their performance in PTT and other biomedical applications. For instance, Li et al³³, reported the synthesis of heterostructures metal-semiconductor based on AuNRs@Cu_{2-x}Se Core-shell NPs, showing improved photothermal conversion effect induced by the plasmonic coupling between these two materials. Additionally, Qi et al³⁴ synthesized AuNRs@SiO₂@ PEGylated graphene oxide NPs with high drug loading efficacy compared to traditional AuNRs@SiO₂; and improved photothermal stability and conversion associated with the GO-PEGylated coating. Moreover, Hu et al³⁵, reported enhanced photoluminescence intensity and bioimaging for AuNRs@CdSe/ZnS quantum dots NPs and Huang et al³⁶, synthesized AuNRs@Layered Double hydroxide@polyethylene glycol NPs showing potential applications in antibacterial wound-healing, tumor ablation, high photothermal efficiency and improved biological uptake. All these examples show the great versatility of the core-shell systems improving the optical properties, photothermal conversion capacity and biological interactions, when AuNRs are used as the core.

1.3. Lanthanoids properties

Lanthanoids (Ln), corresponds to the family of 15 elements from lanthanum ($4f^0$) to lutetium ($4f^{14}$) which are characterized by gradual filling of the 4f electron shell. Since the three stages of ionization enthalpy of lanthanoid elements are comparative low, they tend to form cations and assume trivalent ionic states Ln(III) and in some cases divalent (Samarium, Europium and Ytterbium) or tetravalent (Cerium, Praseodymium, Terbium and Lutetium) states³⁷ as shown in Table 1. Ln(III) species are hard acids, which are weakly influenced by ligands, because 4f orbitals are shielded from their electrostatic potential due to external 5s and 5p orbitals; therefore, they maintain their atomic character and do not have significant participation in covalent bonding formation, which in turn, determines their unique chemical, magnetic, and optical properties³⁸. Also, there is a contraction effect, which causes the atomic nucleus to strongly draw outer shell electrons as the atomic number increases due to small shielding of 4f electrons. Thus, there is a tendency for atomic and ionic radii to decrease with the increase of the atomic number^{39,40}.

Table 1. Lanthanoid properties. Adapted from ref 37.

Atomic number	Name	Symbol	Electron configuration	Valence	Ln (III) radius (pm)
57	Lanthanum	La	$5d^1 6s^2$	3	116
58	Cerium	Ce	$4f^1 5d^1 6s^2$	3;4	114
59	Praseodymium	Pr	$4f^3 6s^2$	3;4	113
60	Neodymium	Nd	$4f^4 6s^2$	3	111
61	Promethium	Pm	$4f^5 6s^2$	3	109
62	Samarium	Sm	$4f^6 6s^2$	2;3	108
63	Europium	Eu	$4f^7 6s^2$	2;3	107
64	Gadolinium	Ge	$4f^7 5d^1 6s^2$	3	105
65	Terbium	Tb	$4f^9 6s^2$	3;4	104
66	Dysprosium	Dy	$4f^{10} 6s^2$	3	103
67	Holmium	Ho	$4f^{11} 6s^2$	3	102
68	Erbium	Er	$4f^{12} 6s^2$	3	100
69	Thurium	Tm	$4f^{13} 6s^2$	3	99
70	Ytterbium	Yb	$4f^{14} 6s^2$	2;3	99
71	Lutetium	Lu	$4f^{14} 5d^1 6s^2$	3	98

In addition, the degeneracy lift of the 4f configuration occurs as described by the Russell-Saunders coupling, since the spin and orbital angular momentum of an electron confer on that electron a spin magnetic dipole and an orbital magnetic dipole. Thereby, the spin and orbital angular momentum may couple together magnetically via the magnetic dipoles they induce. Then, the ^{2S+1}L spectroscopic terms are originated, and the spin-orbit coupling (J) lifts the degeneracy of these terms leading to the $^{2S+1}L_J$ levels that are responsible for the electronic structure of the Ln (III) ions⁴¹ (Figure 6). Besides, when a Ln (III) ion is inserted into a chemical environment, as the 4f electrons are mostly localized in the inner shells the ligand-field effects on the electronic structures are very small, at the order of $\sim 100 \text{ cm}^{-1}$ ⁴². Although, despite the small magnitude of these effects, the $(2J + 1)$ degenerate J-levels are split by ligand-field resulting in a determined number of Stark sub-levels that depends on the site symmetry of the metal ion⁴³. Moreover, the electronic transitions observed for Ln (III) have a 4f-4f nature, with narrow absorption and emission bands of a few nanometers and shows small pseudo-stokes shifts.

The absorption and emission of light occurs thanks to operators derivative of the nature of light: the odd-parity electric dipole (ED) operator, the even-parity magnetic dipole (MD) and electric quadrupole (EQ) operators. Not all transitions are permitted since they have to obey selection rules. Then, ED 4f-4f intraconfigurational transitions are forbidden by Laporte ($\Delta l = \pm 1$) and spin ($\Delta S = 0$) selection rules; however, due to ligand-field perturbation that leads to the mixing of the $4f^n$ and $4f^{n-1} 5d^1$ configuration, this rule is relaxed and the transition is called induced or forced electric dipole transition. Thus, a more correct meaning for a forbidden transition is that it has a low probability of occurring, while an allowed transition has a high probability, in consequence compared to other^{43,44}.

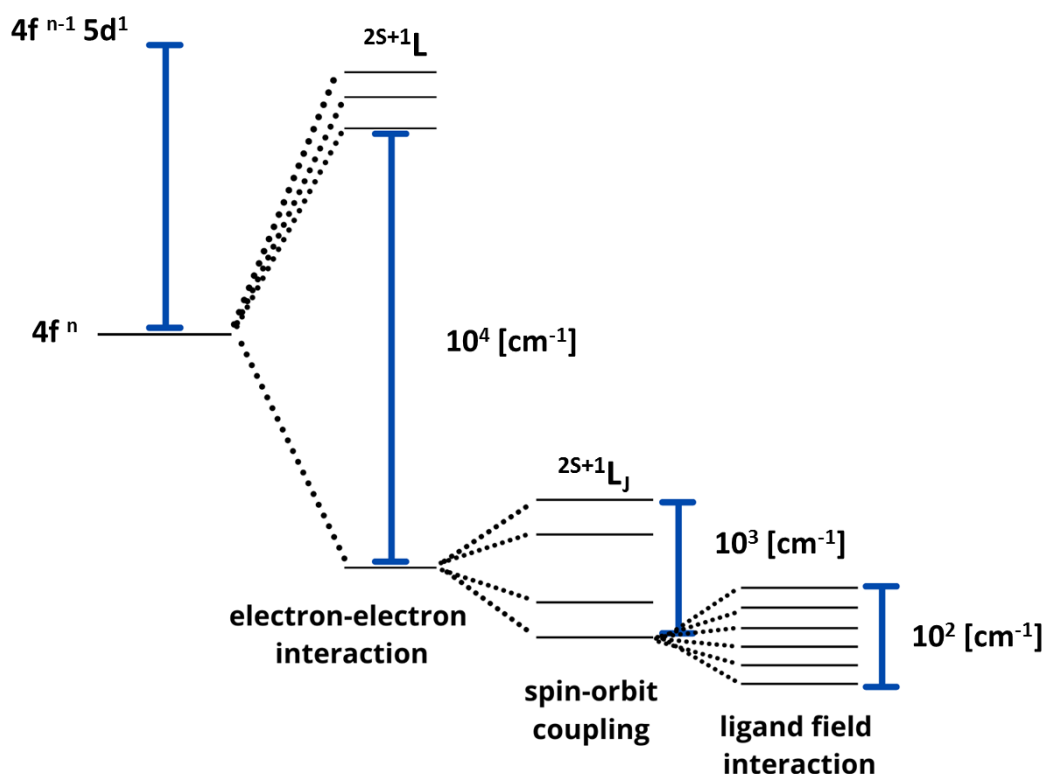


Figure 6. Energy scale of the electronic structure of lanthanoid ions. From left to right, electron-electron interaction, spin-orbit coupling, and ligand field effect. Adapted from ref. 39. Copyrights American Chemical Society 1995.

1.4. Lanthanoid core-shell nanoparticles

On the other hand, Ln ions are widely used in the design of core-shell heterostructures due to properties such as narrow emission bands, high chemical stability, minimized autofluorescence, low toxicity⁴⁵, and the possibility of combining diverse Ln elements, leading to different energy transfer processes as Up-Conversion, Down Shifting and Quantum Cutting, which promotes energy emissions in the visible and NIR region that can be tapped for biomedical and spectroscopy applications⁴⁶. Up-Conversion (UC) confirmed for first time in 1973 by Auzel⁴⁷, is an anti-stokes process where multiple low energy photons are converted into one photon of higher energy⁴⁸. Otherwise, the UC phenomenon involving trivalent Ln(III) ions is a non-linear process that relies on 4f-4f electronic transitions and is generally characterized by absorption in the NIR region followed by radiative emission within the near-ultraviolet, visible, or NIR ranges through three main processes:

- a) *Energy transfer UC (ETU)*: A UC phenomenon result from the interaction between the same or different Ln ions. The energy is transferred by cross relaxation in the form of non-radiative coupling of ions. According to the different modes of transmission, ETU is divided into three main types: serial energy transfer (SET), cross relaxation (CR) and cooperative energy transfer (CET) as shown in Figure 7a.
- b) *Excited State Absorption (ESA)*: A continuous multi-photon absorption process where the same Ln ion is excited from ground-state to an excited-state energy level through continuous two-photon or multi-photon absorption, followed by the release of energy in the form of light, through a radiative decay (Figure 7b).
- c) *Photon Avalanche (PA)*: Is the result between the interaction of ESA and ETU-CR (Figure 7c). The energy difference between excited light $h\nu_1$ and E_2 and E_3 is the same. Then, ions located at E_2 level absorb the energy and are excited to the excited state level E_3 by cross-relaxation process, and the emitters ions at E_1 and E_3 levels are excited. All of them converge on the E_2 level, so the number of photons on the E_2 sharply increases.

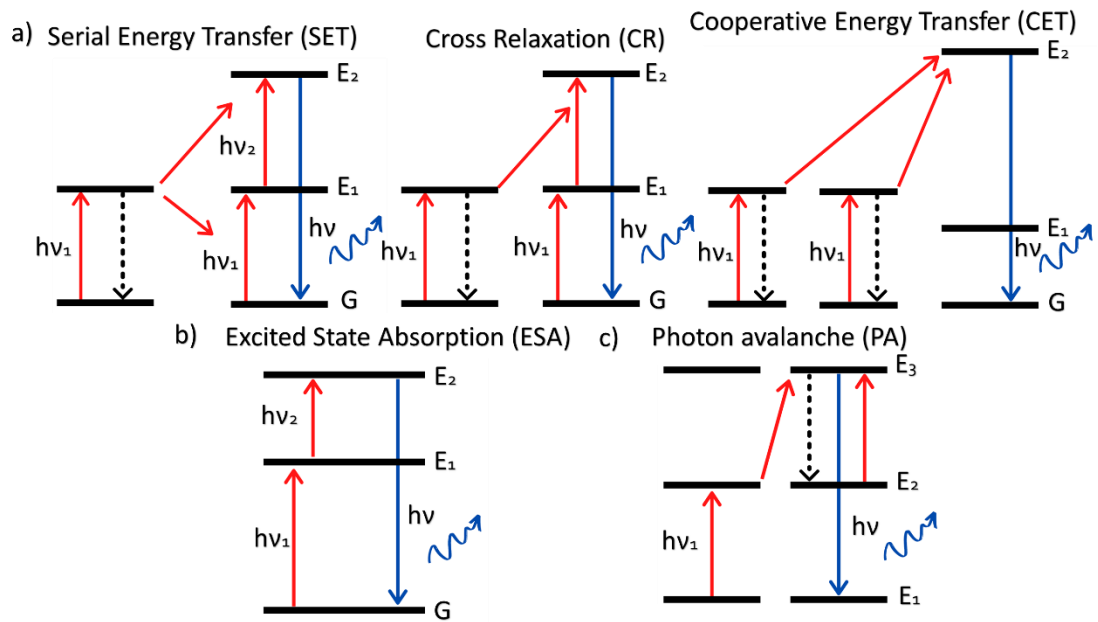


Figure 7. Up-Conversion main processes. a) Energy transfer UC (ETU), b) Excited State Absorption (ESA) and c) Photon avalanche (PA).

In addition, UC nanomaterials are usually developed with a common scheme that consists of activators and sensitizers made up of Ln ions and matrix materials such as oxides, halides, fluorides or sulfur compounds²⁸. Activators are the center of luminescence, and sensitizers transfer their absorbed energy to the activators improving their luminescence efficiency; while matrix materials themselves are not luminescent but can provide suitable lattice sites for activators⁴⁹. The key photophysical steps involved in the UC process are illustrated in Figure 8a as follows: i) Absorption of excitation photons by sensitizers; ii) energy migration between sensitizers ions until reach the activator; iii) energy storage on an intermediate state of the activator; iv) promotion of the intermediate level of the activator to a emitting level, after a second energy migration event; and v) radiative emission from the higher energy level of the activator. The probability occurrence and efficacy of each of these steps is related to intrinsic characteristics of the material such as phonon density of states, local symmetry and distance between optically active elements (Figure 8b), all these characteristics are associated with the fundamental arrangement of atoms. Then, UC emissions are not just related to its constituent atoms, but intricately linked to the locations (and interactions) of the constituent atoms within the NPs⁴⁸.

Otherwise, opposite to the UC phenomenon, down shifting (DS) and Quantum cutting (QC) are Stokes phenomena where due to the interactions between electrons and phonons, there is an internal energy relaxation process, and as a result, a longer-wavelength photon will be emitted (Figure 9). Then, DS is a process in which a high-energy photon is converted in lower energy photons via radiative/non-radiative transitions to low lying fluorescing states⁵⁰ and QC is a process in which a high-energy photon is converted into two or more lower-energy photons with quantum efficiency bigger than 100%⁵¹. These processes usually involve absorption of photons in the UV or visible region and emission in the NIR range. For these reasons, compared to traditional luminescent nanomaterials as organic dyes and quantum dots; core-shell NPs with Ln ions have numerous advantages for biomedicine, such as improved penetration depth, minimized autofluorescence, low radiation damage and cytotoxicity, high chemical and optical stability and improved potential for PTT due to the possibility of modulate the emission region depending on the pair of ions used as sensitizer and activator, the irradiation source and the morphology of the NPs^{28,52}. Allowing these heterostructures to act as an ideal multifunctional platform capable of simultaneous imaging, detection, and therapy⁴⁶.

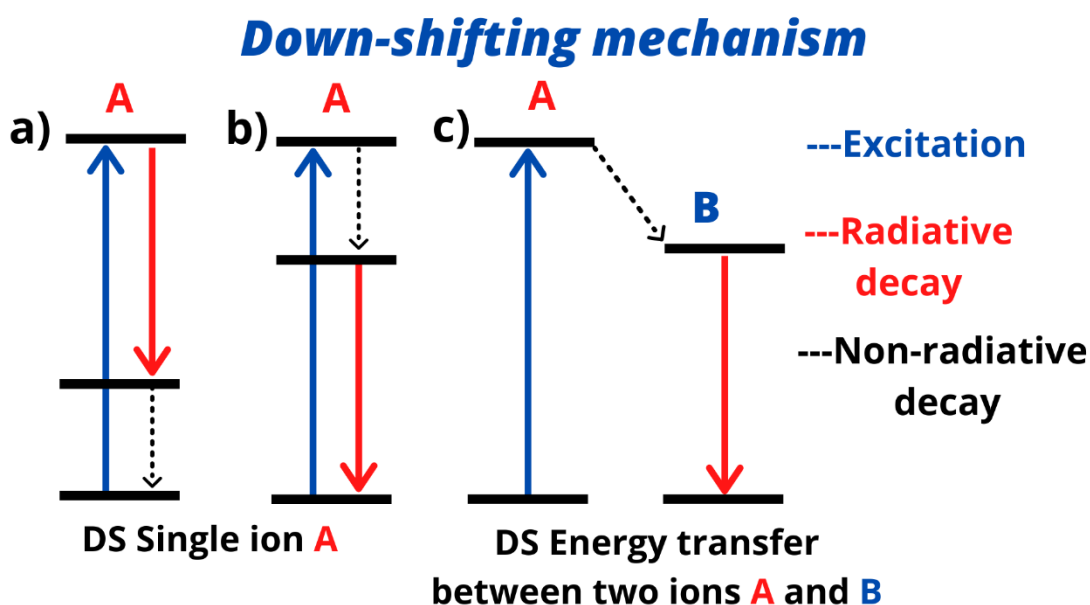


Figure 9. Schematic illustration of down-shifting general process **a)** and **b)** single ion **c)** Non-radiative energy transfer from a Ln ion A to B. (the energy in excess is dissipated by phonons). Adapted from ref 56. Copyrights ACS Nano 2019.

1.5. Plasmon enhanced Fluorescence

As shown in the above section, the design of core-shell heterostructures including Ln ions introduces a wide number of advantages for biological and spectroscopic applications. However, the UC efficiency reported for Ln ions is relative low, due to unfavorable features as surface-related quenching effects (surface defects, high-energy vibrations of solvent and/or ligand molecules) and the intraconfigurational dipole-dipole forbidden nature of 4f-4f transitions, that results in lower absorption bands and extinction coefficients compared to organic dyes, giving rise to weak light absorption of the NPs^{49,53,54}. Thus, in order to improve these features, have been employed some modifications, such as the design of core-multishell structures where by synthesizing different layers in which activator and sensitizer ions are separated through inert matrix layers, can occur multiple transfer energy steps that decrease the concentration quenching effects by suppressing cross-relaxation processes, leading to improved energy transfer UC at the interface, especially for multi-photon processes⁵⁵. Additionally, depending on the Ln ion used and their concentration along the shells, other mechanisms can be favored improving DS or QC emissions^{56,57}.

Another strategy that has been applied, is the use of organic dyes that acts as an antenna with larger cross-sections and broad absorption bands that improves light harvesting⁵⁸, although these antennas must match with the excitation band of the sensitizer ion, and also need to be far away from the absorption band of the interested UC emission, since the emission intensity could be quenched through a reabsorption process. Then, to overcome UC quenching associated with surface-related defects, have been explored the synthesis of epitaxial core-shell nanostructures linked to organic dyes that allow broadly infrared-harvesting through multistep cascade energy transfer with a sequential non-radiative energy transfer to up-converting ion pairs in the core, that results in enhanced UC efficiency⁵⁹. In addition, plasmon enhanced fluorescence arises as a promissory alternative that allows improved light harvesting and enhanced emission intensity through DS, QC or UC processes by matching the absorption or emission band of the Ln ions with the LSPR band of a metal or semiconductor in a plasmonic heterostructure⁶⁰. Likewise, luminescence from a fluorophore can be generally characterized in terms of the internal quantum yield and lifetime, and either the excitation or emission of the light emitter can be enhanced, then the effect of a plasmonic material on the luminescence of a fluorophore could be described as follows: After the fluorophore irradiation, it will be excited from the ground state to a higher energy level,

then the excess of energy will be released in the form of a photon (light) or a phonon (vibration), through radiative and non-radiative decays respectively (Figure 10b). The rates at which the radiative and non-radiative transitions will occur are denoted by the terms Γ and Γ_{nr} , respectively. These two decay rates determine the internal quantum yield, Q , and lifetime, τ , of a fluorophore.

$$Q = \frac{\Gamma_0}{\Gamma_0 + \Gamma_{nr}} \quad (2)$$

$$\tau = \frac{1}{\Gamma_0 + \Gamma_{nr}} \quad (3)$$

The quantum yield of a de-excitation process refers to the efficiency ratio of events corresponding to that process with respect to the total number of excitation events, or, equivalently, the probability of each type of de-excitation event⁶¹. Thus, the quantum yield for luminescence (Eq. (2)) is the rate of photon emission events over the summed rate constants of all de-excitation events, in summary it denotes the "emission efficiency". Otherwise, the luminescence lifetime (Eq. (3)) is the amount of time that a fluorophore exists in the excited state before returning to the ground state, in other words, the time necessary to observe a population decay of $1/n$. When a fluorophore is placed near a metallic surface, the interaction between the two materials results in a modified quantum yield, Q_m , and lifetime, τ_m as denoted in the equations (4) and (5):

$$\tau = \frac{1}{\Gamma_0 + \Gamma_m + \Gamma_{mnr} + \Gamma_{nr}} \quad (4)$$

$$Q_{fm} = \frac{\Gamma_0 + \Gamma_m}{\Gamma_0 + \Gamma_m + \Gamma_{mnr} + \Gamma_{nr}} \quad (5)$$

where Γ_m represents the modified radiative decay rate and Γ_{mnr} the additional non-radiative decay channels introduced by the presence of the metal NP (Figure 10b). Considering this, a plasmonic material could influence a near emitter in three main processes⁶²⁻⁶⁵:

1) Within the excitation of the LSPR band, the metal NPs can act as an antenna and locally concentrate the incident field enhancing the absorption by improving the reception of light.

2) If the distance between the fluorophore and the NPs is appropriate 5-35 nm (the distance dependence is characteristic of every material)⁶⁶, the radiative decay rate Γ_m increases while the Γ_{mnr} term becomes insignificant, giving rise to enhanced fluorescence.

3) If the fluorophore is too close to the metallic surface (1-5 nm), it will increase the non-radiative decay rate, then the Γ_{mnr} term dominates the equation leading to a fluorescence quenching.

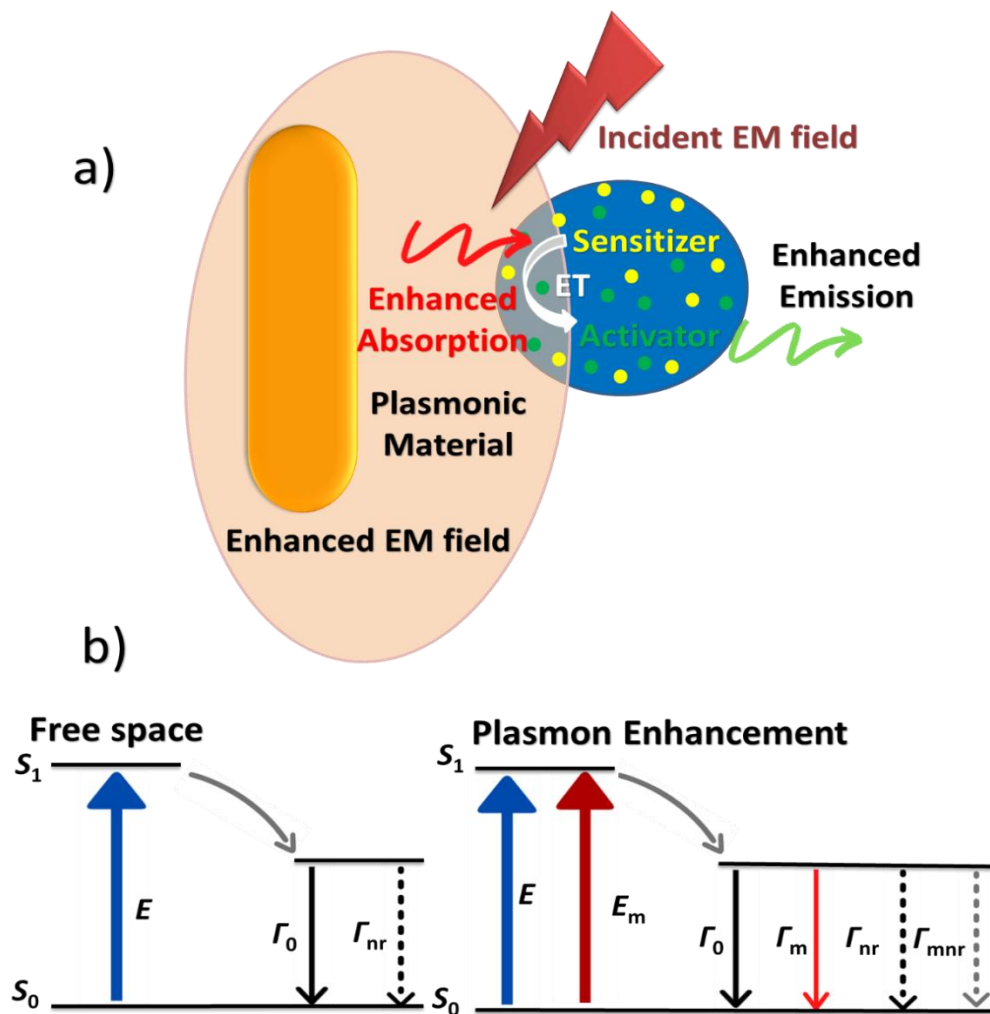


Figure 10. a) Schematic illustration of the plasmon enhancement fluorescence on fluorophore. Adapted from ref. 50. *Rev. Phys.* 2019. b) Jablonski diagram showing the pathways through which energy is transferred between energy states when a fluorophore is in the absence or presence of a metallic NP. Adapted from ref. 62. Copyrights Materials Today advances 2020.

On the other hand, if the fluorophore is placed too far from the particle, it would not experience the enhanced electric field and neither Γ_m nor Γ_{mnr} will have any significant impact, then the fluorophore will act as if it is in free space.

In further detail, exciting the nanoparticle at its LSPR wavelength results in greatly amplified absorption and scattering that will enhance the near-field intensity of the electric field surrounding it; in turn, if the fluorophore is placed within this near-field, both the excitation and emission rates will be modified resulting in enhanced luminescence. (Figure 10a). Additionally, in the free space condition, once the fluorophore is ready to relax to its ground state, it can only relax through either radiative or non-radiative pathways; however, in the presence of the metal nanoparticle, depending on the distance⁶⁶ an additional radiative decay path, Γ_m , is created, allowing the fluorophore to emit a higher number of photons than previously possible and thus enhance the emission intensity⁶² (Figure 10b). On the other hand, if the nanoparticle and the fluorophore are very close to each other, new relaxation paths will be generated whereby energy can pass due to the coupling between the LSPR band and the dipole of the excited fluorophore, enabling non-radiative energy transfer from the fluorophore to the plasmonic material, the opposite process is not observed since metallic plasmons have lifetimes in the order of 10^{-12} - 10^{-14} s while common fluorophores such as Ln ions, Quantum Dots and organic dyes have lifetimes between 10^{-6} - 10^{-9} s. Moreover, the maximum enhancement of the fluorescence is achieved if the LSPR wavelength is equal to the excitation (UC) or emission (DS and QC) wavelength of the fluorophore. Then, different works^{63,67,68} reported that by adjusting the overlap of the emission or absorption band of the fluorophore with the LSPR band of the plasmonic material, it is possible to enhance the DS, QC or UC emissions on the same core-shell structure. Two possible mechanisms have been discussed in order to explain how can be favored one process or another:

- 1) The UC mechanism is related to absorption matching since the LSPR band of the metal is near to the excitation wavelength of the Ln ions, which by the influence of the enhanced electric field increases the excitation rate from the ground state, enhancing the emission intensity. Thus, the UC Intensity is proportional to E^{2n} for an n-photon process²⁹. The greater the number of photons necessary to populate the emitting state, the more sensitive the emission intensity will be to any change in E.

2) On the other hand, the QC and DS mechanisms are associated with emission matching, in this case the LSPR band of the NPs is close to the emission band of the Ln ions. The enhanced electric field increases the rate of the radiative transitions, therefore, quantum yield and emission intensity are enhanced.

For instance Lin et al⁶⁸ reported the synthesis of AuNRs@SiO₂/NaYF₄:Tb(III),Yb(III)@NaYF₄ core-shell NPS (Figure 11a). The AuNRs shows two LSPR bands corresponding to the transversal and longitudinal modes at 530 and 980 nm respectively (Figure 11b); and were coated with SiO₂ layers of different thickness ranging between 0-45 nm in order to study the effect of the distance between the plasmonic material and the emitter Tb(III) and Yb(III) ions. Fluorescence measures were carried out under an excitation wavelength of 372 nm according to the transition $^7F_6 \rightarrow ^5D_3$ of Tb(III) that leads to the QC emission at 980 nm associated with the transition $^2F_{5/2} \rightarrow ^2F_{7/2}$ of Yb(III) (Figure 11 c left). Additionally, the NPs were excited at 980 nm according to the transition $^2F_{7/2} \rightarrow ^2F_{5/2}$ of Yb(III) that results in the UC emission peaks located at 486 nm, 543 nm, 584 nm and 620 nm attributed to $^5D_4 \rightarrow ^7F_j$ transitions (j=6, 5, 4, 3) of Tb(III) (Figure 11 d left). Results show that, as was previously discussed for both UC and QC processes, the emission intensity is improved as long as the thickness of the SiO₂ layer increases reaching a maximum enhancement at 35 nm (Figure 11 c-d right). In addition, the maximum enhancement in the UC emission intensity is achieved when the excitation band of the fluorophore (Yb(III) $\lambda_{exc}=980\text{nm}$) and the longitudinal LSPR band of the AuNRs overlaps; while for the QC process, the enhancement is maximum when the emission band of the Ln ions and the LSPR band of the AuNRs matches.

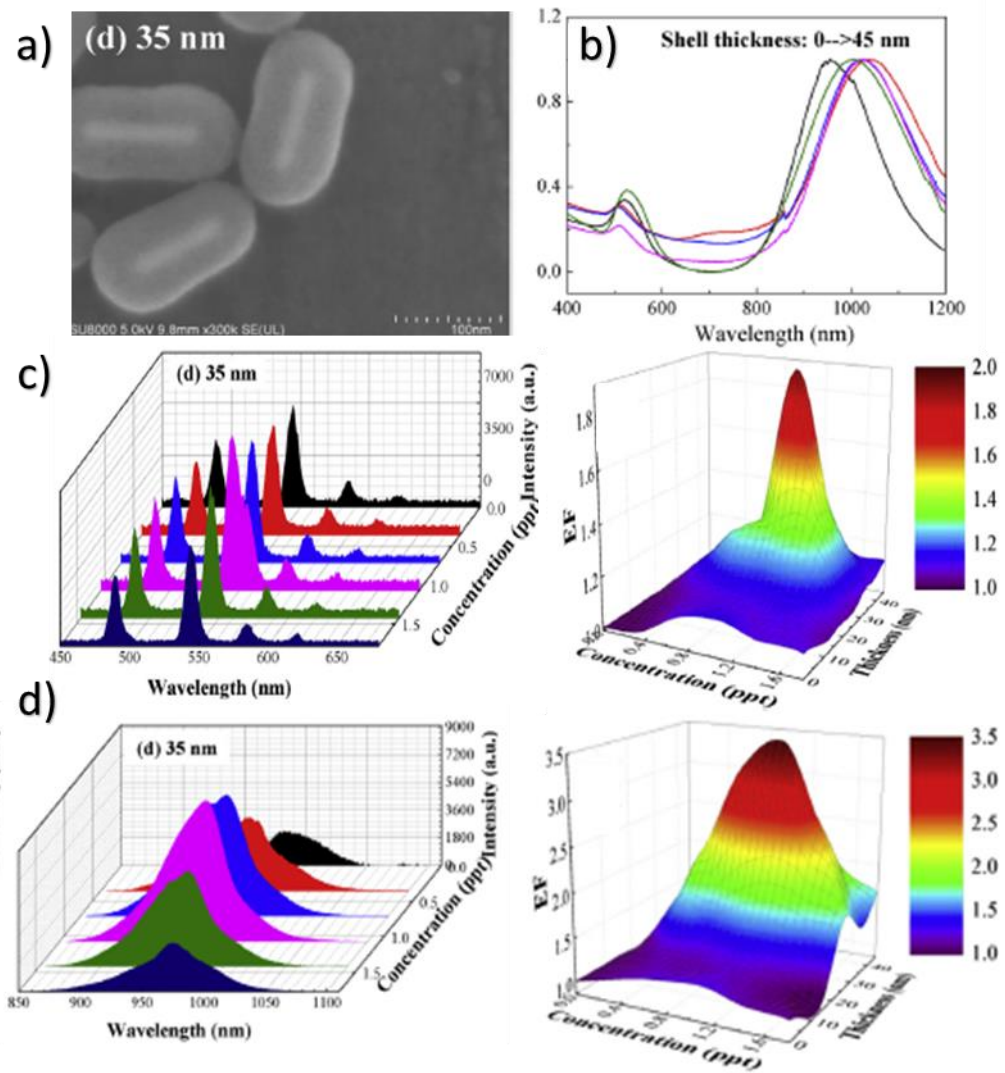


Figure 11. *a)* Transmission electron microscopy image of the AuNRs@SiO₂/NaYF₄:Tb(III),Yb(III)@NaYF₄ core-shell NPs with a SiO₂ thickness layer of 35 nm. *b)* Absorption spectra as a function of the SiO₂ thickness 0-45 nm. *c)* UC emission spectra $\lambda_{exc} = 980$ nm (left), enhancement factor as a function of the SiO₂ thickness and NP concentration (right). *d)* QC emission spectra $\lambda_{exc} = 372$ nm (left), enhancement factor as a function of the SiO₂ thickness and NP concentration (right). Reproduced from ref. 68. Copyrights J. Lumin. 2019.

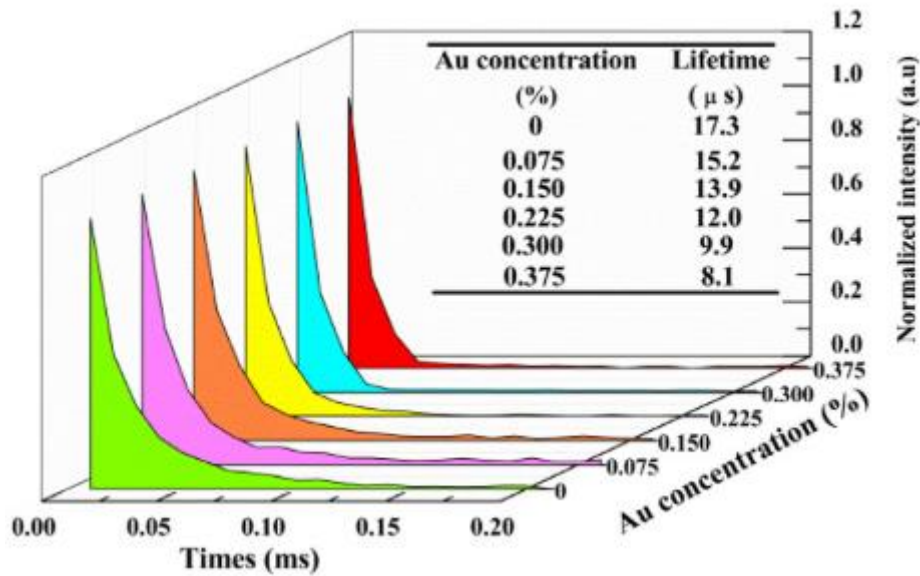


Figure 12. Luminescence decay curves of Er(III) $^4I_{11/2} \rightarrow ^4I_{15/2}$ transition ($\lambda_{exc} = 486 \text{ nm}$, $\lambda_{em} = 977 \text{ nm}$) in $\beta\text{-NaYF}_4\text{:Er(III)}$ NPs decorated $x\%$ Au NRs ($x = 0, 0.075, 0.15, 0.225, 0.3, 0.375$). Inset: Calculated lifetimes of Er(III) $^4I_{11/2}$ excited state decorated with $x\%$ Au NRs ($x = 0, 0.075, 0.15, 0.225, 0.3, 0.375$). Reproduced from ref 60. Copyrights Opt. Commun 2019.

In addition, the life time of the Yb(III) and Tb(III) ions decrease by increasing the AuNRs@SiO₂ concentration, probably associated with the new decay paths induced by the enhanced electric field and the coupling of the metallic surface with the Ln ions, which could increase the radiative and non-radiative decay rates. These results are in well agreement with the ones reported by Huang et al⁶⁰, where by decorating $\beta\text{-NaYF}_4\text{:Er(III)}$ NPs with AuNRs, the life time of the Er(III) ions decrease as long as the AuNRs concentration increases (Figure 12). Thus, as shown above, there are many parameters that could influence the emission intensity when a plasmonic material is positioned near to a Ln ion, additionally to the distance between the plasmonic material and the fluorophore, and the matching of the absorption or emission band with the LSPR band of the metal, the quenching or enhancement of the emission intensity also depends on several factors such as overlap of the polarization field, plasmonic material, heterostructure morphology and pump power⁶⁹⁻⁷¹. Then, plasmon enhanced fluorescence in metal heterostructures is a promissory field for biological, PPT and spectroscopic applications. However, it still requires further research.

1.6. Recent background of gold core-shell heterostructures on photothermal therapy.

In 2018 Mohammadniaei et al⁷², developed bifunctional Au@Bi₂Se₃ core-shell NPs for synergetic therapy by surface enhanced Raman scattering traceable *Antagomi R* delivery and PTT. Results shows that by encapsulating Bi₂Se₃ with Au there is an improvement on the surface functionalization and biocompatibility by 18.6% and it also maintained the plasmonic features allowing this SERS-active heterostructure to real time release and monitoring on in vitro *antagomi R*. Further functionalization with a PVP-FA/ CPP-dsRNA peptide leads to an increase of the cellular uptake efficiency by 87% and improved PTT cancer treatment (~98% cell death). Also in 2018 Ovejero et al⁷³, reported the synthesis of hybrid magneto-plasmonic NPs (HMPNPs) based on iron oxide NPs (IONPs) and AuNRs as colloidal nanoheaters, showing that the hybrid samples display a larger coercive field, which induces greater heating at high magnetic fields than the IONPs. Besides, the heat generated by IONPs and AuNRs in photothermal heating can be combined using HMPNPs. However, the plasmonic interaction between the phases reduces the amount of heat released with respect to a mixed colloid decreasing their efficiency for PTT applications. Otherwise, in 2019 Wang et al⁷⁴, reported the fabrication of GdOF:Yb/Er@(AuNRs@BSA) NPs with flexible switch ability of fluorescence imaging and PTT using 808 and 980 nm lasers as irradiation source. The concentration and accumulation of AuNRs over the UCNPs lead to enhanced photothermal conversion. Moreover, the UC emissions of the core can also be achieved with less NIR absorption and lower temperature increase under 980 nm laser irradiations, which is especially beneficial for maintaining security and reducing normal cell killing during in vivo diagnosis. In addition, BSA-coating and FA-conjugating were employed to effectively promote the HeLa cell uptake of the heterostructure, facilitating non-tumor site alleviation and target high-efficiency PTT. Additionally, in 2020 Dong et al⁷⁵, reported the synthesis of NaGdF₄:Yb(III)Er(III)@NaYF₄@AuNPs via solvothermal method. These core-shell UCNPs were employed as nanoscale light sources of which AuNPs efficiently absorbed green emission centered at 540 nm with an average diameter of 4 nm. As a result, green emission of UCNPs could not penetrate the coating of the AuNPs without being absorbed. It was determined a photothermal conversion efficiency of 41.2% which is lower compared to AuNPs with other morphologies as nanorods or nanostars. Moreover, fluorescent resonance

energy transfer mechanism from UCNPs to AuNPs was confirmed to be the predominant route for this nanoscale photothermal system (UCNPs@Au), instead of direct photon absorption.

As shown in the literature review, most of the core-shell nanostructures used for PTT applications are based on compounds of NaYF₄ or NaGdF₄ doped with Ln ions like Eu(III), Er(III), Yb(III) or Nd(III) that improves the photothermal efficiency taking advantage of the UC, QC or DS phenomena⁷⁶⁻⁷⁹. In order to further improve the efficiency of these materials, Zhang et al⁸⁰ (2018), fabricated NaYF₄:Er(III)·Yb(III)@NaYF₄ UCNPs conjugated with AuNRs, which has the capacity of simultaneously generating heat and real-time temperature sensing through the hyperthermia phenomena generated for the plasmonic material and the temperature dependence of the luminescence intensity, showing efficient photothermal conversion which might make a significant step towards the achievement of real-time controlled PTT. Additionally, Parchur et al⁸¹, developed theranostic NPs of AuNRs@Gd₂O₃:Ln(III) (Ln = Yb/Er) for in vivo treatment of mice tumor cancer cells showing higher photothermal conversion efficiency when the NPs were doped with Yb(III) and Er(III) ions, efficiently ablating the animal tumors through PTT. Moreover, the magnetic properties of Gd(III) ions improved the ability of the theranostic NPs as contrast imaging agent for magneto resonance imaging making these kind of heterostructures a promissory alternative in PTT for cancer treatment.

1.7. Objectives and Justification

As discussed in the literature review, coating AuNRs with lanthanoid oxides under a controlled synthesis procedure derives in heterostructures with tunable size, morphology, crystal phase, and specific surface functionalization. This improves the phenomena of UC, QC and or DS depending on the matching between the LSPR band of gold and the excitation or emission wavelength of the Ln ions respectively. Allowing these materials to enhance the optical signal in fluorescence and improve their photothermal efficiency.

Thus, the purpose of this research is to carry out the synthesis of core-multishell hierarchical nanostructures using AuNRs, coated with $\text{Gd}_2\text{O}_3:\text{Er(III),Yb(III)}$ and $\text{Gd}_2\text{O}_3:\text{Nd(III)}$, in order to improve the emission of the system in the visible and NIR region by controlling the aspect ratio of the AuNRs. To locally control the enhancement of the UC and DS processes through plasmon enhanced fluorescence. The proposed system may act as a thermal sensor and have potential applications of bioimaging and hyperthermia treatments by providing both optical tracking and photothermal capacity.

In order to achieve this goal, some specific objectives were proposed:

- 1) Synthesize AuNRs controlling the aspect ratio in order to modulate the longitudinal LSPR band to 800-980 nm.
- 2) Synthesize $\text{AuNRs@Gd}_2\text{O}_3:\text{Er(III),Yb(III)}$ through surfactant exchange and solvothermal methods.
- 3) Synthesize the core-multishell system: $\text{AuNRs@Gd}_2\text{O}_3:\text{Er(III),Yb(III)@Gd}_2\text{O}_3:\text{Nd(III)}$ in order to enhance the emission intensity of the Ln ions in the visible and NIR region.
- 4) Optical thermometry at different excitation wavelengths (808 and 980 nm).
- 5) Photothermal evaluation through hyperthermia measures of the final product.

Chapter 2

Experimental procedures

2.1. Gold nanorods synthesis

For the synthesis of the AuNPs, hydrogen tetrachloroaurate (III) trihydrate ($\text{HAuCl}_4 \cdot 3\text{H}_2\text{O}$, $\geq 99.9\%$), cetyltrimethylammonium bromide (CTAB, $\geq 99\%$), sodium borohydride (NaBH_4 , $\geq 99.99\%$), silver nitrate (AgNO_3 , $>97\%$), were purchased from Sigma-Aldrich. Hydrogen peroxide (H_2O_2 , 30%) and sodium hydroxide (NaOH , $>97\%$) were purchased from Anidrol and Synth, respectively. The glassware was cleaned with aqua regia solution (3:1 v/v, $\text{HCl}:\text{HNO}_3$) and washed with deionized water before the synthesis. For the sample decomposition, all reagents were purchased from Merck, and for microwave-assisted acid decomposition and standard/sample dilutions, sub-boiling nitric acid was employed. Before using, all glassware was cleaned with HNO_3 10% (v/v) and rinsed with deionized water.

All the reagents were prepared in aqueous solution, it was used deionized water (≥ 18.2 $\text{M}\Omega$ cm) from a Milli-Q water purification system (Millipore).

The synthesis of the AuNRs was carried out according to the method described by Xu D. et al⁸², using hydrogen peroxide as the reducing agent under basic conditions by varying the $\text{H}_2\text{O}_2/\text{Au(III)}$ ratio with different amounts of NaOH , AgNO_3 . This methodology was chosen because it allows the control of the size and morphology of the AuNRs in order to set the aspect ratio that leads to longitudinal LSPR bands between 800-980 nm which matches with the excitation or emission bands of the Yb(III) and Nd(III) ions.

2.1.1. Seed preparation

First, 32 μL of a 78.6 mmol L^{-1} HAuCl_4 solution were mixed with 4 mL of a 0.1 mol L^{-1} CTAB solution. Finally were added, 24 μL of a 0.1 mol L^{-1} NaBH_4 solution under vigorous stirring for 2 min. The reaction mixture was aged in a 28 °C water bath for at least 2 h before use (Figure 13).

2.1.2. Synthesis and growth of the AuNRs

For the second step, 20 μL of a 0.1 mol L^{-1} AgNO_3 solution and 668 μL of a 78.6 mmol L^{-1} HAuCl_4 solution were added to 50 mL of a 0.1 mol L^{-1} CTAB stock solution. Then, 163 μL of a 1 mol L^{-1} NaOH solution (pH ~ 11.8) and 27.5 μL of a 30% v/v H_2O_2 solution were added under stirring for 30 s. Next, 150 μL of the above seed solution were sequentially added and stirred for another 30 s and kept at 28°C in a water bath for at least 1.5 h. Finally, the solution was centrifuged at 5510 g for 30 min followed by the removal of the supernatant. The precipitate was redispersed in 10 mL and stored at 25°C to avoid crystallization of the CTAB surfactant.

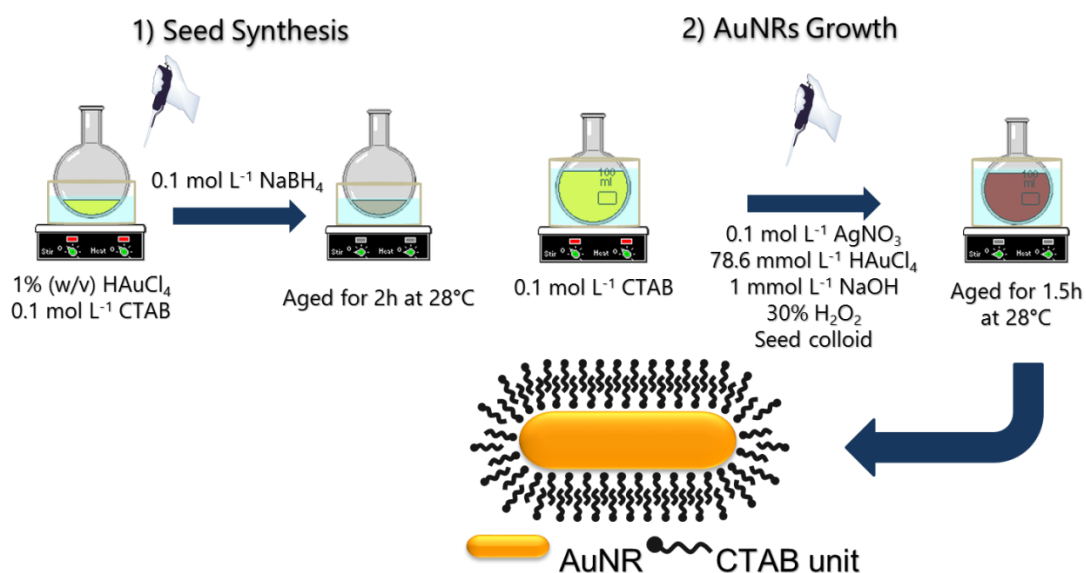


Figure 13. Schematic illustration of the synthesis procedure of AuNRs with H_2O_2 as the reducing agent under basic conditions.

2.2. Synthesis of AuNRs@Gd₂O₃:Er(III), Yb(III)@Gd₂O₃:Nd(III)

For the synthesis of the core-shell NPs, hexamethylene tetramine (HMT $\geq 99.9\%$), sodium oleate (NaOL $\geq 99.9\%$), gadolinium (III) oxide (Gd₂O₃ $\geq 99.9\%$), erbium (III) oxide (Er₂O₃ $\geq 99.9\%$), ytterbium (III) oxide (Yb₂O₃ $\geq 99.9\%$), and neodymium (III) oxide (Nd₂O₃ $\geq 99.9\%$), were purchased from Sigma-Aldrich. Aqueous solutions of lanthanide nitrate salts (Ln(NO₃)₃) were prepared by dissolving lanthanide oxide in hot concentrated nitric acid. The determination of the Ln (III) ion concentration was performed by complexometric titration with disodium ethylenediaminetetraacetic acid salt (EDTA analytic grade, synth) using xylenol orange (5 w% in KBr) as indicator and acetic / acetate (pH \approx 6) as buffer. The synthesis of the core-shell oxide was carried out in three steps by adapting the methodology described by Wang, et al⁸³ (Figure14). All the reagents were prepared in aqueous solution, it was used deionized water (≥ 18.2 M Ω cm) from a Milli-Q water purification system (Millipore).

2.2.1. Surfactant exchange

First, 5 mL of NaOL 0.03 mol L⁻¹ were mixed with 5 mL of CTAB-AuNRs 0.48 mmol L⁻¹ at 85 °C for 1h. Then, the solution was centrifuged at 8609 g for 25 min followed by the removal of the supernatant and redispersed in 10 mL. The obtained product was NaOL-AuNRs.

2.2.2. Formation of the core-shell structure

For the second step, 5 mL of NaOL-AuNRs solution were diluted in 223 mL of DI water, then were added 4 mL of HMT 0.1 mol L⁻¹ and 3.2 mL of Gd(NO₃)₃ 0.01 mol L⁻¹ containing 2% of Er(NO₃)₃ and 18% of Yb(NO₃)₃. The solution was stirred for 2 min and incubated for 4 h at 85 °C. Then were added 2 mL of HMT and 1.6 mL of Gd(NO₃)₃ 0.01 mol L⁻¹ containing 20% of Nd(NO₃)₃ over stirring for 2 min. The solution was kept at 85 °C and incubated for another 4h. Finally, it was left undisturbed overnight and centrifuged the next day at 8609 g for 25 min to remove the supernatant. The product was dried and stored in a desiccator to obtain the precursor AuNRs@Gd(OH)₃/Gd(OH)CO₃:Er(III), Yb(III)@Gd(OH)₃/Gd(OH)CO₃:Nd(III) · H₂O.

2.2.3. Thermal treatment

The obtained precursor was calcined at 800 °C in air atmosphere for 3 h and cooled with a N₂ flux in order to avoid the CO₂ absorption on the material surface. The final product was AuNRs@Gd₂O₃:Er(III),Yb(III)@Gd₂O₃:Nd(III) .

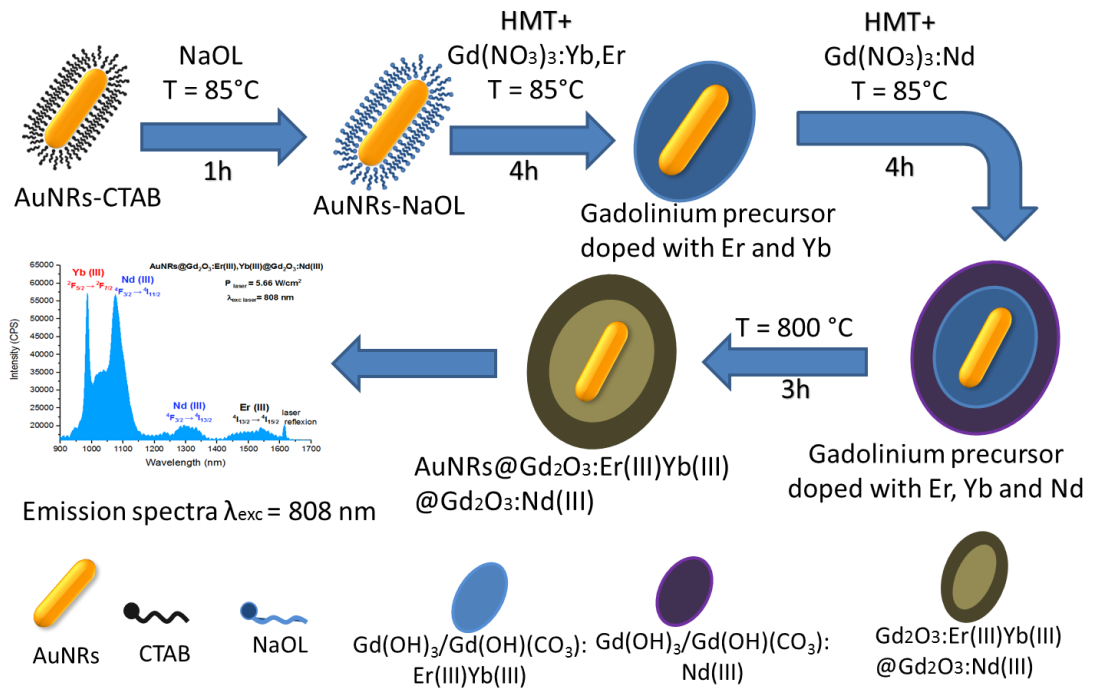


Figure 14. Schematic illustration of the formation process of the AuNRs@Gd₂O₃:Er(III),Yb(III)@Gd₂O₃:Nd(III) core-multishell nanoparticles.

2.3. Characterization

2.3.1. Ultraviolet-visible spectroscopy (UV-Vis)

All the synthesized samples were characterized in a UV-Vis Spectrophotometer Cary 50, using a quartz cuvette with path length of 1 cm. The samples were prepared by taking a 400 μL aliquot and mixing with deionized water with a dilution factor of [1:4]. The spectra were measured between 200-1100 nm.

2.3.2. Infrared spectroscopy

In order to verify the formation of the hydroxide/hydroxycarbonate precursor and the oxide formation after the thermal treatment. Products from the step 2 and 3 were characterized by IR spectroscopy in a FTIR spectrophotometer Agilent Cary 660 from 400 to 4000 cm^{-1} .

2.3.3. Transmission electron microscopy (TEM)

In order to study the morphology and size distribution of the NPs, all samples were characterized by TEM microscopy with an additional energy dispersive analysis (EDS) to verify the Ln ions distribution along the different shells. The measures were made in a Libra-Zeiss TEM with a work voltage of 120 KV with a tungsten filament. The samples were prepared by dropping aliquots of 3 μL of the washed solutions at the end of each step in a copper grid containing a carbon film (TedPella). After naturally drying, the grid was analyzed. Moreover, High resolution (HR) TEM images and Selected Area Electron Diffraction (SAED) measures were performed in order to confirm the crystalline structure of the oxide phase and determinate the interplanar distances and their correlation with the diffraction profile. EDS mapping and High-Angle Annular Dark-Field imaging were performed in a TEM-JEOL 2100 microscopy with a work voltage of 200kV.

2.3.4. Fluorescence spectroscopy

The emission spectra of the precursor and the final product were measured in powder on a spectrofluorometer Fluorog-3 (Horiba Jobin-Yvon FL3-22-iHR320) under two irradiation sources Crystalaser DL808-1W-T₀ and DL980-1W-T₀. The analysis in aqueous solution was not possible due to the low solubility of the samples in water and ethanol.

2.3.5. Thermogravimetric and differential thermal analysis

In order to establish the formation temperature of the oxide phase in the step 3. The Thermogravimetric (TG) and differential thermal (DT) curves of the samples were obtained on a TA SDT Q600 instrument, from 25 – 1000 °C in α -alumina crucible under synthetic air atmosphere with a heating rate of 5 °C ·min⁻¹.

2.3.6. X-Ray Diffraction analysis (XRD)

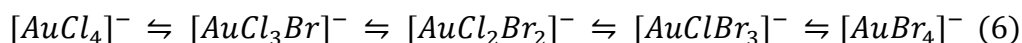
To further confirm the formation of the oxide formation and the crystalline phase. The X-Ray diffraction pattern was obtained in a Shimatzu XRD 7000 diffractometer using CuK α (1.5418 Å) radiation in the 10 to 70° 2 θ range with screening rate of 0.5° min⁻¹.

Chapter 3

Results and Discussion

3.1. Gold nanorods synthesis

According to the procedure previously described, the synthesis of the AuNRs was carried out through a seed preparation methodology. In order to obtain high quality rod-shape morphologies and control the aspect ratio, the role of every reagent is crucial. Then, there are some conditions that must be controlled. First in the seed preparation step, the NaBH₄ acts as a strong reducing agent that will reduce the Au(III) ions in the solution to Au(0), their addition must be as fast as possible to achieve the simultaneous production of all the nuclei (gold seeds) leading to a light-brown color that indicates the formation of small NPs (< 2 nm), conversely a pink-red coloration indicates the formation of bigger NPs. Otherwise, CTAB has a quaternary ammonium surfactant head group that forms a complex with the gold salt precursor and modifies its redox potential⁴ and is known to form rod-shape micelles, which are expected to induce the anisotropic growth of the spherical seeds. Additionally, it has a carbon tail long enough to stabilize the nanorods, but short enough to achieve solubility in water at room temperature, making CTAB the surfactant most common used in the synthesis of AuNPs. Along the synthesis procedure the gold precursor (HAuCl₄) involves three oxidation states: Au(III) in the precursor, Au(I) as intermediate, and Au(0) comprising the final NPs. According to the ligand field theory, the complexation strength of Au(III) with halides follows the series I⁻ < Br⁻ < Cl⁻. Therefore, in the presence of the CTAB, the four chloride ligands in AuCl₄⁻ will be eventually replaced by the bromide ions from the surfactant, which results in a color change from pale-yellow to dark orange-yellow according to the equilibrium in Eq (6).



In addition, the AuBr₄⁻ ions will form an ion pair with the quaternary ammonium surfactant monomers, which are neutral and insoluble in water, requiring a surfactant concentration ratio of [60:1] to ensure dissolution. This is very important since both, the AuCl₄⁻ - AuBr₄⁻ exchange and the formation of the AuBr₄⁻- CTA complex will influence the redox potential, in turn influencing the growth kinetics.

For the second step, H_2O_2 was used as the reducing agent under basic conditions. The objective of using a weaker reducing agent is to ensure that gold reduction only occurs on the existing nuclei in the solution, reducing Au(III) ions to Au(I). It is also important that H_2O_2 do not reduce Au(I) ions to Au(0), since this could lead to a secondary nucleation process along the growth step, reducing the proportion of NPs that are nanorods. Then, the seeds act as catalysts for the final reduction, inducing the reduction of the Au(I) to Au(0) only on the particle surface⁸⁴⁻⁸⁶. Finally, the solution pH was set to 11.5 to favor the final reduction above the seeds, and the amount of AgNO_3 was varied considering that higher concentrations of Ag^+ ions will increase the aspect ratio of the AuNRs, because this salt slows down the growth process above the seeds. Therefore, through the methodology described in the experimental section were synthesized AuNRs with a longitudinal LSPR band centered at ~ 790 nm (AuNRS-790) as shown in Figure 15. In order to modulate the longitudinal LSPR band to larger wavelengths, the amount of AgNO_3 was increased to 60 μL and the amount of H_2O_2 was increased to 56 μL to achieve a relation $\text{H}_2\text{O}_2/\text{Au(III)} = 28.14$. Since, according to Xu et al,⁸² the AuNRs aspect ratio increases as long as the $\text{H}_2\text{O}_2/\text{Au(III)}$ ratio increases. Then, under these conditions, there were synthesized AuNRs with a longitudinal LSPR band centered at ~ 931 nm (AuNRs-931) (Figure 16). Both Samples of AuNRs shows a LSPR band around ~ 530 nm corresponding to the transverse mode of the nanorods. However, Figure 16 shows a pronounced shoulder in the transverse LSPR band indicating the formation of AuNPs with other morphologies during the growth of the AuNRs-931. Moreover, a narrower and more symmetric longitudinal LSPR band is observed for AuNRs-790 (Figure 15) when compared to AuNRs-931 (Figure 16), which is associated with a more homogeneous size distribution for the first one. The UV-Vis spectra were measured before and after the washing step to guarantee the stability of the AuNRs under low concentrations of CTAB.

On the other hand, the reduction yield which corresponds to the total amount of gold precursor that was reduced along the synthesis procedure can be precisely estimated from the absorbance at 400 nm. This wavelength was selected because the main contribution of the absorbance comes from absorption related to interband transitions in metallic gold. Since particles with the same volume will equally contribute to the absorbance at this wavelength, regardless of the shape and size of the NPs. Therefore, the concentration of Au(0) in the final product was calculated from the normalized spectra (Figure 15b and 16b) at 400 nm, knowing that an absorbance of 1.2 correspond to $[\text{Au(0)}] = 0.5 \text{ mM}$ ⁸⁴.

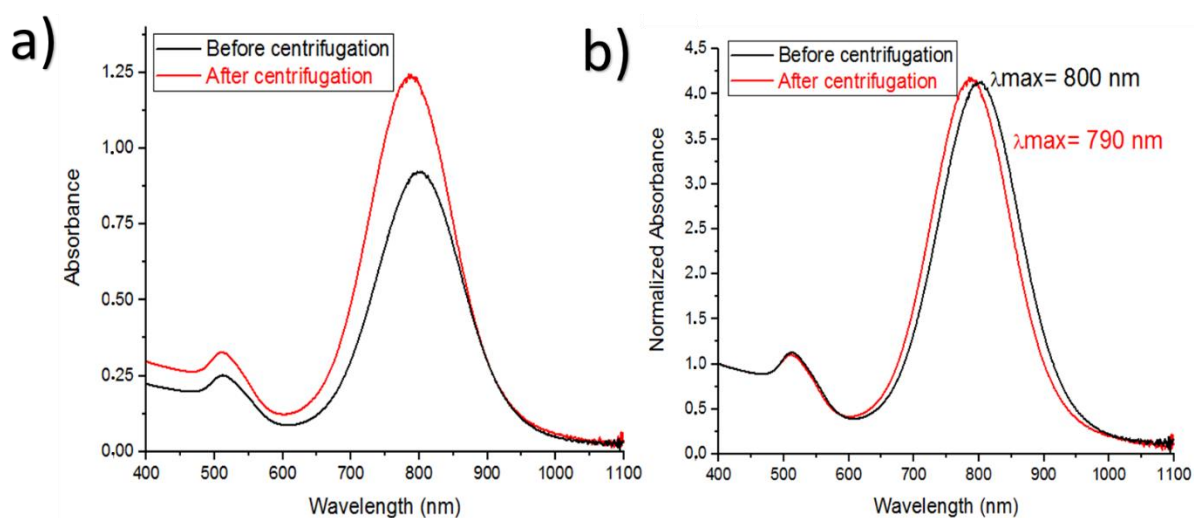


Figure 15. *a) AuNRs-790 UV-Vis spectra using 20 μL AgNO_3 and $\text{H}_2\text{O}_2/\text{Au (III)} = 13.82$. (---) Before centrifugation; (----) after centrifugation. **b) UV-Vis spectra normalized at 400nm.***

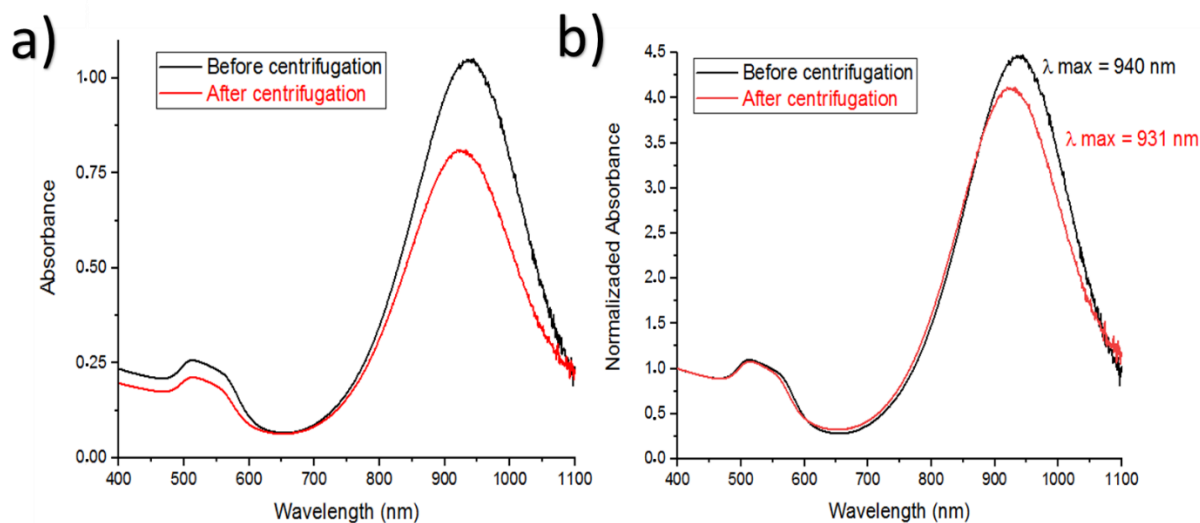


Figure 16. *a) AuNRs-931 UV-Vis spectra using 60 μL AgNO_3 and $\text{H}_2\text{O}_2/\text{Au(III)} = 28.14$ (----) before centrifugation; (----) after centrifugation. **b) UV-Vis spectra normalized at 400nm.***

The morphological features of the AuNRs were studied by TEM microscopy in order to corroborate the rod shape morphology and calculate the size distribution as shown in Figures 17 and 18. TEM images (Figure 17) shows that AuNRs-790 are homogenous with average width and length of 14.5 ± 1.2 and 55.8 ± 7.9 nm respectively. However, some nanospheres or nanocubes could be observed due probably to the speed of gold reduction with a strong reducing agent such as NaBH_4 at the initial stage. In the case of the AuNRs-931

(Figure 18), additionally to the spheres and cubes, the nanorods shows some bone shape morphologies with reduced width 12.8 ± 2.1 and increased length 63.3 ± 11.8 compared to the AuNRs-790. This may be associated with the effect of AgNO_3 on the growth speed of gold above the seeds in the second step, as reported by Scarabelli et al⁸⁴. In addition, Figure 19 shows the aspect ratio and size distribution of the AuNRs. As was expected, the LSPR band is dislocated to larger wavelengths with the increase of the aspect. This red-shifting in the longitudinal LSPR band of the AuNRs-931 compared to the AuNRs-790 may be attributed to the fact that AuNRs-931 has a bigger length which increases the charge separation along the longitudinal mode of the nanorods, decreasing the energy of the LSPR band. Table 2 shows the average width, length and aspect ratio of the Synthesized NPs.

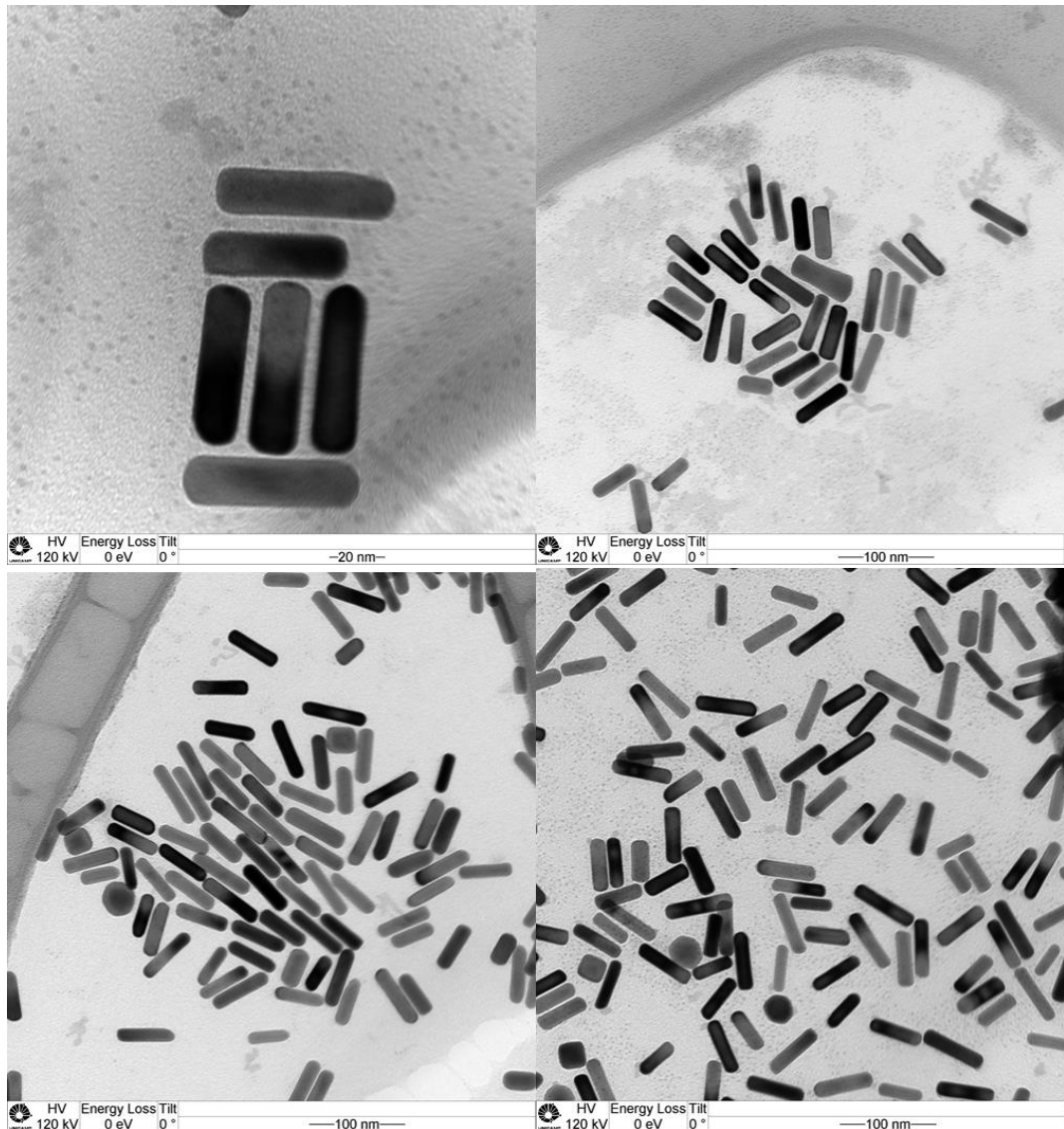


Figure 17. TEM images of the AuNRs-790 at different magnifications. 20 nm (top left), 100 nm (top right and bottom)

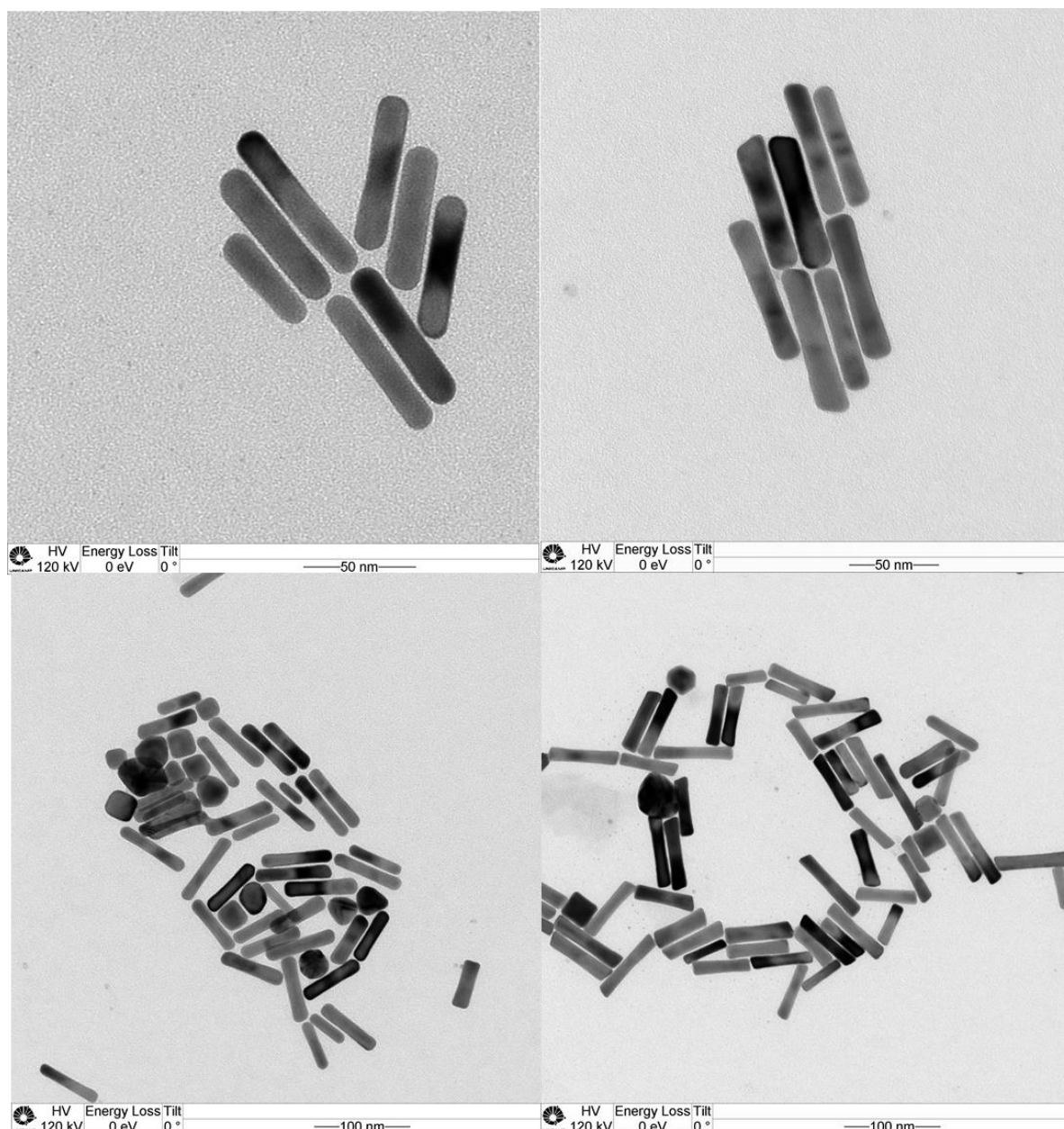


Figure 18. TEM images of the AuNRs-931 at different magnifications. 50 nm (top), 100 nm (bottom)

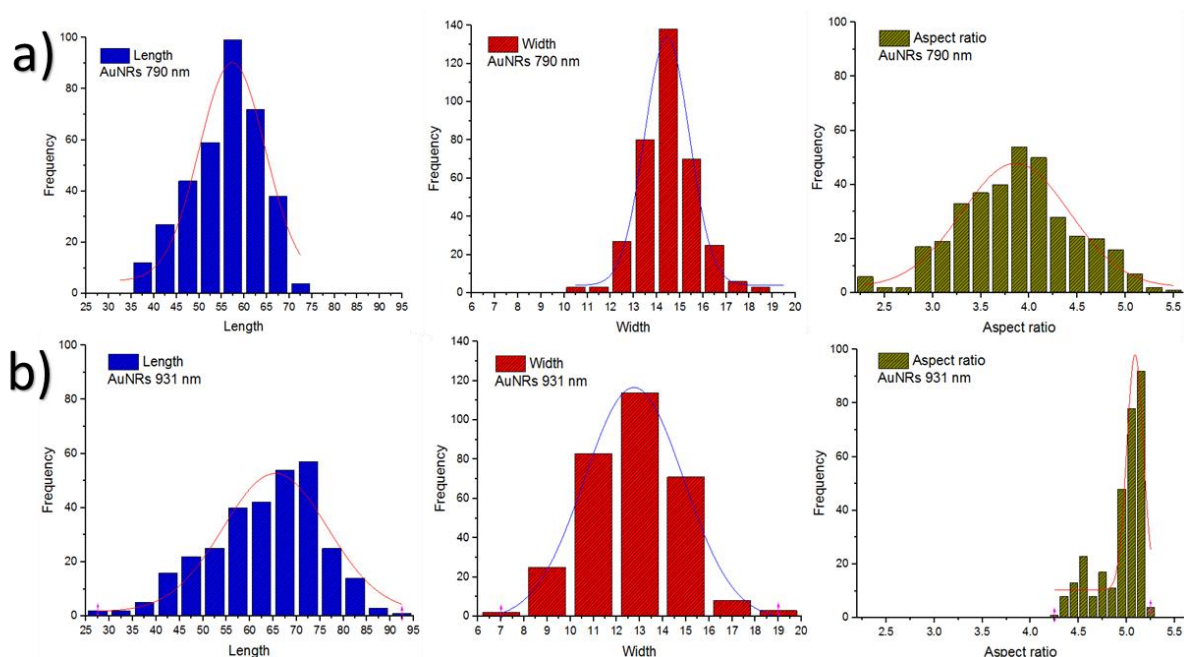


Figure 19. Size distribution and aspect ratio of. *a)* AuNRs-790 and *b)* AuNRs-931. Were counted 355 and 308 NPs respectively.

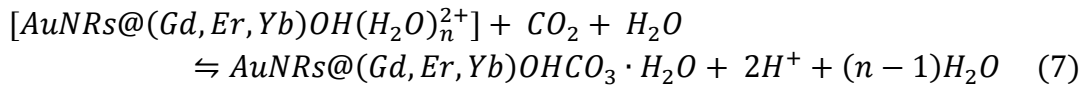
Table 2. Average sizes dimensions and aspect ratio of the synthesized AuNRs.

	AuNRs LSPR band centered at 790 nm	AuNRs LSPR band centered at 931 nm
Average Width (nm)	14.5 ± 1.2	12.8 ± 2.1
Average Length (nm)	55.8 ± 7.9	63.3 ± 11.8
Average Aspect Ratio	3.9 ± 0.6	4.9 ± 0.3

3.2. Synthesis of the AuNRs@Gd(OH)₃/GdOHCO₃:Er(III),Yb(III)·H₂O precursor.

The synthesis of the AuNRs@Gd(OH)₃/GdOHCO₃:Er(III),Yb(III)·H₂O core-shell NPs was carried out according to the method reported by Wang et al⁸³ using HMT and Gd(NO₃)₃ doped with Er (III) and Yb (III). First, the CTAB surfactant was exchanged for NaOL in order to obtain AuNRs-NaOL as described in the experimental section. Because the carboxylic groups in the NaOL has strong chemical chelation with the Ln ions due to the electrostatic forces; leading to the formation of a lanthanoid-oleate complex, which increase

the Ln ions concentration around the AuNRs surface instead of the free space. After the removal of the supernatant, the AuNRs-NaOL solution was diluted in water, followed by the addition of the HMT and the $\text{Ln}(\text{NO}_3)_3$. Then, by heating the reaction mixture at 85-90 °C the HMT is hydrolyzed releasing NH_3 , which further in aqueous solution release OH^- ions, that will interact with the Gd(III), Er(III) and ,Yb(III) ions, resulting in a hydroxide intermediate product of $(\text{Gd, Er, Yb})\text{OH}(\text{H}_2\text{O})_n^{2+}$ that reacts with the CO_2 dissolved in water. Leading to a mixture of $[(\text{Gd, Er, Yb})(\text{OH})_3 \cdot \text{H}_2\text{O}]$ and $[(\text{Gd, Er, Yb})\text{OHCO}_3 \cdot \text{H}_2\text{O}]$ according to Eq. (7). The amount of $[(\text{Gd, Er, Yb})\text{OHCO}_3 \cdot \text{H}_2\text{O}]$ in the mixture further increases after the removal of the supernatant and in the dried step, since $[(\text{Gd, Er, Yb})(\text{OH})_3]$ has a high affinity for CO_2 , forming more hydroxycarbonate.



On the other hand, the methodology described in the reference procedure and other papers consulted^{82,87} does not show clearly how was calculated the AuNRs concentration in the step previous to the core-shell formation, so several attempts were made in order to establish the optimal Au/Gd(NO₃)₃ ratio needed to obtain core-shell structures with a proper morphology. First, the amount of Gd(NO₃)₃ was more much bigger than the Au concentration [1:800] leading to the growth of the Gadolinium matrix above the AuNRs and in the free space as shown in the Figure 20a. Then, the Au/Gd(NO₃)₃ ratio was reduced to [1:1] leading to the formation of a shell of ~1 nm of thickness (Figure20b). Finally the optimal Au/GdNO₃ ratio was found to be [1:8.33] leading to the formation of the AuNRs@Gd(OH)₃/GdOHCO₃.Er(III),Yb(III)·H₂O precursor showed in Figure 21a. All the AuNRs were coated with the gadolinium matrix and also can be observed the growth of some hydroxide/hydroxycarbonate NPs without gold. The NPs achieved have a size and morphology very similar to the NPs reported in the references^{81,83,87,88} as shown in Figure 21 b and c.

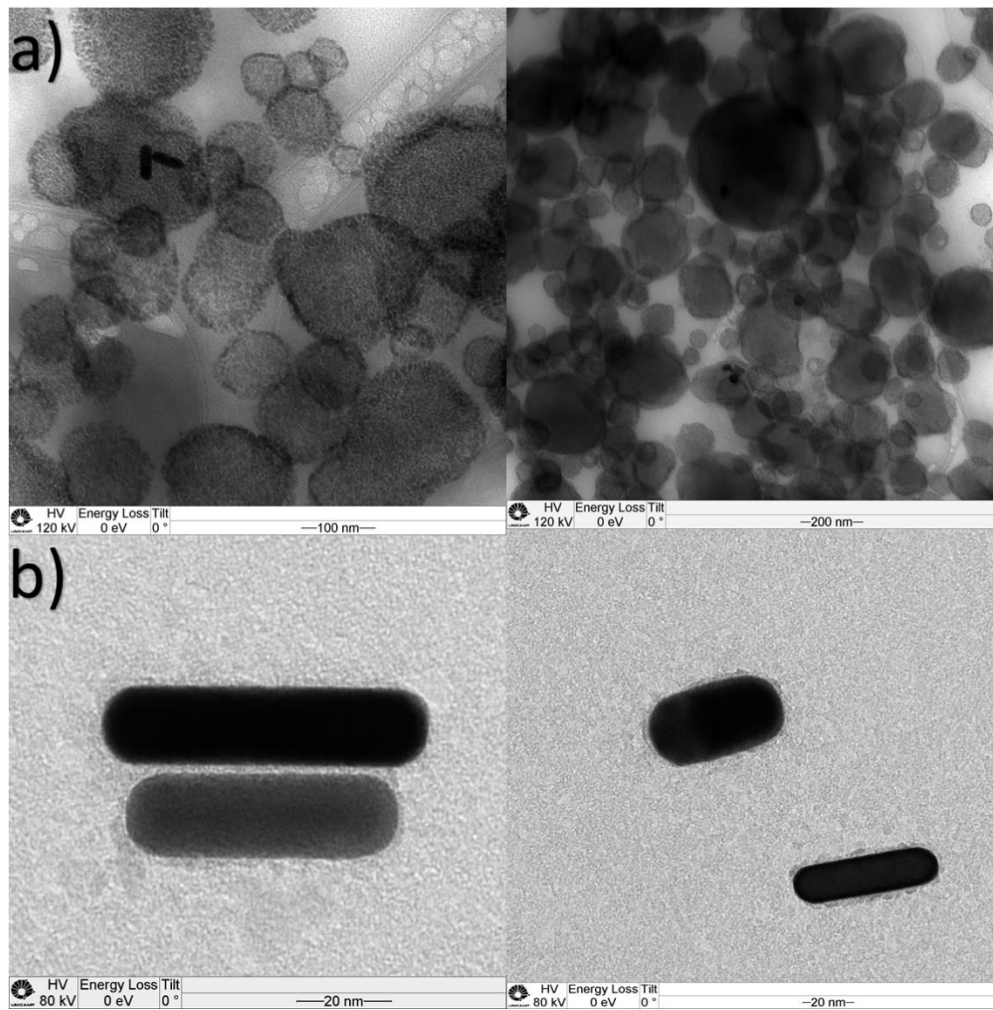


Figure 20. TEM images of the AuNRs@Gd(OH)₃/GdOHCO₃:Er(III), Yb(III)·H₂O at different magnifications with Au/Gd(NO₃)₃ ratio of a) 1:800 and b) 1:1.

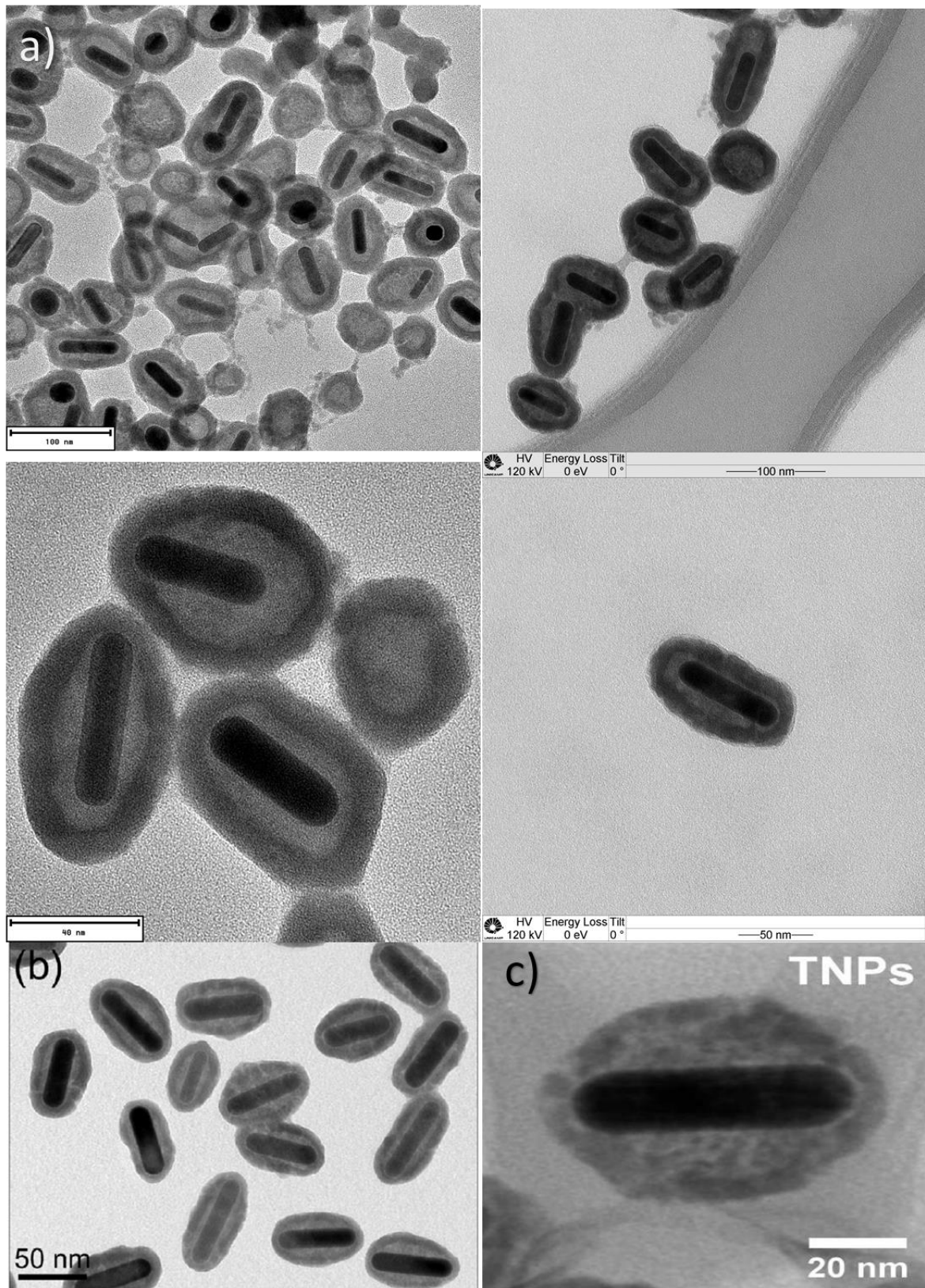


Figure 21. TEM images of AuNRs@Gd(OH)₃/GdOHCO₃:Er(III), Yb(III)·H₂O precursor at different magnifications *a)* From this work *b)* Reproduced from ref 83. *c)* Reproduced from ref 81.

The amount of Er(III) and Yb(III) ions in the shell was calculated to be 2 and 18% respectively because this is the optimal concentration of the dopants in order to avoid concentration quenching effects and observe an enhancement of the emission intensity due to the different energy transfer processes between the Ln ions⁵⁴. In addition, Gadolinium oxide was selected as the host matrix because it has low lattice phonon energy and since Gd(III) ions have been widely used as contrast agent for magneto resonance imaging and can also restrict the temperature-sensitive shape deformation of AuNRs, allowing image-guided PTT for the treatment of cancer cells⁶⁸. Moreover, to confirm the presence of Yb(III), Er(III) and Gd(III) ions was realized an electron energy loss spectroscopy (EELS) mapping (Figure 22), showing homogeneous distribution of the Ln ions along the NP completely coating the AuNRs surface. The contrast for Er(III) ions it's difficult to observe due to its low concentration (2%) compared with the other Ln ions. Therefore, their signal cannot be detected since it is on the same scale of the equipment background.

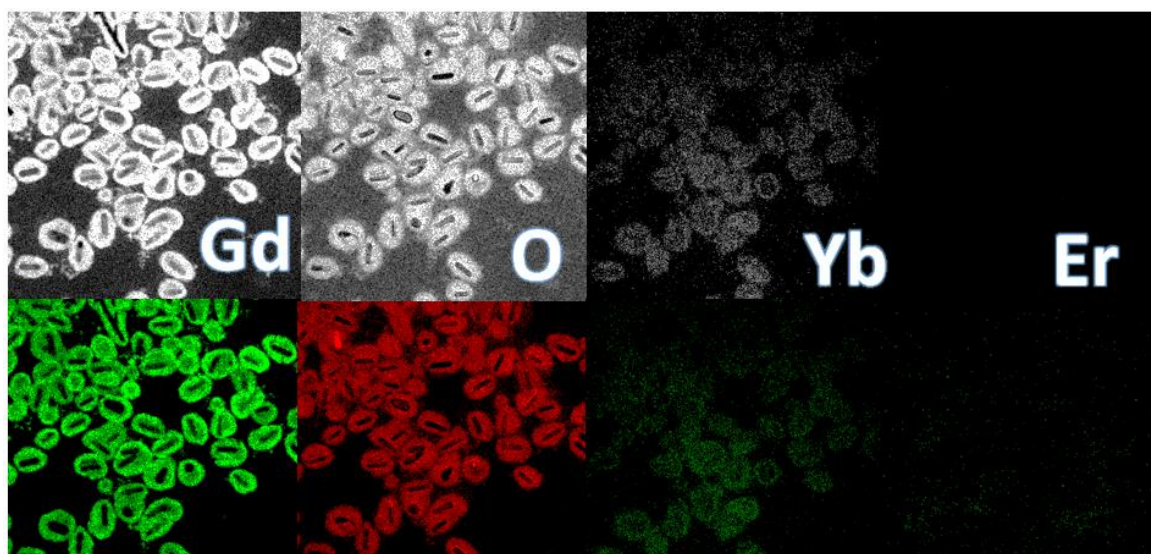


Figure 22. EELS mapping of the AuNRs@Gd(OH)₃/GdOHCO₃:Er(III),Yb(III)·H₂O core-shell NPs.

3.3. Growth of the second shell of Gd(OH)₃/GdOHCO₃:Nd(III).

In order to grow a second shell of the gadolinium matrix over the previous system, was added Gd(NO₃)₃ doped with 20% of Nd (III) with an Au/Gd(NO₃)₃ ratio of [1:4.16] in the presence of HMT. In this case, the particles in solution act as a nucleation center allowing the growth of the second shell on the surface of the precursor NPs, following a similar process as described in Eq. (7). TEM images in Figure 23a confirm the growth of the second shell; besides, along the synthesis procedure possibly there is an agglomeration process, leading to core-multishell NPs with several AuNRs in the core. In addition, in order to confirm the presence and desired distribution of the Ln ions along the different shells, was realized an EDS mapping (Figure 23b). The results confirm the successful formation of the core-multishell structure and homogenous distribution of the different Ln ions along the shells.

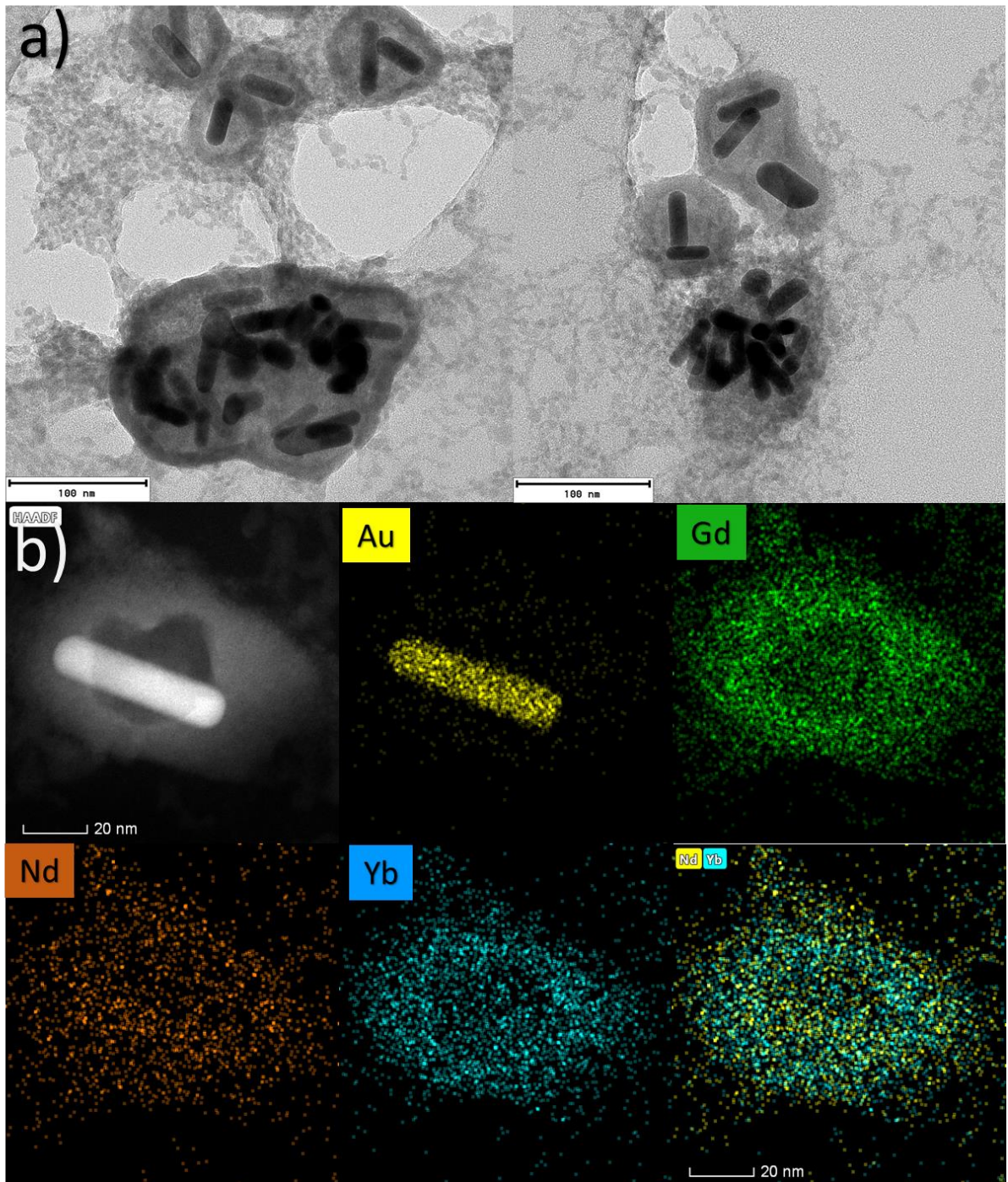


Figure 23. a) Transmission electron micrograph and b) EDS mapping of the core-multishell system.

3.4. Synthesis of AuNRs@Gd₂O₃:Er(III),Yb(III)@Gd₂O₃:Nd(III).

Finally, the core-multishell NPs were subjected to a thermal treatment in order to generate the oxide matrix since, as reported in the literature⁸⁷⁻⁸⁹, hydroxycarbonates and hydroxides are matrices with high lattice phonon energy modes that suppress the emission of the Ln ions; while gadolinium oxide is a better choice as mentioned above. Therefore, to establish the Gd₂O₃ formation temperature, thermogravimetric and differential thermal analyses were carried out. Figure 24 illustrate the thermal decomposition of the AuNRs@Gd(OH)₃/GdOHCO₃:Er(III),Yb(III)@Gd(OH)₃/GdOHCO₃:Nd(III)·H₂O NPs from 25-1000 °C with a heating rate of 5 °C min⁻¹ under synthetic air atmosphere. According to D'Assunção and Kim et al,^{90,91} the thermal decomposition of Ln(OH)₃ and LnOHCO₃ follows four steps as described in Equations (8-14). In general, all rare earth hydroxycarbonates will follow a sequence of dehydration, partial decarbonation, and full decarbonation. In addition, according to Boopathi et al,⁹² lanthanoids can lose up to 23% of their initial mass due to dehydration. Dehydration regarding evaporation of moisture mainly occurs below 100 °C with any additional water, or crystalline water in the hydroxycarbonate, being lost between 200 and 500 °C. Thus, after the dehydration process, hydroxycarbonates will partially decompose into oxycarbonates, which further decompose into the respective oxide. As can be observed from the TG curves, the total mass loss related to the decomposition process is about 44.34 %. Theoretical calculations predict a mass loss about 19.18% assuming a mixture ratio [50:50] of the hydroxide/hydroxycarbonate matrix and an Au/Gd₂O₃ ratio [0.05:1]. Since some other analyses as X-ray diffraction of the precursor sample are needed in order to establish more accurate relations about the amount of each phase. Besides, the composition of the final product is expected to be Au_{0.05}@Gd_{2-x}O₃:Yb_{0.18x}Er_{0.02x}@Gd_{2-x}O₃:Nd_{0.2x}. Considering this, there is a mass loss difference of 25.16% of which 7.86 % would be associated with the evaporation of moisture and partial dehydration of the water content in the sample observed in temperature range from 25-267 °C. The remaining 17.3 % would be related to the dehydration process regarding crystallization water and the decomposition of organic impurities from the synthesis procedure. Moreover, DTA curve shows a strong endothermic peak at 310°C associated to the transformation of the Gd(OH)₃ phase to

GdOOH. Additionally, HR-TEM images, IR and x-ray analyses confirm the successful formation of the Gd_2O_3 phase as discussed in the following sections.

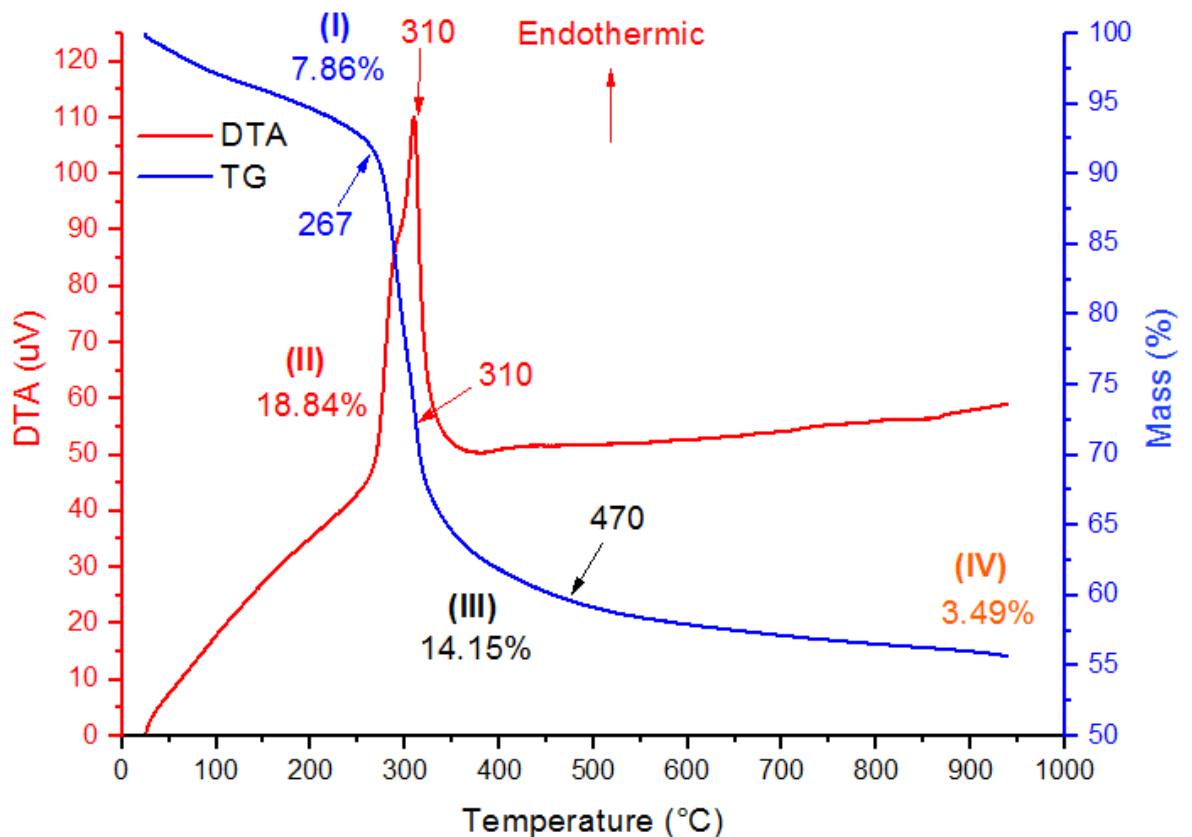
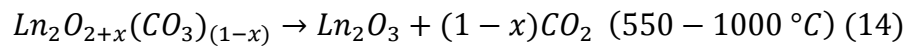
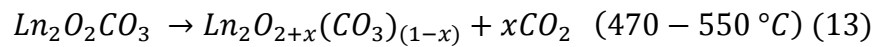
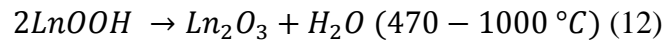
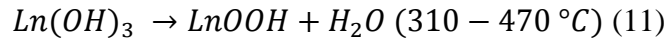
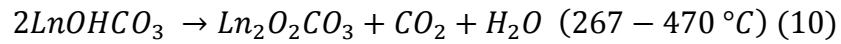
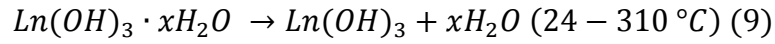


Figure 24. TG and DTA curves of the AuNRs@Gd(OH)₃/GdOHCO₃:Er(III), Yb(III)@Gd(OH)₃/GdOHCO₃:Nd(III)·H₂O.

As shown above, the oxide formation starts at temperatures between 470-550°C. Thereby, the thermal treatment was carried out under different conditions by varying the heat temperature and calcination time. The IR spectra were measured before and after the thermal treatment in order to verify the formation of the hydroxycarbonate and hydroxide phases in the precursor, and the oxide formation in the final product as shown in Figure 25. The precursor sample (Figure 25d) shows an intense broad band between 3000-3600 cm^{-1} corresponding to the stretching of the hydroxyl groups, characteristic of the hydroxycarbonate and hydroxide structures and surface-adsorbed water molecules. Additionally, at 1641 cm^{-1} there is a tiny shoulder corresponding to the bending mode of the water molecules present in the sample. The peaks at 2921 and 2852 cm^{-1} are associated with the symmetric and asymmetric stretching vibrations of CH_2 groups of the oleate surfactant. Moreover, the peaks at 1009, 845 and 721 cm^{-1} are associated with the ν_1 , ν_2 and ν_4 modes of the $(\text{CO}_3)^{2-}$ ions, while the intense peaks at 1494 and 1388 cm^{-1} correspond to the asymmetric stretching of the ν_3 modes of the carbonate ions. Also, at 683 cm^{-1} it is observed a peak originated from the OH bending of Gd-OH^{93} . Likewise, all the samples show two tiny peaks at 2360 and 2335 cm^{-1} corresponding to the absorption of atmospheric CO_2 . In addition the peaks at 1494 and 1388 cm^{-1} in the spectra a, b and c are symmetric and has the same intensity, while the peak at 1388 cm^{-1} in spectra d is more intense, this difference can be associated with the overlapping with the peak related to the stretching of the NO_3^- ions at 1370-1390 cm^{-1} showing that in the precursor sample there are some impurities from the synthesis procedure. These results confirm the formation of the $\text{Gd}(\text{OH})_3$ and GdOHCO_3 phases in the precursor. Otherwise, the thermal treatment of the samples in Figure 25 b and c were carried out at 600 °C during 0.5 and 2 h respectively. IR spectra show the absence of the peaks at 2951, 2852 and 683 cm^{-1} associated with the elimination of the organic impurities and the elimination of the Gd-OH interaction. Moreover, there is a large decrease in the band centered at 3355 cm^{-1} associated with the elimination of moisture and part of the hydroxyl groups in the precursor. The intensity of the peaks at 1494, 1388 and 845 cm^{-1} also decreases, indicating the elimination of carbonate in the gadolinium matrix. Although, possibly due to the calcination time, there is still a small fraction of the hydroxycarbonate phase present in the final product. Besides, at 538 cm^{-1} could be observed the formation of a tiny peak associated with the Gd-O stretching, indicating the formation of the Gd_2O_3 phase. Therefore, in order to achieve the total elimination of the hydroxycarbonate phase, a third attempt was performed at 800°C for 3h.

Figure 25a shows an even greater decrease in the bands corresponding to the carbonate and hydroxyl groups. In turn, the peak at 538 cm^{-1} became sharper and more intense, probably due to increased crystallinity of the sample. The corresponding results coincide to those reported by Gaspar et al⁹⁴, as shown in Figure 26, confirming the successful formation of the AuNRs@Gd₂O₃:Er(III), Yb(III)@Gd₂O₃:Nd(III).

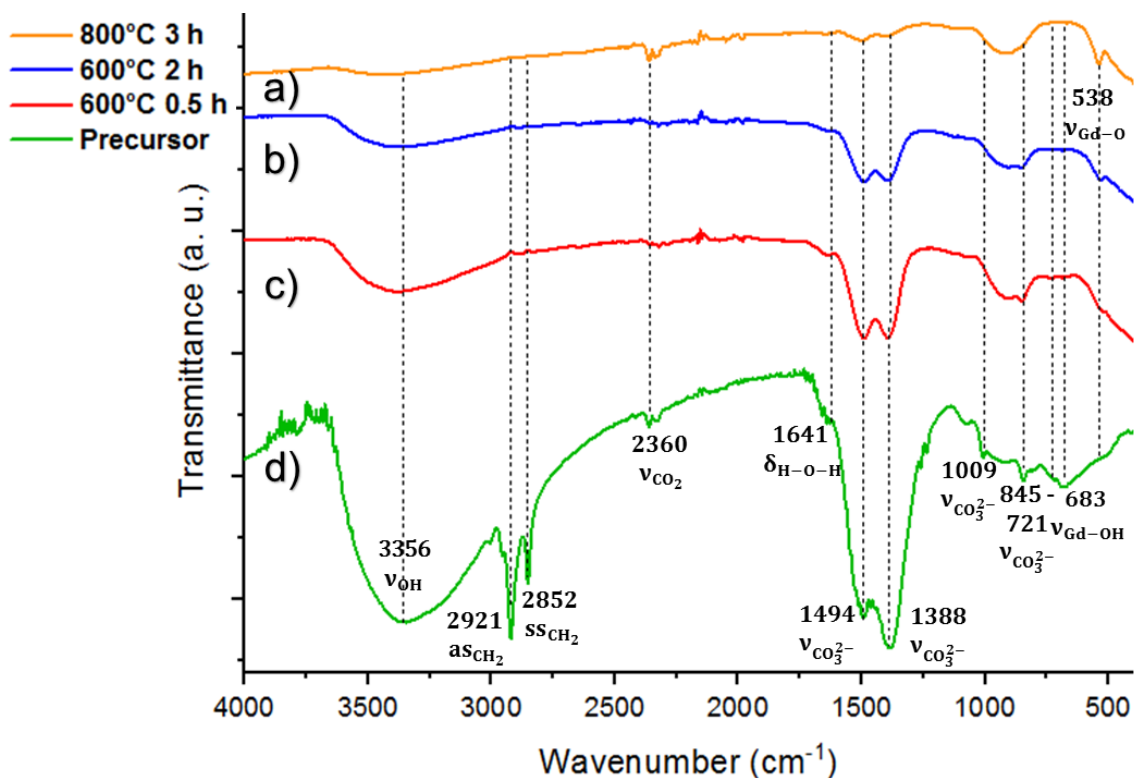


Figure 25. IR spectra of the samples: after thermal treatment under different conditions a) $800\text{ }^{\circ}\text{C}$ 3h b) $600\text{ }^{\circ}\text{C}$ 2h c) $600\text{ }^{\circ}\text{C}$ 0.5h. And d) before thermal treatment.

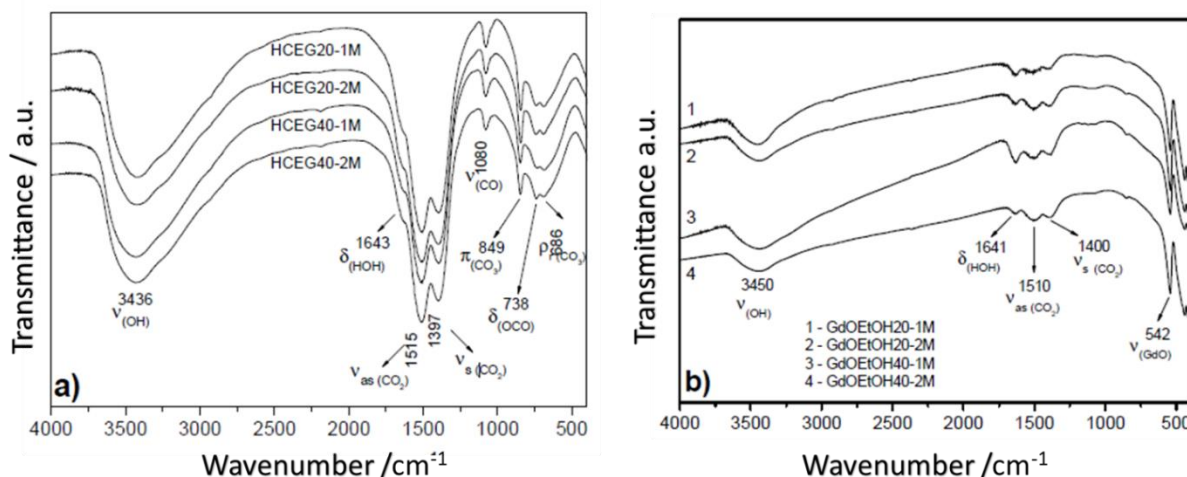


Figure 26. IR spectra of **a)** hydroxycarbonate and **b)** gadolinium oxide. Reproduced from ref.9. Copyright 2010 University of Campinas.

Moreover, in order to study the effect of the temperature on the morphology of the NPs after the thermal treatment, TEM measurements and EDS mapping were carried out (Figure 27a). TEM images show a deformation of the rod-shape morphology of gold, leading to a spherical structure. This is probably associated with an increase of the atomic mobility at high temperatures adopting a spherical morphology since it has lower surface energy. Another factor that could influence is the decomposition of the NaOL surfactant which stabilizes the AuNRs and maintains their rod-shape morphology. Otherwise, gold has a melting point of 1064 °C; decreases in melting temperature due to quantum effects at nanometric scale are observed for particles smaller than 6 nm⁹⁵, which is not the case since AuNRs used along the synthesis procedure have dimensions bigger than 12 nm. Likewise, EDS mapping of the NPs shows that the core-shell structure was maintained with the Gd, Yb, Er and Nd (III) ions distributed around the AuNPs core. HR-TEM image of an individual nanocrystal (Figure 27b) reveals the clear lattice planes, confirming the crystallinity of the as-prepared sample. The corresponding SAED patterns (Figure 27c) taken from a single NP can reveal the crystalline nature of the samples, showing lattice fringes with interplanar spacing of 0.313, 0.206, 0.235, 0.171 nm and 0.468 nm that corresponds to the planes (222), (431), (332), (622) and (211) of the cubic phase of the Gd₂O₃. These results are in well agreement with the XRD patterns shown in Figure 28. The crystalline phase was indexed as cubic Gd₂O₃ PDF number: 86-2477 space group: Ia-3; a= 10.81. In addition, was possible to identify the principal planes of cubic gold corresponding to the PDF: 4-784, space group: Fm-3m; a= 4.078. Besides, there is a

broad band between 17 and 27° associated with the use of a quartz sample holder along the analysis.

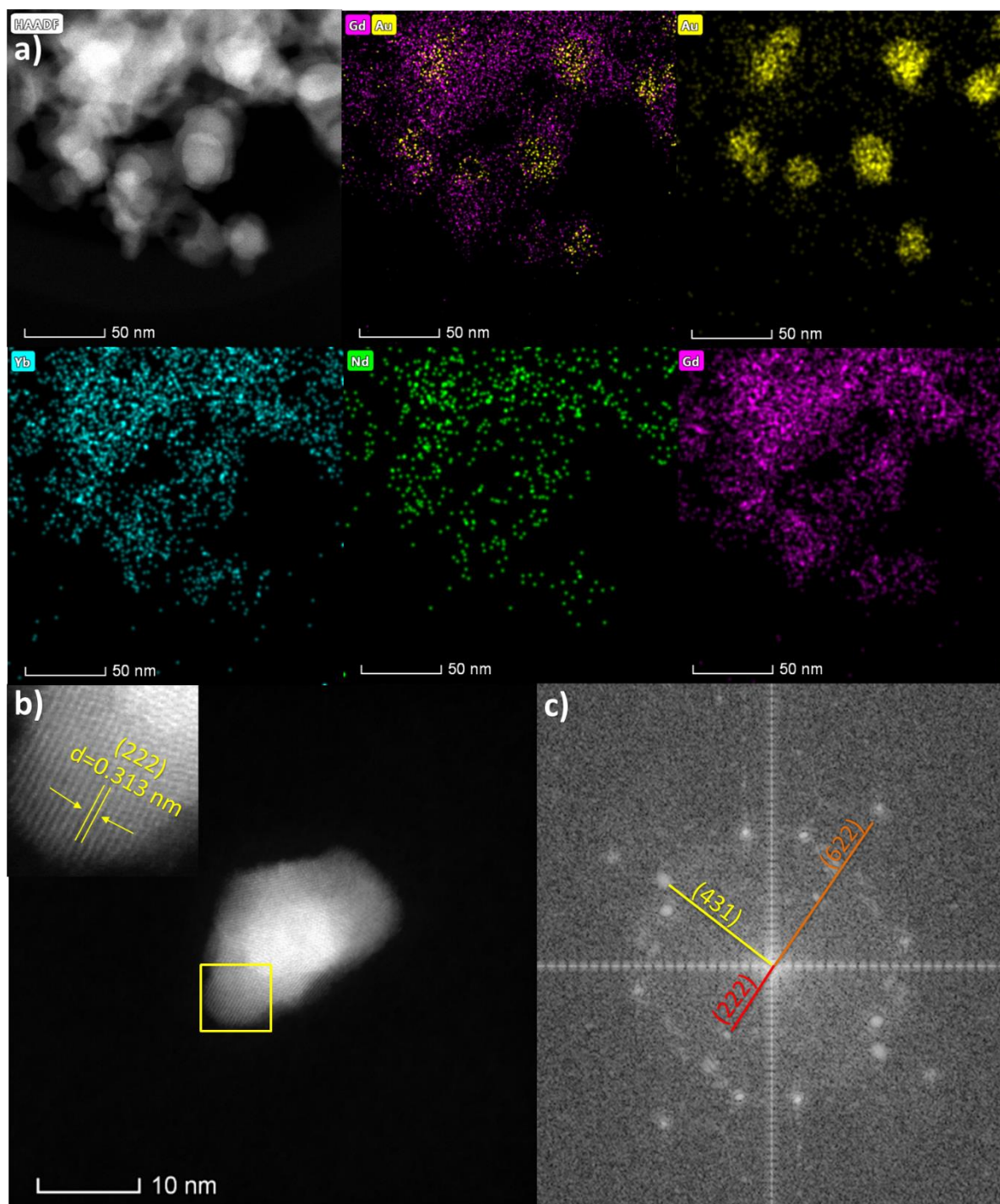


Figure 27. *a)* TEM image and EDS mapping, *b)* single crystal HR-TEM image and *c)* SAED pattern of AuNRs@Gd₂O₃:Er(III), Yb(III)@Gd₂O₃:Nd(III) after thermal treatment at 800 °C for 3h.

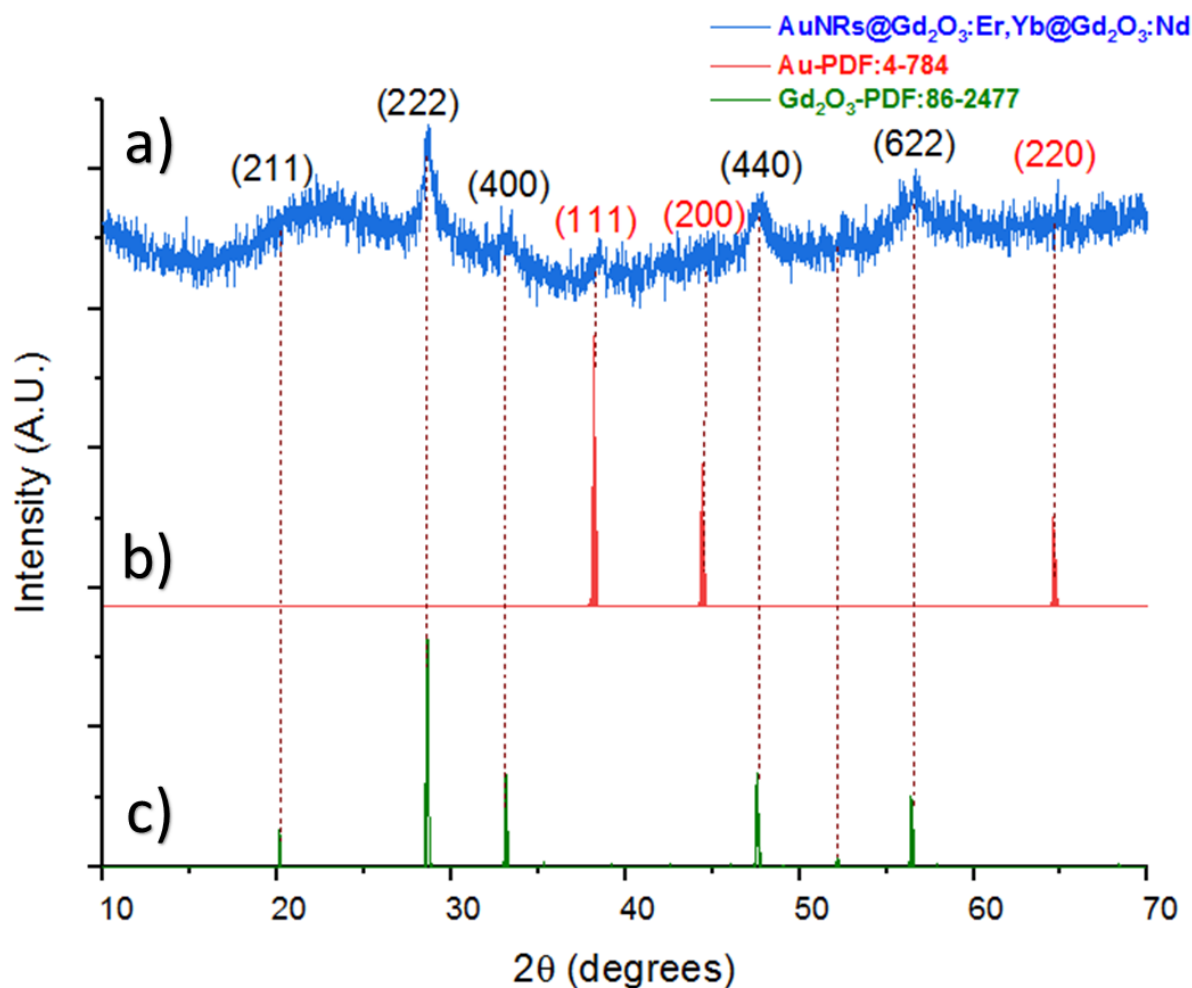


Figure 28. XRD patterns of **a)** AuNRs@Gd₂O₃:Er(III),Yb(III)@Gd₂O₃:Nd(III) after thermal treatment at 800 °C for 3h. **b)** AuNPs PDF: 4-784 and **c)** Gd₂O₃ PDF: 862477.

3.5. Fluorescence and optical thermometry.

The emission spectra under two different excitation wavelengths were measured in order to study the energy transfer processes between the Ln ions in the NIR region. First, was performed the measure of the emission spectra of the precursor sample, as was expected due to the presence of –OH and –CO vibrational groups, the emission is quenched and is not possible to observe any peak associated with the emission of the Ln ions. Then, were measured the emission spectra of the sample after the thermal treatment under laser irradiation of 808 (Figure 29) and 980 nm (Figure 30). Figure 29 shows four peaks, which could be associated with the transitions $^4F_{3/2} \rightarrow ^4I_{11/2}$ (1076 nm) and $^4F_{3/2} \rightarrow ^4F_{13/2}$ (1300 nm) that corresponds to the direct excitation of Nd(III) ions. In addition, is possible to observe the transitions $^2F_{5/2} \rightarrow ^2F_{7/2}$ (987 nm) and $^4I_{13/2} \rightarrow ^4I_{15/2}$ (1540 nm) that corresponds to the DS

energy transfer from Nd(III) to Yb(III) and Yb(III) to Er(III) respectively as is illustrated in Figure 31a. Moreover, Figure 30 shows two peaks, which may be associated with the direct excitation of Yb(III) ions $^2F_{5/2} \rightarrow ^2F_{7/2}$ (1059 nm) and the DS energy transfer from Yb(III) to Er(III) $^4I_{13/2} \rightarrow ^4I_{15/2}$ (1540 nm) as illustrated in Figure 31b. It is also observed a weak broad band at 1300 nm probably associated to the direct excitation of Nd(III). Therefore, additional to the IR spectra, XRD and SAED patterns, these results corroborate the formation of the oxide phase since hydroxycarbonate and hydroxides are non-fluorescence matrices, and after the thermal treatment was possible to observe the emission of the sample in the NIR region.

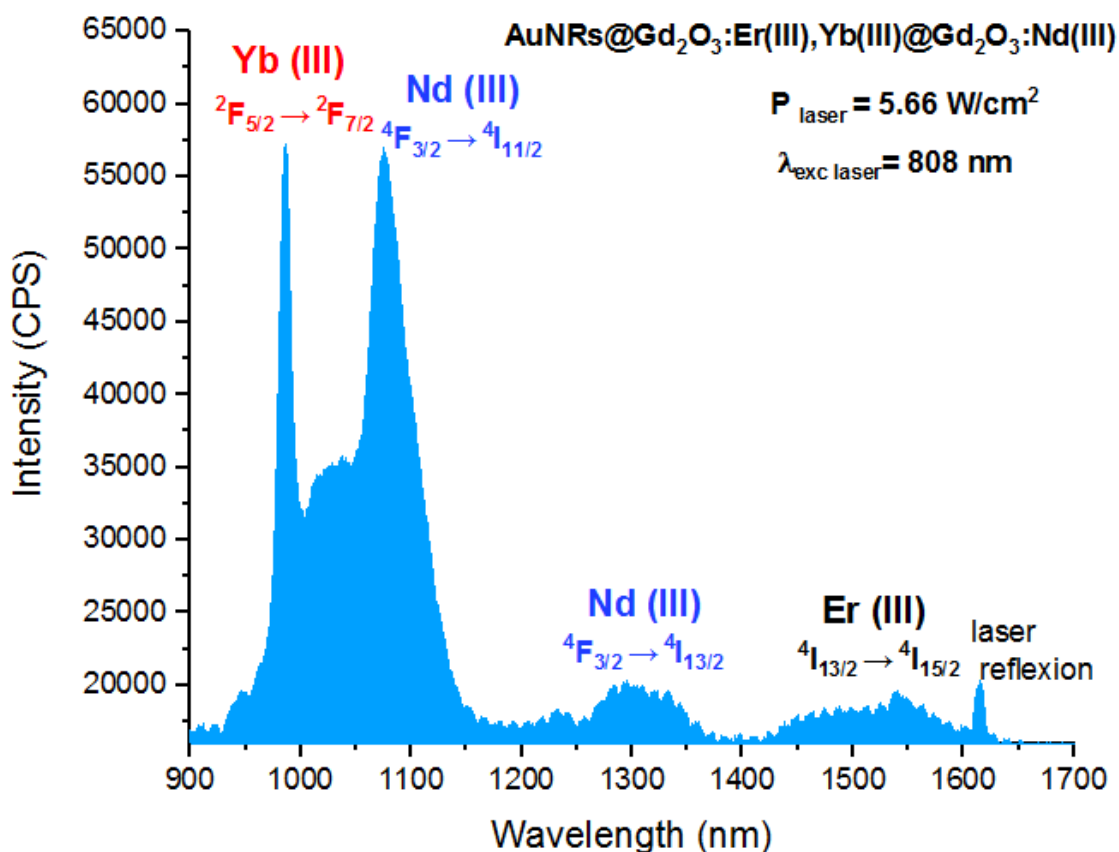


Figure 29. Emission spectra of the AuNRs@Gd₂O₃:Er(III),Yb(III)@Gd₂O₃:Nd(III) under 808 nm laser irradiation.

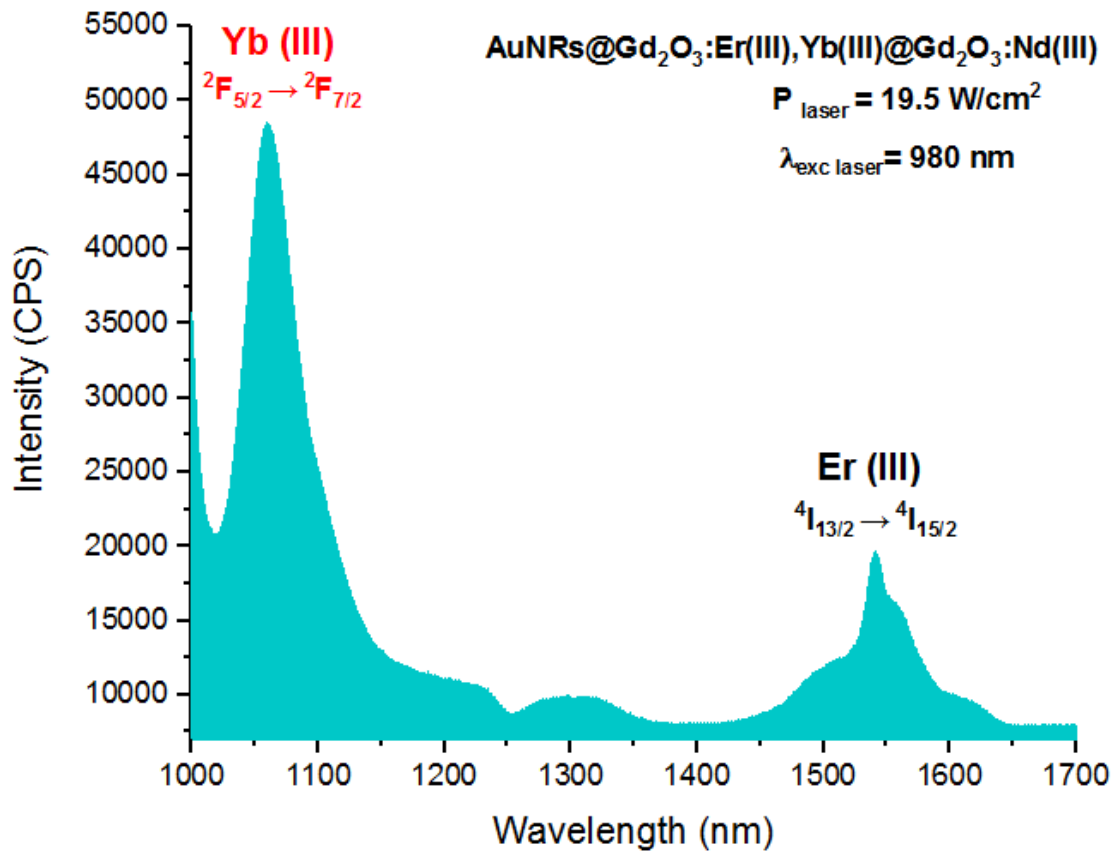


Figure 30. Emission spectra of the AuNRs@Gd₂O₃:Er(III), Yb(III)@Gd₂O₃:Nd(III) under 980 nm laser irradiation.

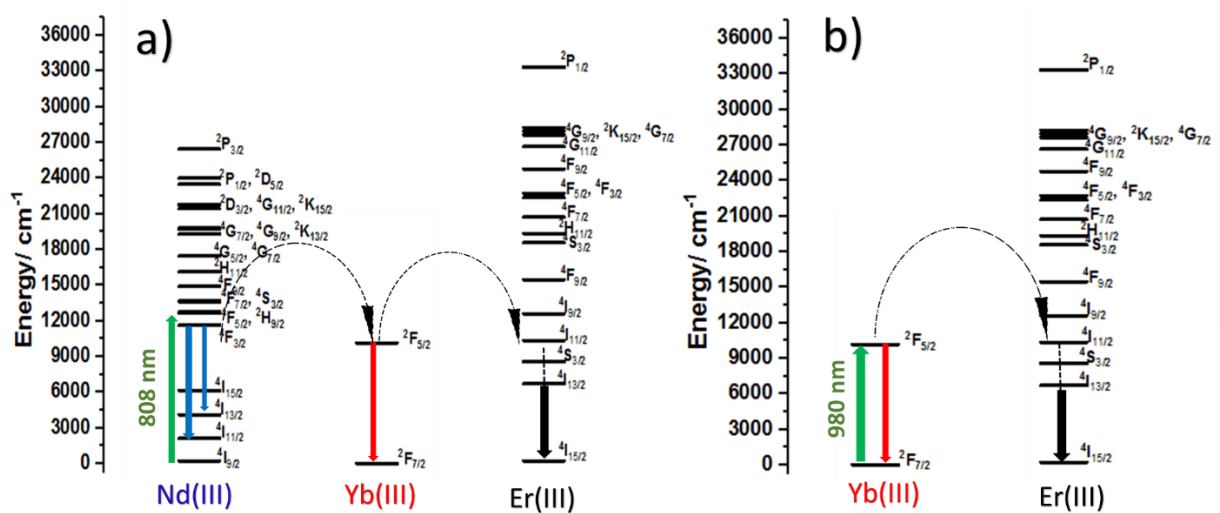


Figure 31. Proposed energy mechanisms for the emission of AuNRs@Gd₂O₃:Er(III), Yb(III)@Gd₂O₃:Nd(III) a) $\lambda_{exc} = 980$ nm b) $\lambda_{exc} = 808$ nm.

On the other hand, luminescent thermometers could measure the temperature in three main ways: i) spectral shift of a given transition, ii) emission intensity measurements, using the integrated intensity of a single transition or a pair of transitions; and iii) lifetime measurements, using the decay profiles of the emitting excited states⁹⁶. However, many luminescent studies^{17,46,97} report temperature dependent lifetime measurements and as was discussed in the literature review plasmonic materials could modify the lifetime of the Ln ions emitter levels. Thereby, the most common way to ascertain the absolute temperature is by measuring the intensities of two transitions of distinct emitting centers. Therefore, in this work there were measured the emission intensities of the transitions ${}^2F_{5/2} \rightarrow {}^2F_{7/2}$ and ${}^4I_{13/2} \rightarrow {}^4I_{15/2}$ of Yb(III) and Er(III) ions, respectively, under 980 nm laser irradiation. Since, the aim of this research is to take advantage of the hyperthermia phenomenon for PTT applications, generated by the heating of the AuNRs through the excitation of the LSPR band. Thus, as reported by Hemmer et al¹⁷, NIR region comprises several biological windows where tissue penetration is greater and minimizes phototoxic effects to the cells, additional to lower heating of the water molecules present in the tissue when NIR irradiation is applied instead of UV-vis. Moreover, most of the biomedical applications focused on detection and imaging of cancer cells use laser of 808 nm as the irradiation source, although by selecting the excitation wavelength at 980 nm could be achieved deeper tissue penetration and improved heating of the tissue without harm the surroundings by the heating of the water molecules, which in turn, combined with the hyperthermia due to the excitation of the LSPR band of the AuNRs in the core-shell NPs at this wavelength could lead to enhanced photothermal effect and improved theranostic activity. Therefore, towards evaluate the potential capacity of the AuNRs@Gd₂O₃:Er(III), Yb(III)@Gd₂O₃:Nd(III) system as an optical thermometer in the NIR region, were measured the emission spectra by varying the temperature from 30 to 51 °C in order to simulate the biological range. The emission spectra were measured by triplicate every 3 °C controlling the temperature with a Linkam thermostat under N₂ flux. Likewise, the operating range of a racimetric thermometer is determined by the linear region of the ratio between the intensities, LIR (luminescence intensity ratio). The rate at which the emission ratio changes with temperature provides the sensitivity of the thermometer⁹⁶ (Eq. (15)).

$$S = \frac{1}{LIR} \frac{dLIR}{dT} \quad (15)$$

Figure 32 shows the LIR ratio for the AuNRs@Gd₂O₃:Er(III),Yb(III)@Gd₂O₃:Nd(III) NPs. As could be observed, the LIR ratio is almost constant, showing any significant variation between the two transitions studied. In addition, Figure 33 presents the staked spectra at each temperature, showing that the emission intensity does not show significant variations as the temperature increases. Therefore, in this range of temperature, the sensitivity of the proposed system is very low, probably associated with the fact that the excited states of Er(III) ions could be thermal populated, thus in this narrow temperature range the thermal energy is not enough to populate the excited states, which may increase the emission intensity of this transition (1540 nm).

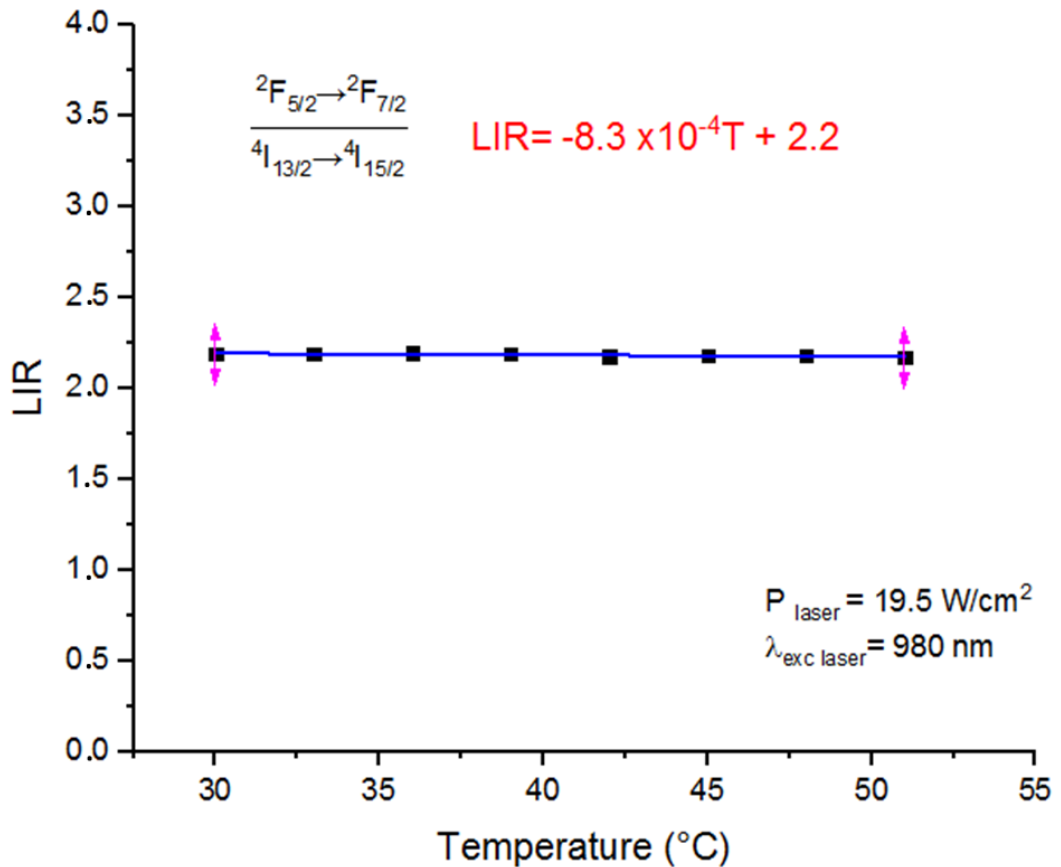


Figure 32. Linear Intensity Ratio (LIR) as a function of temperature under 980 nm laser irradiation.

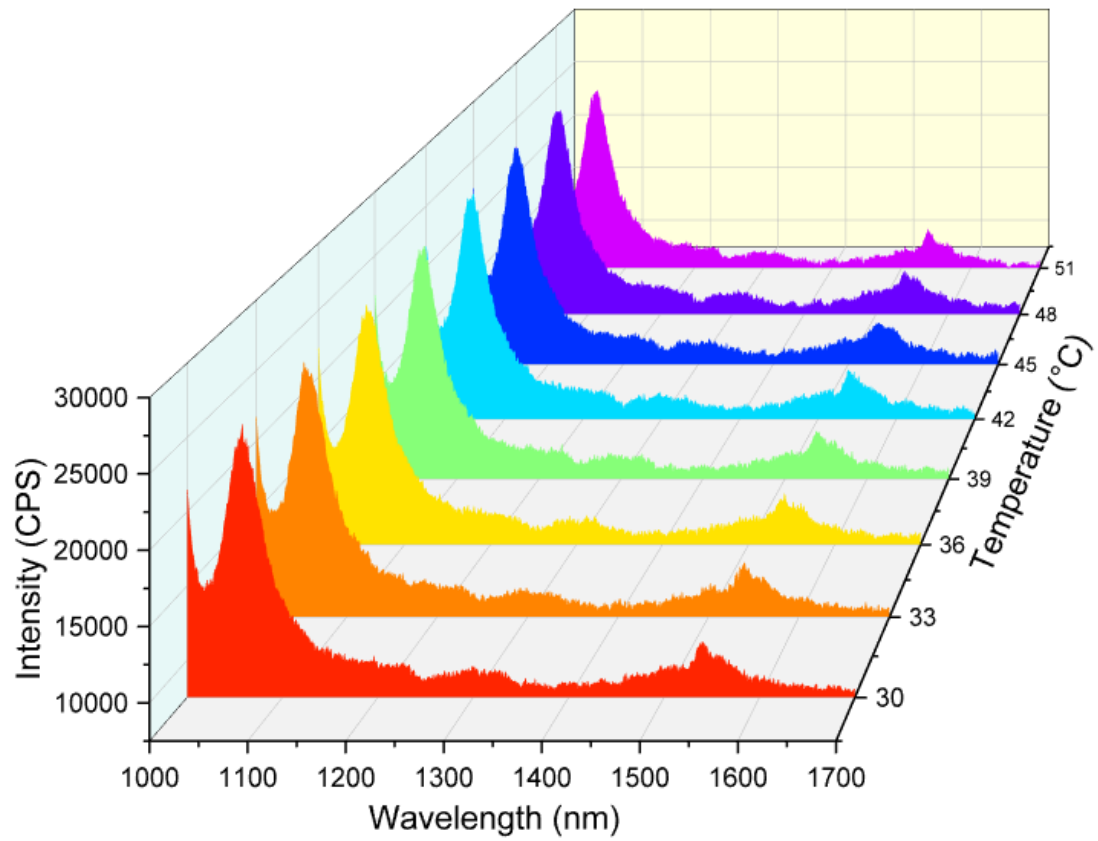


Figure 33. Stacked emission spectra of AuNRs@Gd₂O₃:Er(III),Yb(III)@Gd₂O₃:Nd(III) by varying the temperature from 30-51 °C under 980 nm laser irradiation.

3.6. Plasmon effect on the emission intensity

As discussed in the literature review, plasmonic NPs as AuNRs could enhance or quench the emission intensity of the Ln ions depending on the distance and the matching between the LSPR band maximum of gold and the excitation or emission bands of the Ln ions by modifying the rate of the radiative and non-radiative decays. Then, in order to study the effect of the coating on the position of the LSPR band of the AuNRs, the UV-Vis spectra were measured by taking 1 mL aliquot of solution at the end of each step along the synthesis procedure. As shown in Figure 34 after the surfactant exchange with NaOL the LSPR maximum has a redshift of 13 nm due probably to the charge change on the surface of the AuNRs by the exchange between CTAB and NaOL. Furthermore, after coating with the $\text{Gd}(\text{OH})_3/\text{GdOHCO}_3 \cdot \text{H}_2\text{O}$ shells, it is observed a displacement about ~ 120 nm related to the change on the dielectric constant, since in the first step the AuNRs were exposed to water and then were coated by the gadolinium matrix changing the refractive index of the medium, causing a distortion on the plasmon field that leads to the dislocation of the LSPR band. In addition, Figure 35a shows a TEM image and EDS mapping of the final product after the thermal treatment. As mentioned above, the core-multishell structure and the distribution of the different Ln ions along the shell is maintained. However, it is observed a shape deformation of the AuNRs morphology. Measurements of the position of the LSPR band after the thermal treatment still need to be performed, although a blue shifting is expected as reported by Lui and Li, et al^{87,89,98}. Since thanks to the change from a rod-shape to a spherical morphology, there is a decrease in the charge separation which leads to an increase in the restoring forces that determine the oscillation frequency of the plasmon, increasing the energy of the longitudinal LSPR. Also, there is expected a decrease of the LSPR intensity due to the decrease of the dipole size as shown in figure 35b.

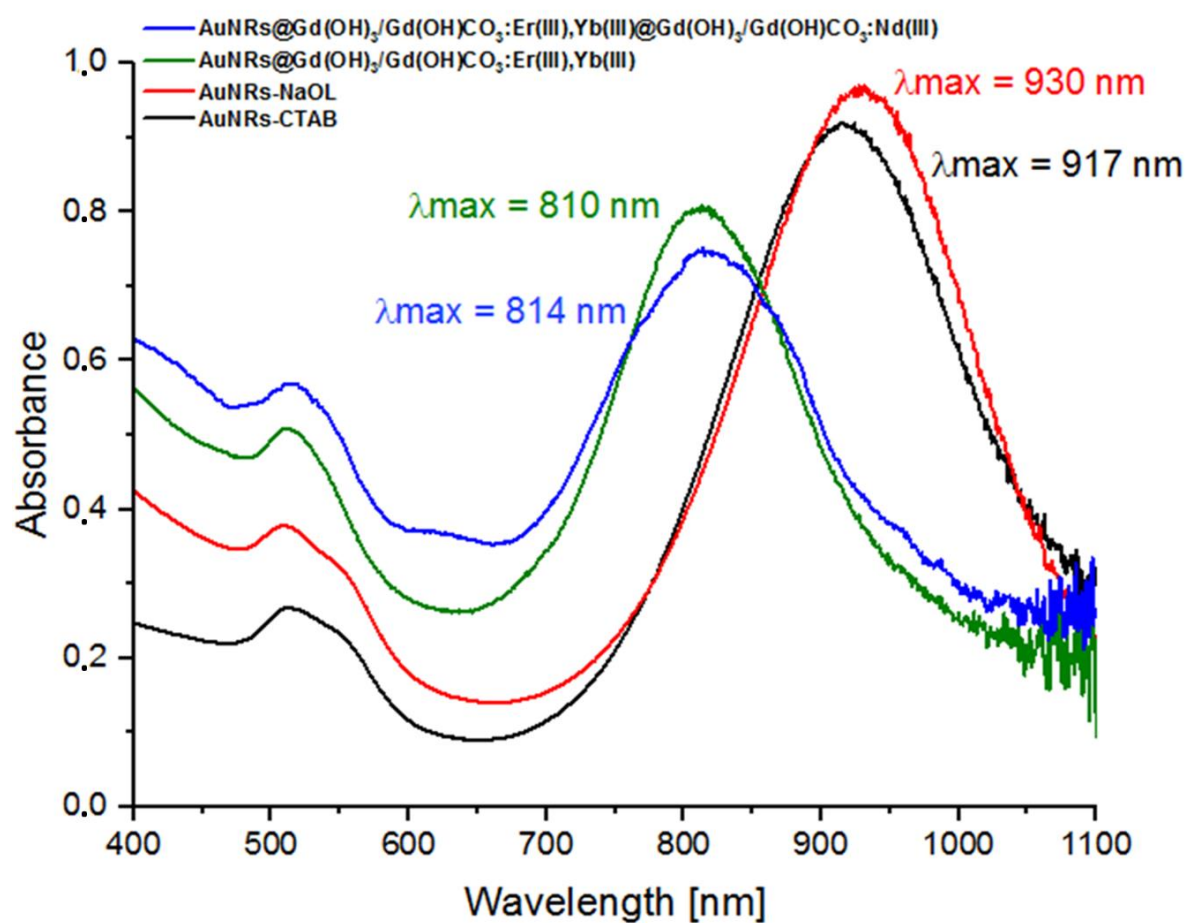


Figure 34. UV-Vis spectra at each step along the core-multishell synthesis. (---) AuNRs-CTAB, (----) AuNRs-NaOL, (-----) AuNRs@Gd(OH)₃/Gd(OH)CO₃:Er(III),Yb(III) and (----) AuNRs@Gd(OH)₃/Gd(OH)CO₃:Er(III),Yb(III)@Gd(OH)₃/Gd(OH)CO₃:Nd(III).

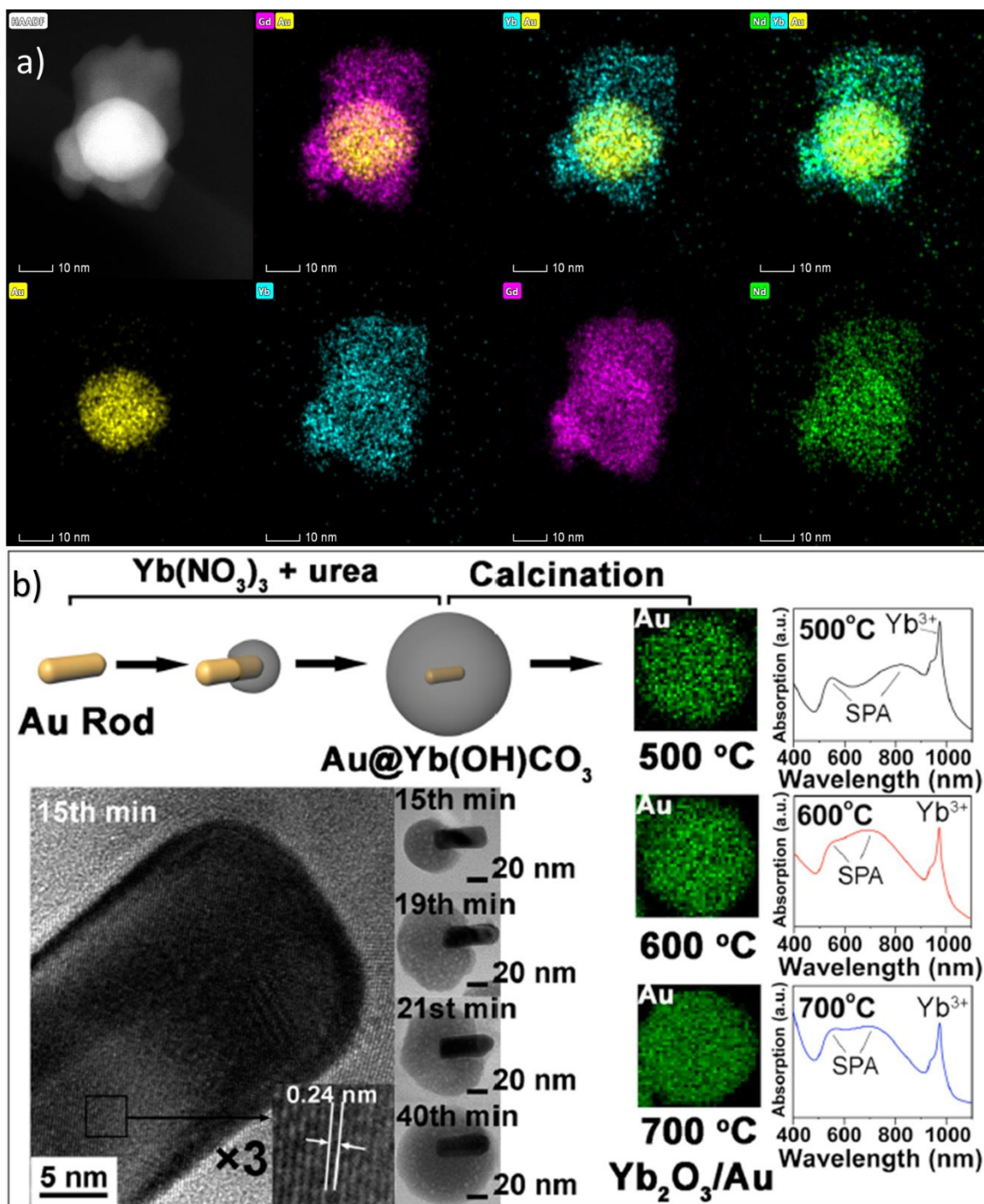


Figure 35. *a)* TEM image and EDS mapping of the AuNRs@Gd₂O₃:Er(III), Yb(III)@Gd₂O₃:Nd(III) after thermal treatment at 800 °C for 3h. *b)* Schematic synthesis procedure and HR-TEM images presenting the growing process of the Yb(OH)CO₃ onto AuNRs (left) and EDX mapping images, and absorption spectra presenting the distributions and the absorption properties of gold in the calcined samples (right). Reproduced from ref. 97 copyright J. Phys. Chem. C 2014.

On the other hand, the global emission intensities of the synthesized NPs are relative low compared to the usual matrices of fluorides using Yb and Er ions under excitation at 808 or 980 nm as reported in the literature^{33,75–77,99}. This could be associated with several factors, first, as can be noticed from Figure 34 the plasmonic core and the emitter ions are almost in direct contact, and as discussed above from Figure 10 when a fluorophore is placed near to a metallic surface, the interaction between the two materials results in a modified quantum yield and lifetime due to the additional radiative and non-radiative decay channels introduced by the presence of the metal NP. In addition, if the plasmonic material and the fluorophore are very close to each other, there are new paths whereby energy can pass. Then, non-radiative energy transfer from the Ln ions to the metal plasmon can occur leading to a fluorescence quenching¹⁰⁰; the opposite channel (energy transfer from the metal NP to the Ln ion) is not operative due to the extremely short lifetime of the plasmon (between 10^{-12} - 10^{-14}). Considering this, it is possible to explain the low emission intensity of the sample due to the non-radiative energy transfer between the Ln ions and the AuNPs in the core, allowed by the close distance between them. Otherwise, the AuNRs were synthesized with aspect ratios that lead to longitudinal LSPR bands between 800-980 nm in order to match with the excitation or emission bands of the Ln ions in the NIR region, however due to the shape deformation and the expected blueshift discussed above there is not overlapping. Then, the enhanced electromagnetic field generated by the excitation of the LSPR band has lower intensity and do not promote the transition rate from the ground state to the excited states with the same efficiency. Thus, the enhancement effect due to the local field decreases, resulting in a reduced intensity enhancement factor.

Chapter 4

Conclusions and future perspectives

The above-mentioned results show the synthesis of AuNRs with aspect ratios ranging from 3.9 to 4.9 nm, leading to longitudinal LSPR bands between 800 – 980 nm. The AuNRs were coated with $\text{Gd}(\text{NO}_3)_3$ with Yb, Er and Nd(III) ions through a surfactant exchange method, followed by a solvothermal process. TEM images and EDS analysis show the successful formation of the core-shell structure. Moreover, IR and fluorescence spectroscopy analyses suggest the formation of a hydroxide/hydroxycarbonate gadolinium matrix. Then, the precursor sample was subjected to a thermal treatment in order to achieve a low phonon energy lattice matrix such as gadolinium oxide. IR spectra HR-TEM images, SAED and XRD patterns suggest the formation of Gd_2O_3 in the cubic phase. Therefore, the main purpose of designing a hierarchical core-shell nanostructure based on AuNRs coated with $\text{Gd}_2\text{O}_3:\text{Er}(\text{III}), \text{Yb}(\text{III})$ and $\text{Gd}_2\text{O}_3:\text{Nd}(\text{III})$ was achieved. In addition, it was possible observe the energy transferences between the different Ln ions via DS energy transfer, showing that the proposed system is active in the NIR region and has a promissory potential for biological applications. Although, further studies still need to be performed in order to evaluate the photothermal capacity of the proposed system through hyperthermia measures, as well as control reactions in order to have a better understanding about the role of the plasmon in the emission intensity of the Ln ions.

As shown in chapter 3, there are some topics that should be further studied to optimizing the proposed system and have a deeper understanding of the interaction between plasmons and Ln ions, in order to develop a hierarchical system that could act as a thermal sensor and have potential applications of bioimaging and hyperthermia treatments by providing both optical tracking and photothermal capacity. Therefore, for further studies, it is necessary corroborate the amount of each phase (gold, hydroxide, hydroxycarbonate and oxide) along each step of the synthesis procedure, in order to have a better understanding of the reaction mechanism and the chemical structure of the prepared samples. In addition, X-ray photon spectroscopy measures may be performed to confirm the proper distribution of the different Yb, Er and Nd(III) ions along the shells.

On the other hand, optical thermometry measurements show a very low sensitivity of the samples in the biological range (30 - 51 °C), probably because at this temperature range the thermal energy is not enough to populate the emitter states of Er and Nd (III) ions. Thus, further measurements in a wider range must be done. Likewise, several works show an

increase of lifetime-dependent optical thermometry measures¹⁰¹⁻¹⁰³, thus considering that metallic plasmon could modify the lifetime of the emitter states in Ln ions^{68,69} by the introduction of new radiative and non-radiative decay paths, is also important study the lifetime decay profile of the system to have a better understanding of the interaction plasmon-Ln ion emission, to design a more accurate optical thermometer. Otherwise, the enhancement or quenching of the emission intensity of the Ln ions associated with the interaction with the plasmon of a metallic surface is close-related to the distance between them. Therefore, in order to increase the emission intensity of the prepared NPs a good alternative would be the addition of an inert shell of SiO₂ or Gd₂O₃ without the Ln ions in order to achieve a greater spacing, since as report in references [62-68] if the distance between the Ln ion and the plasmonic NPs are less than 5 nm, there is a non-radiative energy transfer process from the Ln ion to the metal NP leading to emission quench, at the same time, as the distance between them increases (5-35nm) there is an improvement of the emission intensity due to the effect of the enhanced electric local field which will increase the excitation rate from the ground state, enhancing the emission intensity.

In addition, considering that the AuNRs adopt a spherical-shape structure after the thermal treatment, which leads to a blueshift of the longitudinal LSPR band, and that the proposed system may be active either in the UV-Vis region via UC emissions. Fluorescence and UV-Vis spectroscopy measures should be done in order to establish the position of the LSPR band after the thermal treatment and study the emission $^4S_{3/2} \rightarrow ^4I_{15/2}$ of Er (III) at 545 nm due to the UC energy transfer between Yb and Er ions⁷⁰, since this emission should be enhanced by the gold plasmon. Finally, some control reactions should be performed in order to establish the total enhancement or quench factor of the AuNPs plasmon on the emission intensity of the proposed system. For example, comparative measures of the life-time, fluorescence and hyperthermia of the core-shell NPs with and without the AuNRs core.

Chapter 5

References

1. Jamkhande, P. G., Ghule, N. W., Bamer, A. H. & Kalaskar, M. G. Metal nanoparticles synthesis: An overview on methods of preparation, advantages and disadvantages, and applications. *J. Drug Deliv. Sci. Technol.* **53**, 101174 (2019).
2. Qin, L. *et al.* “Gold rush” in modern science: Fabrication strategies and typical advanced applications of gold nanoparticles in sensing. *Coord. Chem. Rev.* **359**, 1–31 (2018).
3. Khan, I., Saeed, K. & Khan, I. Nanoparticles: Properties, applications and toxicities. *Arab. J. Chem.* **12**, 908–931 (2019).
4. Devi, G. K. *et al.* A review on metallic gold and silver nanoparticles. *Res. J. Pharm. Technol.* **12**, 935–943 (2019).
5. Suchomel, P. *et al.* Simple size-controlled synthesis of Au nanoparticles and their size-dependent catalytic activity. *Sci. Rep.* **8**, 1–11 (2018).
6. Dal Forno, S., Ranno, L. & Lischner, J. Material, Size, and Environment Dependence of Plasmon-Induced Hot Carriers in Metallic Nanoparticles. *J. Phys. Chem. C* **122**, 8517–8527 (2018).
7. De Freitas, L. F., Varca, G. H. C., Batista, J. G. D. S. & Lugão, A. B. An overview of the synthesis of gold nanoparticles using radiation technologies. *Nanomaterials* **8**, (2018).
8. Cao, J., Sun, T. & Grattan, K. T. V. Gold nanorod-based localized surface plasmon resonance biosensors: A review. *Sensors Actuators, B Chem.* **195**, 332–351 (2014).
9. Willets, K. A. & Van Duyne, R. P. Localized Surface Plasmon Resonance Spectroscopy and Sensing. *Annu. Rev. Phys. Chem.* **58**, 267–297 (2007).
10. Yu, H., Peng, Y., Yang, Y. & Li, Z. Y. Plasmon-enhanced light–matter interactions and applications. *npj Comput. Mater.* **5**, 1–14 (2019).
11. Bai, X. *et al.* The basic properties of gold nanoparticles and their applications in tumor diagnosis and treatment. *Int. J. Mol. Sci.* **21**, (2020).
12. Mao, W., Son, Y. & Yoo, H. S. Gold Nanospheres and Nanorods for Anti-Cancer Therapy: comparative studies of fabrication, surface-decoration, and anti-cancer treatments. *Nanoscale* **6**, (2020).
13. Ishtiaq, S., Shah, K. U., Ur-Rehman, T. & Ud-Din, F. *Gold nanorods: new generation drug delivery platform. Metal Nanoparticles for Drug Delivery and Diagnostic Applications* (Elsevier Inc., 2020). doi:10.1016/b978-0-12-816960-5.00005-7.

14. Yang, H. *et al.* The impact of size and surface ligand of gold nanorods on liver cancer accumulation and photothermal therapy in the second near-infrared window. *J. Colloid Interface Sci.* **565**, 186–196 (2020).
15. Amendola, V., Pilot, R., Frasconi, M., Maragò, O. M. & Iatì, M. A. Surface plasmon resonance in gold nanoparticles: A review. *J. Phys. Condens. Matter* **29**, (2017).
16. Rizal, C., Belotelov, V., Ignatyeva, D., Zvezdin, A. K. & Pisana, S. Surface Plasmon Resonance (SPR) to Magneto-Optic SPR. *Condens. Matter* **4**, 50 (2019).
17. Hemmer, E., Benayas, A., Légaré, F. & Vetrone, F. Exploiting the biological windows: Current perspectives on fluorescent bioprobes emitting above 1000 nm. *Nanoscale Horizons* **1**, 168–184 (2016).
18. Ruggiero, E., Alonso-De Castro, S., Habtemariam, A. & Salassa, L. Upconverting nanoparticles for the near infrared photoactivation of transition metal complexes: New opportunities and challenges in medicinal inorganic photochemistry. *Dalt. Trans.* **45**, 13012–13020 (2016).
19. Chen, X. *et al.* Cr⁴⁺ activated NIR-NIR multi-mode luminescent nanothermometer for double biological windows. *Chem. Eng. J.* **396**, 125201 (2020).
20. Duong, H. Van *et al.* Biocompatible Chitosan-Functionalized Upconverting Nanocomposites. *ACS Omega* **3**, 86–95 (2018).
21. Mandari, K. K., Do, J. Y., Police, A. K. R. & Kang, M. Natural solar light-driven preparation of plasmonic resonance-based alloy and core-shell catalyst for sustainable enhanced hydrogen production: Green approach and characterization. *Appl. Catal. B Environ.* **231**, 137–150 (2018).
22. Chang, Y. *et al.* Anisotropic Plasmonic Metal Heterostructures as Theranostic Nanosystems for Near Infrared Light-Activated Fluorescence Amplification and Phototherapy. *Adv. Sci.* **6**, (2019).
23. Kang, J. K. *et al.* Principles and applications of nanomaterial-based hyperthermia in cancer therapy. *Arch. Pharm. Res.* **43**, 46–57 (2020).
24. Elahi, N., Kamali, M. & Baghersad, M. H. Recent biomedical applications of gold nanoparticles: A review. *Talanta* **184**, 537–556 (2018).
25. Tejada, E. M., Arámburo, M., Vargas, E., Contreras, O. E. & Hirata, G. A. Novel bifunctional Nd:YAG/Fe₃O₄ nanocomposite as nanothermometer/nanoheater for potential biomedical applications. *J. Phys. D. Appl. Phys.* **51**, (2018).

26. Zhong, Y. *et al.* Controlled growth of plasmonic heterostructures and their applications. *Sci. China Mater.* (2020) doi:10.1007/s40843-019-1262-6.
27. Ha, M. *et al.* Multicomponent Plasmonic Nanoparticles : From Heterostructured Nanoparticles to Colloidal Composite Nanostructures. (2019) doi:10.1021/acs.chemrev.9b00234.
28. Wiesholler, L. M. & Hirsch, T. Strategies for the design of bright upconversion nanoparticles for bioanalytical applications. *Opt. Mater. (Amst)*. **80**, 253–264 (2018).
29. Chatterjee, K., Sarkar, S., Rao, K. J. & Paria, S. Core / shell nanoparticles in biomedical applications. **209**, 8–39 (2014).
30. Anderson, S. D., Gwenin, V. V & Gwenin, C. D. Magnetic Functionalized Nanoparticles for Biomedical , Drug Delivery and Imaging Applications. **6**, (2019).
31. He, X. *et al.* AIE Featured Inorganic – Organic Core @ Shell Nanoparticles for High-Efficiency siRNA Delivery and Real-Time Monitoring. (2019) doi:10.1021/acs.nanolett.8b04677.
32. Lv, Y., Duan, S. & Wang, R. Progress in Natural Science : Materials International Structure design , controllable synthesis , and application of metal- semiconductor heterostructure nanoparticles. *Prog. Nat. Sci. Mater. Int.* 0–1 (2020) doi:10.1016/j.pnsc.2019.12.005.
33. Li, Y. *et al.* Coupling Resonances of Surface Plasmon in Gold Nanorod / Copper Chalcogenide Core À Shell Nanostructures and Their Enhanced Photothermal Effect. 1–8 (2018) doi:10.1002/cphc.201701338.
34. Qi, Z. *et al.* PEGylated graphene oxide-capped gold nanorods/silica nanoparticles as multifunctional drug delivery platform with enhanced near-infrared responsiveness. *Mater. Sci. Eng. C* **104**, 109889 (2019).
35. Hu, S. *et al.* Surface plasmon resonance enhancement of photoluminescence intensity and bioimaging application of gold nanorod @ CdSe / ZnS quantum dots. 22–31 (2019) doi:10.3762/bjnano.10.3.
36. Huang, J., Yang, Z., Wang, X. & Wang, Z. Core–Shell Gold Nanorod@Layered Double Hydroxide Nanomaterial with Highly Efficient Photothermal Conversion and Its Application in Antibacterial and Tumor Therapy. (2019) doi:10.1021/acsami.9b10373.
37. Bünzli, J. C. G. Benefiting from the unique properties of lanthanide ions. *Acc. Chem.*

- Res.* **39**, 53–61 (2006).
38. Bünzli, J. G. Lanthanide Photonics : Shaping the Nanoworld. *Trends Chem.* 1–13 (2019) doi:10.1016/j.trechm.2019.05.012.
 39. Seth, M., Schwerdtfeger, P., Dolg, M. & Fulde, P. Lanthanide and Actinide Contractions: Relativistic and Shell Structure Effects. *J. Am. Chem. Soc.* **117**, 6597–6598 (1995).
 40. Svetlana Eliseeva, B. Jean-C. Intriguing aspects of lanthanide luminescence. *Chem. Sci.* **4**, 1913–2268 (2013).
 41. Kurzen, H., Bovigny, L., Bulloni, C. & Daul, C. Electronic structure and magnetic properties of lanthanide 3+ cations. *Chem. Phys. Lett.* **574**, 129–132 (2013).
 42. Jiang, Z.-X. *et al.* Lanthanoid single-ion magnets with the LnN 10 coordination geometry. *Chem. Commun.* **52**, 6261–6264 (2016).
 43. Eliseeva, S. V. & Bünzli, J.-C. G. Lanthanide luminescence for functional materials and bio-sciences. *Chem. Soc. Rev.* **39**, 189–227 (2010).
 44. Mani, P., Ranjith, K. M., Mandal, S. & Paul, A. K. Comparative Studies on Optical and Electronic Behavior of Lanthanide-based Coordination Polymers: Synthesis, Structure, Absorption-Emission and Magnetic Properties. *J. Chem. Sci.* **130**, 1–9 (2018).
 45. Kang, D., Jeon, E., Kim, S. & Lee, J. Lanthanide-Doped Upconversion Nanomaterials: Recent Advances and Applications. *Biochip J.* **14**, 124–135 (2020).
 46. Shao, Q. *et al.* Multifunctional lanthanide-doped Core/Shell nanoparticles: Integration of upconversion luminescence, temperature sensing, and photothermal conversion properties. *ACS Omega* **3**, 188–197 (2018).
 47. Auzel, F. E. Materials and devices using double-pumped-phosphors with energy transfer. *Proc. IEEE* **61**, 758–786 (1973).
 48. Hudry, D., Howard, I. A., Popescu, R., Gerthsen, D. & Richards, B. S. Structure–Property Relationships in Lanthanide-Doped Upconverting Nanocrystals: Recent Advances in Understanding Core–Shell Structures. *Adv. Mater.* **31**, 1–25 (2019).
 49. Zong, H., Mu, X. & Sun, M. Physical principle and advances in plasmon-enhanced upconversion luminescence. *Appl. Mater. Today* **15**, 43–57 (2019).
 50. Dong, J. *et al.* Plasmon-enhanced upconversion photoluminescence: Mechanism and application. *Rev. Phys.* **4**, 100026 (2019).
 51. Mir, W. J., Sheikh, T., Arfin, H., Xia, Z. & Nag, A. Lanthanide doping in metal halide

- perovskite nanocrystals: spectral shifting, quantum cutting and optoelectronic applications. *NPG Asia Mater.* **12**, (2020).
52. Runowski, M., Stopikowska, N., Goderski, S. & Lis, S. Luminescent-plasmonic, lanthanide-doped core/shell nanomaterials modified with Au nanorods – Up-conversion luminescence tuning and morphology transformation after NIR laser irradiation. *J. Alloys Compd.* **762**, 621–630 (2018).
 53. Greybush, N. J. *et al.* Plasmon-Enhanced Upconversion Luminescence in Single Nanophosphor À Nanorod Heterodimers Formed through. *ACS Nano* **8**, 9482–9491 (2014).
 54. Fan, Y. & Zhang, F. A New Generation of NIR-II Probes: Lanthanide-Based Nanocrystals for Bioimaging and Biosensing. *Adv. Opt. Mater.* **7**, 1–14 (2019).
 55. Zhou, B. *et al.* Enhancing multiphoton upconversion through interfacial energy transfer in multilayered nanoparticles. *Nat. Commun.* **11**, 1–9 (2020).
 56. Li, Y., Zeng, S. & Hao, J. Non-Invasive Optical Guided Tumor Metastasis/Vessel Imaging by Using Lanthanide Nanoprobe with Enhanced Down-Shifting Emission beyond 1500 nm. *ACS Nano* **13**, 248–259 (2019).
 57. I, Y. L., Jiang, M., Xue, Z. & Zeng, S. 808 Nm Light Triggered Lanthanide Nanoprobes With Enhanced Down-Shifting Emission Beyond 1500 Nm for Imaging-Guided Resection Surgery of Tumor and Vascular Visualization. *Theranostics* **10**, 6875–6885 (2020).
 58. Fan, Y., Liu, L. & Zhang, F. Nano Today Exploiting lanthanide-doped upconversion nanoparticles with core / shell structures. *Nano Today* **25**, 68–84 (2019).
 59. Chen, G. *et al.* Energy-Cascaded Upconversion in an Organic Dye-Sensitized Core/Shell Fluoride Nanocrystal. *Nano Lett.* **15**, 7400–7407 (2015).
 60. Huang, L. *et al.* Simultaneous excitation and emission enhancement of near-infrared quantum cutting in B-NaYF₄: Er³⁺ nanoparticles by double plasmon modes of noble metals. *Opt. Commun.* **441**, 170–175 (2019).
 61. Hamilton, G. & Sanabria, H. *Chapter 6 - Multiparameter fluorescence spectroscopy of single molecules. Spectroscopy and Dynamics of Single Molecules* (Elsevier Inc., 2019). doi:10.1016/B978-0-12-816463-1.00006-7.
 62. Joyce, C., Fothergill, S. M. & Xie, F. Recent advances in gold-based metal enhanced fluorescence platforms for diagnosis and imaging in the near-infrared. *Mater. Today*

- Adv.* **7**, 100073 (2020).
63. Dong, J. *et al.* Plasmon-enhanced upconversion photoluminescence: Mechanism and application. *Rev. Phys.* **4**, 100026 (2019).
 64. Upconversion, P., Wu, D. M., Garc, A., Salleo, A. & Dionne, J. A. Plasmon-Enhanced Upconversion. (2014).
 65. Xu, W., Chen, X. & Song, H. Upconversion manipulation by local electromagnetic field. *Nano Today* (2017) doi:10.1016/j.nantod.2017.10.011.
 66. Gandra, N. *et al.* Probing distance-dependent plasmon-enhanced near-infrared fluorescence using polyelectrolyte multilayers as dielectric spacers. *Angew. Chemie - Int. Ed.* **53**, 866–870 (2014).
 67. Lin, L. *et al.* Plasmon-enhanced luminescence of Ag@SiO₂/β-NaYF₄:Tb³⁺ nanocomposites via absorption & emission matching. *Mater. Chem. Phys.* **220**, 278–285 (2018).
 68. Lin, L. *et al.* Plasmon-enhanced upconversion and quantum-cutting of water-soluble Au@SiO₂/NaYF₄:Tb³⁺,Yb³⁺@NaYF₄ nanocomposites. *J. Lumin.* **214**, 116598 (2019).
 69. Lv, R. *et al.* Plasmonic modulated upconversion fluorescence by adjustable distributed gold nanoparticles. *J. Lumin.* **220**, (2020).
 70. Wang, Y. *et al.* Tailoring Plasmonic Enhanced Upconversion in Single NaYF₄ : Yb³⁺ / Er³⁺ Nanocrystals. *Nat. Publ. Gr.* 1–7 (2014) doi:10.1038/srep10196.
 71. Zong, H., Wang, X., Mu, X., Wang, J. & Sun, M. Plasmon-Enhanced Fluorescence Resonance Energy Transfer. *Chem. Rec.* **19**, 818–842 (2019).
 72. Mohammadniaei, M. *et al.* Bifunctional Au@Bi₂Se₃ Core–Shell Nanoparticle for Synergetic Therapy by SERS-Traceable AntagomiR Delivery and Photothermal Treatment. *Small* **14**, 1–13 (2018).
 73. Ovejero, J. G. *et al.* Hybrid nanoparticles for magnetic and plasmonic hyperthermia. *Phys. Chem. Chem. Phys.* **20**, 24065–24073 (2018).
 74. Wang, C. *et al.* Switchable up-conversion luminescence bioimaging and targeted photothermal ablation in one core–shell-structured nanohybrid by alternating near-infrared light. *Dalt. Trans.* **48**, 5817–5830 (2019).
 75. Dong, B. *et al.* Observation of high efficient photothermal conversion of sub-10 nm Au nanoparticles coated on upconversion nanoparticles. *Opt. Mater. (Amst)*. **101**, 109665

- (2020).
76. He, F. *et al.* Enhanced up/down-conversion luminescence and heat: Simultaneously achieving in one single core-shell structure for multimodal imaging guided therapy. *Biomaterials* **105**, 77–88 (2016).
 77. Cheng, K., Zhang, J., Zhang, L., Wang, L. & Chen, H. Aptamer biosensor for Salmonella typhimurium detection based on luminescence energy transfer from Mn²⁺ doped NaYF₄:Yb, Tm upconverting nanoparticles to gold nanorods. *Spectrochim. Acta - Part A Mol. Biomol. Spectrosc.* **171**, 168–173 (2017).
 78. Ren, W. *et al.* Anisotropic functionalization of upconversion nanoparticles. *Chem. Sci.* **9**, 4352–4358 (2018).
 79. Zhang, Y. *et al.* Fabrication, photothermal conversion and temperature sensing of novel nanoplatform-hybrid nanocomposite of NaYF₄:Er³⁺, Yb³⁺@NaYF₄ and Au nanorods for photothermal therapy. *Mater. Res. Bull.* **114**, 148–155 (2019).
 80. Zhang, H. *et al.* Heterostructures of MOFs and Nanorods for Multimodal Imaging. *Adv. Funct. Mater.* **28**, 1–9 (2018).
 81. Parchur, A. K. *et al.* Vascular Interventional Radiology-Guided Photothermal Therapy of Colorectal Cancer Liver Metastasis with Theranostic Gold Nanorods. *ACS Nano* **12**, 6597–6611 (2018).
 82. Xu, D., Mao, J., He, Y. & Yeung, E. S. Size-tunable synthesis of high-quality gold nanorods under basic conditions by using H₂O₂ as the reducing agent. *J. Mater. Chem. C* **2**, 4989–4996 (2014).
 83. Wang, J. *et al.* Synthesis of gold/rare-earth-vanadate core/shell nanorods for integrating plasmon resonance and fluorescence. *Nano Res.* **8**, 2548–2561 (2015).
 84. Scarabelli, L., Sánchez-Iglesias, A., Pérez-Juste, J. & Liz-Marzán, L. M. A ‘Tips and Tricks’ Practical Guide to the Synthesis of Gold Nanorods. *J. Phys. Chem. Lett.* **6**, 4270–4279 (2015).
 85. He, J. *et al.* The facile removal of CTAB from the surface of gold nanorods. *Colloids Surfaces B Biointerfaces* **163**, 140–145 (2018).
 86. Maria Lumina Sonia, M., Anand, S., Blessi, S., Pauline, S. & Manikandan, A. Effect of surfactants (PVB/EDTA/CTAB) assisted sol-gel synthesis on structural, magnetic and dielectric properties of NiFe₂O₄ nanoparticles. *Ceram. Int.* **44**, 22068–22079 (2018).
 87. Zhang, Y., Wang, J., Nan, F. & Wang, Q. Q. Synthesis of gold nanorod/neodymium

- oxide yolk/shell composite with plasmon-enhanced near-infrared luminescence. *RSC Adv.* **8**, 20056–20060 (2018).
88. Chen, X. *et al.* Nd₂O₃/Au nanocomposites: Upconversion broadband emission and enhancement under near-infrared light excitation. *J. Mater. Chem. C* **2**, 5857–5863 (2014).
89. Li, H., Deng, Q., Liu, B., Yang, J. & Wu, B. Fabrication of core@spacer@shell Aunanorod@mSiO₂@Y₂O₃:Er nanocomposites with enhanced upconversion fluorescence. *RSC Adv.* **6**, 13343–13348 (2016).
90. Kim, P., Anderko, A., Navrotsky, A. & Riman, R. E. Trends in structure and thermodynamic properties of normal rare earth carbonates and rare earth hydroxycarbonates. *Minerals* **8**, (2018).
91. D’Assunção, L. M., Ionashiro, M., Rasera, D. E. & Giolito, I. Thermal decomposition of the hydrated basic carbonates of lanthanides and yttrium in CO₂ atmosphere. *Thermochim. Acta* **219**, 225–233 (1993).
92. Boopathi, G., Gokul Raj, S., Ramesh Kumar, G., Mohan, R. & Mohan, S. Synthesis of samarium doped gadolinium oxide nanorods, its spectroscopic and physical properties. *Indian J. Phys.* **92**, 715–724 (2018).
93. Aghazadeh, M. Preparation of Gd₂O₃ Ultrafine Nanoparticles by Pulse Electrodeposition Followed by Heat-treatment Method. *J. ultrafine Grained nanostructure Mater.* **49**, 80–86 (2016).
94. Gaspar, R. D. L., Mazali, I. O. & Sigoli, F. A. Particle size tailoring and luminescence of europium(III)-doped gadolinium oxide obtained by the modified homogeneous precipitation method: Dielectric constant and counter anion effects. *Colloids Surfaces A Physicochem. Eng. Asp.* **367**, 155–160 (2010).
95. Schmid, G. & Corain, B. Nanoparticulated gold: Syntheses, structures, electronics, and reactivities. *Eur. J. Inorg. Chem.* 3081–3098 (2003) doi:10.1002/ejic.200300187.
96. Rocha, J., Brites, C. D. S. & Carlos, L. D. Lanthanide Organic Framework Luminescent Thermometers. *Chem. - A Eur. J.* **22**, 14782–14795 (2016).
97. Zhao, D. *et al.* Design and Synthesis of an MOF Thermometer with High Sensitivity in the Physiological Temperature Range. *Inorg. Chem.* **54**, 11193–11199 (2015).
98. Liu, T. *et al.* Yb₂O₃/Au upconversion nanocomposites with broad-band excitation for solar cells. *J. Phys. Chem. C* **118**, 2908–2918 (2014).

99. Luo, Q. *et al.* Large enhancements of NaYF₄:Yb/Er/Gd nanorod upconversion emissions via coupling with localized surface plasmon of Au film. *Nanotechnology* **25**, (2014).
100. Carneiro Neto, A. N., Couto dos Santos, M. A., Malta, O. L. & Reisfeld, R. *Effects of spherical metallic nanoparticle plasmon on 4f-4f luminescence: A theoretical approach. Metal Nanostructures for Photonics* (Elsevier Ltd., 2018). doi:10.1016/B978-0-08-102378-5.00002-7.
101. Qiu, X. *et al.* Ratiometric upconversion nanothermometry with dual emission at the same wavelength decoded via a time-resolved technique. *Nat. Commun.* **11**, 1–9 (2020).
102. Li, L. *et al.* Study on the thermal sensitivity of β -NaYF₄: Yb³⁺-Er³⁺ nanothermometers based on luminescence ratiometric technology. *Curr. Appl. Phys.* **19**, 480–485 (2019).
103. Bednarkiewicz, A., Marciniak, L., Carlos, L. D. & Jaque, D. Standardizing luminescence nanothermometry for biomedical applications. *Nanoscale* **12**, 14405–14421 (2020).